Title

Model-based Online State and Parameter Estimation for Lithium-ion Battery Management Systems

Author

Zhang, Dong

Publication Date

2020

Model-based Online State and Parameter Estimation for Lithium-ion Battery Management Systems

by

Dong Zhang

A dissertation submitted in partial satisfaction of the
requirements for the degree of
Doctor of Philosophy

in

Engineering – Civil and Environmental Engineering

in the

Graduate Division

of the

University of California, Berkeley

Committee in charge:

Associate Professor Scott J. Moura, Chair
Professor Alexandre M. Bayen
Assistant Professor Mark Mueller

Summer 2020

Model-based Online State and Parameter Estimation for Lithium-ion Battery Management Systems

Abstract

Model-based Online State and Parameter Estimation for Lithium-ion Battery Management Systems

by

Dong Zhang

Doctor of Philosophy in Engineering – Civil and Environmental Engineering

University of California, Berkeley

Associate Professor Scott J. Moura, Chair

Lithium-ion (Li-ion) batteries have emerged as one of the most prominent energy storage devices for large-scale energy applications, e.g., hybrid electric vehicle (HEV), battery electric vehicles (BEV) and smart grids, due to their high energy and power density, low self-discharge and long lifetime. This dissertation focuses on developing and validating real-time model-based state and parameter estimation algorithms for Li-ion battery management systems. An overview of individual chapters are provided below.

Chapter 2: This chapter examines an online battery capacity estimation scheme from a thermal perspective. Mathematically, a cylindrical battery is modeled by coupling an electrical model that describes the dynamics of state of charge (SOC) with a two-state thermal dynamics. The critical challenges, however, are that (i) only input current, battery terminal voltage, and surface temperature are measureable in real time, and (ii) the sub-models are nonlinearly coupled. Consequently, the proposed hierarchical estimation algorithm uses a combination of input-to-state stability and sliding mode observer to collectively estimate cell capacity. Furthermore, the algorithm also presents real-time estimation for SOC, core temperature, heat generation, and thermal model parameters, making the algorithm a novel methodology for combined state of charge/state of health (SOH) estimation. The results demonstrate the benefits of thermal model based battery capacity estimation against traditional equivalent circuit based estimation.

Chapter 3: An electrochemical battery cell relies on the intercalation and de-intercalation of Li-ions between electrode solid-phase and electrolyte. An important cell capacity fade mechanism is the particle fracture due to intercalation-induced stresses. Volume changes of the electrode particles due to stress may induce particle fracture if the stress exceeds the yielding stress of the electrode material. In this chapter, we design a nonlinear observer based on a Single Particle Model (SPM) coupled with intercalation-induced stress to estimate battery bulk SOC, the particle stress profile, and the anode lithium diffusivity from online current and terminal voltage measurements only. Practically, real-time monitoring of aging related parameters in battery model and internal mechanical stress enables a battery

management system (BMS) to apply optimal control methods that protect against particle fracture, and consequently extend battery life.

Chapter 4: This chapter seeks to derive insight on estimation problem for battery packs. A battery pack system generally consists of hundreds or thousands of single cells connected in parallel and series in order to fulfill the requirements of high-energy and high-power applications. Mathematically, an equivalent circuit model is coupled with a thermal model to form a single cell model, which is then electrically interconnected with other cell models to form a pack model utilizing Kirchhoff's law. For cells in parallel, the resulting model is depicted by a differential-algebraic system (i.e. a descriptor system). The first part of this chapter aims at designing a Lyapunov-based asymptotic state observer for both differential (state of charge) and algebraic (local cell current) state estimation subject to reduced sensing. On the other hand, however, when number of cells in a pack becomes large, executing estimation algorithm for each and every cell becomes intractable computationally. The second part of this chapter proposes a monotone system based interval observer while taking into account modeling and measurement uncertainties in a pack. The estimated SOC intervals (upper and lower bounds) are guaranteed to envelop all SOC trajectories in the pack. The interval observer loses the tractability of single cell states but maximize the scalability of the algorithm.

Chapter 5: Battery thermal effects have been shown to be key factors in the rate of battery degradation. In practical applications, many cases of thermal runaways leading to fire and explosion of Li-ion batteries have been reported. This chapter proposes a model-based estimation algorithm for the battery temperature relying on a reduced high-fidelity nonlinear distributed parameter thermal model using surface measurements. Theoretically, the work extends the traditional partial differential equation (PDE) backstepping technique for a nonlinear parabolic PDE state estimation problem without performing linearization and spatial discretization prior to the observer design. When modeling and measurement disturbances exist, the algorithm quantifies the estimation error bounds in terms of L_2 spatial norm.

Chapter 6: The modeling for electrochemical phenomena inside a battery cell generally adopts a diffusion process. This chapter exclusively investigates a class of reaction-advection-diffusion system subject to boundary disturbance. Theoretically, we design a disturbance estimator for boundary disturbance in an unstable reaction-advection-diffusion PDE system, and derive a sufficient condition on the reaction coefficient, for which the disturbance estimator achieves asymptotic convergence. Subsequently, we propose an asymptotically convergent state estimator for the unstable reaction-advection-diffusion PDE using the estimated disturbance signal, adopting the backstepping technique. This chapter builds a solid foundation for PDE-based Li-ion concentration, and therefore SOC, estimation in a electrochemical cell subject to boundary disturbances.

Chapter 7: This chapter provides concluding remarks of the dissertation and discussions on future works.

To my parents

For their endless love, trust, and encouragement.

Contents

List of Figures

List of Tables

Acknowledgments

I would like to start by thanking my advisor, Professor Scott Moura. This work would not be possible without his mentorship and support. Throughout the years, Scott has become my inspiration and role model for pursuing a life-long academic career. I initially met him during the class he taught, CE 295 – Energy Systems and Control, in Fall 2015, which stimulates my passion for energy systems and battery system control. This experience eventually motivated me to join his Energy, Controls, and Applications Lab (eCAL) for the pursuit of my doctoral degree. I still remember when Scott asked me where I would position myself in ten years when I interviewed for the opening PhD position in his lab, and my answer to that was to become a professor. Five years had gone by, and my answer to that question still hasn't changed. He sets the role model for an amazing professorship that has been pushing me to chase that goal.

I am extremely thankful to my Qualifying Exam committee, Prof. Alexandre Bayen, Prof. Mark Mueller, Prof. Kenichi Soga, and Prof. Khalid Mosalam, for asking me challenging questions and providing critical feedback on my research. Additionally, I wish to extend my gratitude to my dissertation committee, Prof. Alexandre Bayen and Prof. Mark Mueller, for their insightful advice towards my dissertation.

Many special colleagues at UC Berkeley deserve my recognition for their mentorship and friendship. I thank Dr. Satadru Dey for his consistent patience and guidance on teaching me nonlinear control and estimation at the beginning of my graduate career, and our deep collaboration even after his departure from UC Berkeley. I thank Dr. Hector Perez for trusting me to carry on his legacy in the lab, and his endless knowledge on battery experimental testing as well as tips for career development. I thank Saehong Park for his technical discussions, inspirational conversation during difficult times, and introduction to authentic Korean barbeque. I thank Zach Gima for the discussions on battery research and his career advice. I certainly enjoyed the exciting conversations with him on college football after a stressful working day.

I am lucky to have met several world-class researchers from all around the world at Berkeley. I am deeply appreciative of the mentorship and friendship from Dr. Luis Couto. Luis came to eCAL from Brussels to learn from us, but I learned more from him than he could possibly imagine. Our relationship has gone far beyond research collaboration, as he's become one of my closest friends, although we live on different continents. I also thank Dr. Ross Drummond for the endless discussion on PDE control theory within the short period of time that he spent at eCAL. His hospitality and humbleness made him one of the best collaborators I've ever worked with. I wish to acknowledge Dr. Shu-Xia Tang for sharing her knowledge on PDE control and estimation and pushing me for technical excellence.

I would also like to express gratitude to the students I have mentored at eCAL: Pierre-François Massiani, Vanessa Hernandez-Cruz, and Preet Gill.

The CE 295 class students also deserve my recognition for asking course/project questions that I've never thought about, forcing me to understand every details repeatedly.

I am extremely lucky to have Rui Zhu in my life. We lived in different states for my entire PhD, but the warm caring and mental support from her have always made me strong. This PhD degree has challenged me to the greatest extent possible, and I could not have done it without the support of my loving girlfriend.

Finally, I would like to thank my parents for their endless love and support throughout my graduate career at UC Berkeley. I am very proud to dedicate this dissertation to them.

Chapter 1

Introduction

The transportation sector accounts for approximately 25% of global greenhouse gas emissions, per report [1]. Despite low penetration of electrical vehicles (EV), they are new innovative technology to solve climate change and air pollution problems [2]. EVs provide an alternative for fossil-fueled vehicles in order to reduce CO_2 emission. With the aggressive push in policy from automotive industry, the rapid evolution of EVs and smart grid technologies have driven the Li-ion battery to become a prominent device for energy storage. Li-ion batteries offer one of the best energy-to-weight ratios, have no memory effect, and undergo low self-discharge when not in operation [3]. The growing demands are pressing for batteries with better performance and safety. This dissertation combines electrochemical physics and dynamical system estimation/control theory to achieve accurate real-time monitoring of critical conditions of Li-ion battery systems to enhance battery energy, safety, and life.

Battery packs used for EV and utility storage usually demand high energy (kWh to MWh systems) [4]. Increased number of battery cells and higher energy eventually lead to greater impact under failure caused by immature management of battery system. Figure 1.1 and 1.2 demonstrate explosion of Li-ion battery packs in a Boeing 787 airplane and a Tesla Model S, respectively. Although the latter incident was a result of a highway accident, misuse of Li-ion batteries poses critical threats to its safe operation. The model-based online estimation/control methodologies proposed in this dissertation aims at addressing some of the challenges when understanding the current operational and health status of Li-ion batteries.

The remainder of this introduction is structured as follows. First we review the fundamentals of a Li-ion battery cell and battery management systems. Second, we provide formal statement of battery state of charge and state of health estimation problems. Third, we summarize the research challenges and the contribution of the dissertation. Finally, the dissertation organization is provided.

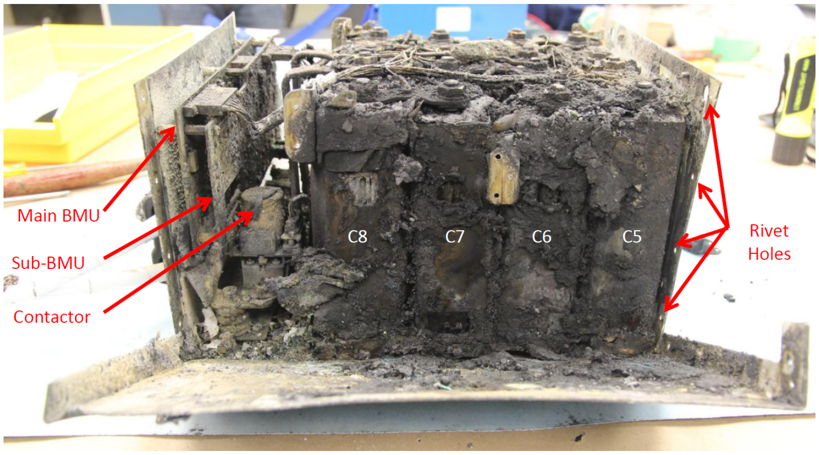

Figure 1.1: A Li-ion battery pack on-board a Japan Airlines Boeing 787 Dreamliner destroyed by fire at the General Edward Lawrence Logan International Airport, Boston, Massachusetts, in January 2013 [5].

Figure 1.2: Tesla Model S battery fire in Washington State in 2013 [4].

1.1 Battery Fundamentals

A typical Li-ion battery Cell (Figure 1.3) is built from several principal components, namely a negative electrode, a positive electrode, the electrolyte, and a separator. The *negative electrode* usually contains graphite, which is an intercalation material [3]. The *positive electrode* can be composed of different chemistries, but it is usually a metal oxide or a blend of multiple metal oxides, e.g., $LiMO_2$. The *separator* is an ionic conductor but an electronic insulator which is used to physically isolates the positive and negative electrodes [6]. The *electrolyte* is an ionic conductor that provides the medium for internal ionic charge transfer between the electrodes. The charged species in the electrolyte can move in response to an

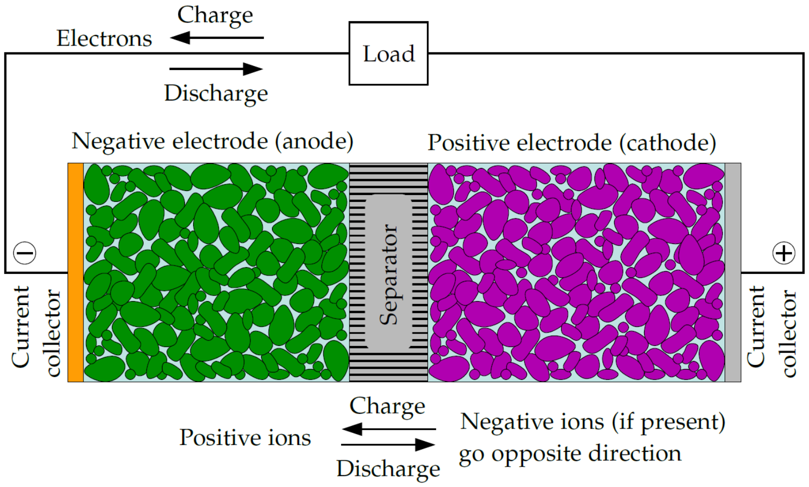

Figure 1.3: Anatomy of an electrochemical battery cell. The cell consists of four main regions: negative electrode (green), positive electrode (purple), separator (shaded grey), and electrolyte (blue) [6].

electrochemical potential gradient [3, 6]. At full charge the majority of lithium exists within the negative electrode solid phase particles, typically a lithiated carbon $\mathrm{Li}_x\mathrm{C}_6$ [7]. During discharge, lithium diffuses from the interior to the surface of these negative electrode material. At the surface, an electrochemical reaction (1.1) separates lithium into a positive lithium ion and electrons. Through this reaction, the negative electrode gives up electrons, a process by which the electrode is oxidized,

$$\mathrm{Li}_x\mathrm{C}_6 \rightleftharpoons \mathrm{C}_6 + x\mathrm{Li}^+ + x\mathrm{e}^-. \tag{1.1}$$

Next, the lithium ion diffuses from the negative electrode, through the separator, to the positive electrode. The electrons travel through the external circuit to power the connected load since the separator is an electrical insulator. The positive electrode accepts electrons from the external circuit, a process by which the electrode is reduced, and the electrons meet lithium ions at the positive electrode particle surface, and undergo the reverse electrochemical reaction according to

$$\mathrm{Li}_{(1-x)}\mathrm{MO}_2 + x\mathrm{Li}^+ + x\mathrm{e}^- \rightleftharpoons \mathrm{LiMO}_2. \tag{1.2}$$

This entire process is reversible by applying sufficient potential across the current collectors — rendering an electrochemical storage device [7]. Electrochemical potential energy at the negative electrode favors a chemical process that would release electrons into the external circuit and positively charged ions into the electrolyte. Also, electrochemical potential energy at the positive electrode favors a chemical process that would accept electrons from the external circuit and positively charged ions from the electrolyte. The resulting electrical potential difference between the terminals of the cell is the cell voltage [6].

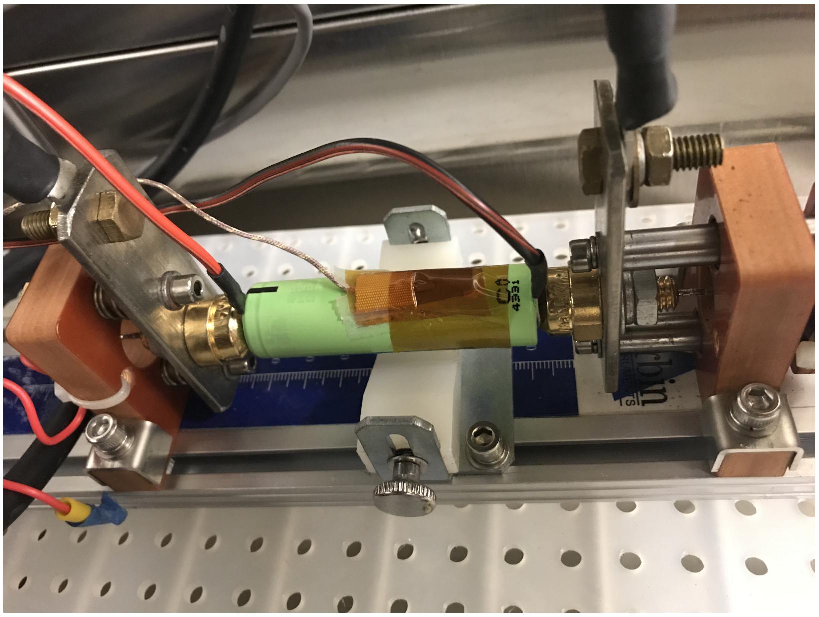

Figure 1.4: Experimental setting for a lab testing of a cylindrical Li-ion battery cell.

1.2 Battery Systems

This dissertation concerns the proper management of battery cells/packs, which is a task that requires both hardware and software components. While both components are equally important in a battery management system (BMS), we devote our attention to software methods, i.e., algorithms. The calculations in algorithms utilize measured data to estimate cell/pack present operational status, to control charging/discharging trajectory, and to predict its performance limits. This sections briefly introduces viable/available on-board measurements for BMS, and the hardware equipment for collecting the data.

First of all, the operating voltage of a single cell for various Li-ion battery chemistries is typically between 2 and 4.2 volts [8]. Individual cell voltages must be carefully monitored since Li-ion batteries are vulnerable to overcharge and overdischarge. For instance, overcharging a Li-ion cell can initiate undesired chemical side reactions that leads to degradation [6]. Second, battery cell dynamics are strong functions of temperature. Practically, many cases of thermal runaways leading to fire and explosion of Li-ion battery have been previously reported in [9]. Thermal effects have also been shown to be key factors in the rate of battery degradation [10]. Finally, a BMS must also monitor battery current to detect abuse conditions and to ensure safety. These measurements, i.e., current, voltage, and temperature, are critical inputs to most state of charge and state of health estimation algorithms that will be introduced later in this dissertation. It should be pointed out that there exists advanced sensors used to measure battery internal conditions, such as internal temperature [11] and stress [12]. However, installation of these sensors usually involves destruction of battery cell packaging and therefore requires safety protection, prohibiting the usage in real-time operation. Hence, a BMS commonly adopts only current, voltage, and (lumped) surface temperature measurements for online management.

Fig. 1.4 shows a typical experimental setting for a Li-ion battery cell at the University of California, Berkeley. An Arbin high current cylindrical cell holder is used to hold the battery cell inside of an ESPEC BTL-433 environmental chamber that maintains the test ambient temperature at the desired point. A thermocouple is placed on the surface of the cell to measure surface temperature. A PEC SBT2050 cycler (not shown in the figure) is used to input charge-discharge profiles and simultaneously record applied current and the corresponding voltage.

1.3 State of Charge and State of Health Estimation

This section introduces two of the most critical properties of an electrochemical Li-ion battery cell: state of charge (SOC) and state of health (SOH), and outlines the state and parameter estimation problem statements.

SOC Estimation Problem

SOC is the indication for the quantity of lithium within each electrode's solid phase. A Li-ion cell stores electrochemical energy in the form of lithium. We define SOC of a cell to be 100% when the cell is fully charged and 0% when the cell is fully discharged. When a cell is at an intermediate status between fully charged and fully discharged, the value of SOC is between 0% and 100%. In terms of lithium concentration, SOC can be represented by the ratio between the average Li-ion concentration at either positive or negative electrode and the maximum possible Li-ion concentration can be held at that electrode.

SOC is analogous to a fuel tank level. Unlike fuel tank levels, SOC cannot be directly measured and must be estimated. From system modeling point of view, SOC is one of the system states and its effect can be reflected by the measured voltage through a nonlinear mapping. When a battery cell is at its equilibrium, the voltage typically increases with respect to increasing SOC, and vice versa. The key challenges for SOC estimation are lack of complete observability and model nonlinearities [7].

SOH Estimation Problem

On the other hand, battery SOH metrics indicate a battery's relative age. To completely understand aging, we must consider a cell from a physics based perspective. In a Li-ion cell, aging occurs in both the negative electrodes and positive electrodes. In the negative electrode, aging effects are observed at three different scales. First, at the surface of the electrode active-material particles, solid–electrolyte interphase (SEI) surface film can be formed as a result of unwanted side reactions. Second, aging can take place within the interior of the active material particles, such as particle fracture and changes in porosity due to volume change. Third, the overall composite electrode structure can lead to degradation, including lithium plating that eventually causes short circuit, etc. Understanding and mathematically modeling aging is a hard task and unfortunately there is no universally agreed-upon definition of SOH [6]. However, at system-level, SOH estimation normally refers to the process by which appropriate cell model parameters are estimated as the cell ages. The two most common SOH metrics are charge capacity fade and impedance rise (i.e. power fade). Charge capacity fade indicates how charge capacity has degraded relative to its fresh value, e.g. a 2 Ah cell may hold 1.6 Ah after several years of use. Power fade represents how power capacity has decreased relative to its fresh value, e.g. a fresh cell may provide 360W of power for 10 seconds, but only 300W after two years of use [7]. There is a consensus in the literature that a cell reaches it end-of-life (EOL) if its charge capacity decreases by 20% or its impedance doubles.

A typical Li-ion cell can be charged and discharged for more than 1000 times until it reaches the EOL, so battery SOH changes slowly. Hence, the estimation algorithm for SOC needs to operate at a fast time scale (e.g. every 1 second) wheres SOH can be updated at a much slower time scale (e.g. days).

1.4 Technical Challenges

The design of online model-based estimators for Li-ion battery states and parameters is particularly challenging for the following reasons:

- Full-order electrochemical models for Li-ion batteries are structurally complex and they are not suited for real-time estimation and control design due to high computational requirements. Hence, the reduced-order models are required.
- The electrochemical (or even some simple equivalent circuit) battery models are over-parameterized. The states/parameters of such systems are generally not completely observable/identifiable from the input-output data, i.e., current, voltage, and temperature measurements.
- A large-scale battery pack consisting of hundreds or thousands of cells are not well-understood due to its natural differential-algebraic structure. An efficient monitoring framework for battery packs is demanding.
- The intercalation and de-intercalation processes inside an electrochemical battery cell are generally modeled by partial differential equations (PDEs). However, the available techniques that can be utilized to deal with nonlinear PDEs are lacking.

1.5 New Contribution of this Dissertation

The overall goal of this dissertation is to provide model-based estimation techniques for accurate battery crucial internal states monitoring. The contributions towards this objective are summarized as follows.

- Chapter 2: The design of real-time battery SOC and charge capacity estimation from a thermal point of view with guaranteed convergence proof, which demonstrates performance enhancements over traditional current-voltage based capacity estimator. This chapter is produced based upon the following publications:
    - Dong Zhang, Satadru Dey, Hector E. Perez, and Scott J. Moura. "Real-Time Capacity Estimation of Lithium-Ion Batteries Utilizing Thermal Dynamics". In: *IEEE Transactions on Control Systems Technology* (2019).
    - Dong Zhang, Luis D. Couto, Saehong Park, Preet Gill, and Scott J. Moura, "Nonlinear Observer for Lithium-Ion Batteries with State-Dependent Parameters". In *IFAC Proceedings*, 2020.
- Chapter 3: The model development of a reduced-order electrochemical model with diffusion induced mechanical stress, and a nonlinear adaptive observer for SOC and SOH monitoring. This allows a BMS to apply optimal control methods that protect against particle fracture, and consequently extend battery life. This chapter integrates and re-produces the results from
    - Dong Zhang, Satadru Dey, Luis D. Couto, and Scott J. Moura. "Battery Adaptive Observer for a Single-Particle Model With Intercalation-Induced Stress". In: *IEEE transactions on control systems technology* (2019).
- Chapter 4: The modeling framework for cells connected in parallel/series to form a battery pack via a differential-algebraic system (*a.k.a.* a descriptor system), the design for descriptor system based estimator for obtaining individual cell SOC, and a scalable interval observer for packs with large number of heterogeneous cells. It tackles the challenging parallel cell estimation problem and the computational burden when executing single cell estimators for a large amount of cells. This chapter is inherited from the following publications:
    - Dong Zhang, Luis D. Couto, Sebastien Benjamin, Wente Zeng, Daniel F. Coutinho, and Scott J. Moura. "State of Charge Estimation of Parallel Connected Battery Cellsvia Descriptor System Theory". 2020 American Control Conference (ACC), Denver, CO, USA, 2020, pp. 2207-2212.
    - Dong Zhang, Luis D. Couto, Preet Gill, Sebastien Benjamin, Wente Zeng, and Scott J. Moura. "Interval Observers for SOC Estimation of Lithium-ion Battery Packs". 2020 American Control Conference (ACC), Denver, CO, USA, 2020, pp. 1149-1154.

- Chapter 5: The framework for a high-dimensional temperature PDE model reduction and a PDE model-based thermal estimation using only the boundary temperature measurements, which enables an accurate temperature monitoring using high-fidelity models and nonlinear PDE estimation techniques. This chapter is currently under development with the following manuscript:
    - Dong Zhang, Satadru Dey, Shu-Xia Tang, Ross Drummond, and ScottJ. Moura. "Battery Temperature Estimation with an Uncertain Semilinear Thermal PDE Model".
- Chapter 6: The mathematical foundation for the combined state and disturbance estimation for an unstable reaction-advection-diffusion PDE subject to boundary disturbances, which facilitates the disturbance rejection control that can be readily applied to battery SOC estimation via solid-phase lithium concentration estimation. This chapter is originated and produced using
    - Dong Zhang, Shu-Xia Tang, and Scott J. Moura. "State and Disturbance Estimator for Unstable Reaction-Advection-Diffusion PDE with Boundary Disturbance". In: *2019 Proceedings of the Conference on Control and its Applications*. SIAM. 2019, pp. 67–74.

1.6 Dissertation Organization

The remaining chapters of this dissertation are organized as follows. Chapter 2 presents a real-time battery capacity estimation algorithm utilizing thermal dynamics. Chapter 3 proposes a battery adaptive observer for a reduced order electrochemical model, namely the single particle model, with intercalation-induced stress, for accurate battery health monitoring. Chapter 4 examines estimation algorithms for battery packs, especially for cells connected in parallel. Chapter 5 discusses the battery thermal estimation with an uncertain high-fidelity semilinear PDE model, followed by a general framework for state and disturbance estimator for an unstable reaction-advection-diffusion PDE with boundary disturbance in Chapter 6. Finally, the key contributions of this dissertation and potential future works are summarized in Chapter 7.

Chapter 2

Real-Time Capacity Estimation of Lithium-Ion Batteries Utilizing Thermal Dynamics

2.1 Introduction

This chapter proposes and rigorously analyzes a thermal model-based online battery charge capacity estimation algorithm.

An advanced BMS implements real-time control/estimation algorithms that enhance battery performance while improving safety. A crucial function of a BMS is to estimate the SOC and the SOH. Capacity fade is one of the most important metrics among all of principal effects of battery aging [13]. Accurate real-time capacity estimation with certified convergence properties is still an unsolved problem.

The existing literature contains several approaches to battery capacity estimation. They can be broadly categorized into offline and online approaches.

Offline approaches generally develop capacity estimation scheme in specific laboratory settings with access to large amounts of battery data under varying operating conditions [14, 15, 16]. However, the applicability of the offline approaches is limited due to the following reasons: i) in real-time, we have access to very limited amount of data; ii) battery degradation depends significantly on users, operating conditions, etc. Therefore, a single offline capacity estimation scheme may not be sufficient for these cases.

Online capacity estimation methods operate on embedded BMS micro-controllers utilizing real-time measurements. Generally, online approaches are comparatively more challenging than their offline counterparts, due to lack of measured information and limited computation power. Several studies have investigated this. Seminal work exploring combined SOC and model parameter estimation using Kalman Filter (KF) were introduced in [17, 18]. In [19], a dual sliding mode observer consists of a fast-paced and a slow-paced time-varying observer was presented for estimating the SOC and SOH of Li-PB batteries.

Lin *et al.* developed an adaptive observer based on online parameterization method for battery core temperature estimation and health monitoring [20]. Electrochemical model-based battery aging studies provide a sharp understanding of the underlying physical and chemical processes occurring during battery utilization. For instance, a reduced-order electrochemical model for a composite electrode battery combined with KF was utilized for a dual-observer design to estimate SOC and capacity [21]. Moura *et al.* performed combined SOC/SOH estimation based on single particle model (SPM) and the concept of backstepping state estimator for partial differential equations (PDEs) [22]. Several other authors used Particle Filter (PF) for battery state of health estimation [23, 24]. Machine learning tools for SOH estimation are attracting extensive attention in recent years. For example, the Support Vector Machine (SVM) is commonly used as a regression tool for SOH estimation [25]. Efforts have also been made to improve accuracy of battery health estimation by combining SVR with a Bayesian framework [26]. However, none of the aforementioned approaches explore battery capacity estimation from a thermal perspective. Moreover, only few of these algorithms have proven convergence properties - a crucial requirement for ensuring reliable operation in real-world BMS. In this chapter, we propose and rigorously analyze a capacity estimation scheme that utilizes battery thermal dynamics.

In this chapter we design a thermal model-based scheme for battery capacity (SOH) estimation from only input current and output voltage measurements. The results specifically (i) analyze the observer convergence with modeling uncertainties; (ii) provide algorithm validation on experimental capacity fade data from a commercial battery cell; (iii) enhance the estimation algorithm by having a real-time thermal model parameter identification step.

The reminder of this chapter is organized as follows: Chapter 2.2 presents battery electrical and thermal models. Chapter 2.3 examines thermal model parameter identifiability, state estimation with unknown input, and sliding mode observers with convergence analysis. Chapter 2.4 highlights the benefits of thermal model-based capacity estimation against conventional methods sorely based on current-voltage data. Chapter 2.5 discusses the capacity estimation algorithm validation on simulation and experimental data. Conclusions are drawn in Chapter 2.6.

2.2 Battery Model

A coupled electro-thermal model is detailed for a cylindrical lithium-iron-phosphate battery cell (A123 ANR26650M1). The model utilizes a coulomb counting method to capture the dynamics of SOC and a two-state thermal model that predicts battery surface and core temperatures.

Electrical Model

The SOC is computed via the coulomb counting method by integrating the applied current normalized by battery capacity over time. The dynamical equation is given by:

$$\frac{dSOC(t)}{dt} = -\frac{I(t)}{C_{bat}}, \tag{2.1}$$

where $I(t)$ is the input current, and we specify positive $I(t)$ for discharge and negative $I(t)$ for charge. Parameter C_{bat} is the battery charge capacity in Ampere-second.

Thermal Model

We consider a two-state lumped thermal model for a cylindrical battery, adopted from [27]. This model assumes homogeneity along the cell's longitudinal axis. The model states are core temperature (T_c) and surface temperature (T_s):

$$C_c \frac{dT_c(t)}{dt} = \frac{T_s(t) - T_c(t)}{R_c} + \dot{Q}(t) + \nu_c(t), \tag{2.2}$$

$$C_s \frac{dT_s(t)}{dt} = \frac{T_f(t) - T_s(t)}{R_u} - \frac{T_s(t) - T_c(t)}{R_c} + \nu_s(t), \tag{2.3}$$

$$\dot{Q}(t) = I(t) \left[OCV\big(SOC(t)\big) - V_T(t) - T(t)\frac{dU}{dT} \right], \tag{2.4}$$

$$T(t) = \frac{1}{2}\big(T_s(t) + T_c(t)\big), \tag{2.5}$$

$$y(t) = T_s(t) + n(t), \tag{2.6}$$

where R_c, R_u, C_c and C_s represent heat conduction resistance, convection resistance, core heat capacity, and surface heat capacity, respectively. Symbol $\dot{Q}(t)$ is internal heat generation. Heat generation from resistive dissipation and entropic heat are considered, where dU/dT is the entropic coefficient and $T(t)$ is the average of surface and core temperature [28]. V_T denotes the measureable terminal voltage, whereas OCV is the open circuit voltage as a function of state of charge. We assume the coolant flow rate is constant and the ambient temperature T_f is nearly constant [11]. We also introduce bounded terms $\nu_c(t)$ and $\nu_s(t)$ to model the uncertainties in the thermal dynamics, where $\nu_c(t) \leq \overline{\nu}_c$ and $\nu_s(t) \leq \overline{\nu}_s$. Estimates of $\overline{\nu}_c$ and $\overline{\nu}_s$ can be found by comparing the open-loop thermal model output with experimental data. Moreover, a time-varying but bounded measurement noise $n(t) \leq \overline{n}$ is considered, with $\overline{n} > 0$.

Re-arranging (2.2)-(2.6) into state-space form:

$$\dot{x}(t) = Ax(t) + Bu(t) + G\dot{Q}(t) + \nu(t), \tag{2.7}$$

$$y(t) = Cx(t) + n(t), \tag{2.8}$$

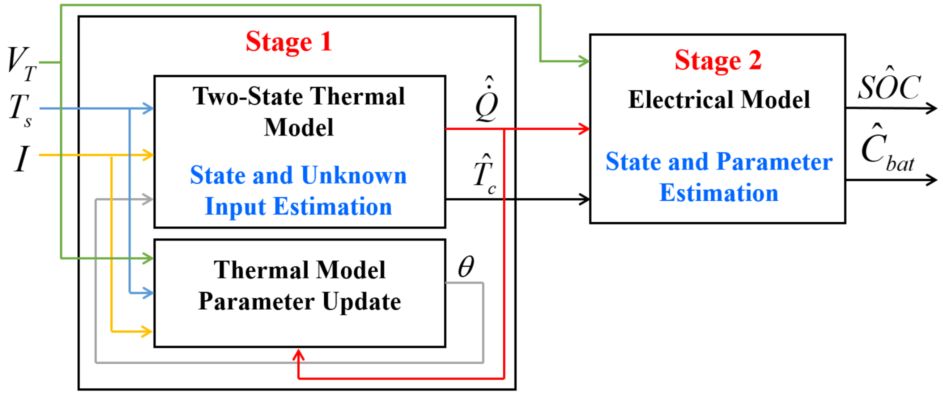

Figure 2.1: Cascaded online capacity estimation structure

where the input, states, and uncertainties are given by

$$x(t) = \begin{bmatrix} T_c(t) \\ T_s(t) \end{bmatrix}, \quad u(t) = T_f, \quad \nu(t) = \begin{bmatrix} \nu_c(t) \\ \nu_s(t) \end{bmatrix} < \bar{\nu} = \begin{bmatrix} \bar{\nu}_c \\ \bar{\nu}_s \end{bmatrix}, \tag{2.9}$$

and the corresponding system matrices are

$$A = \begin{bmatrix} -\frac{1}{R_cC_c} & \frac{1}{R_cC_c} \\ \frac{1}{R_cC_s} & -\left(\frac{1}{R_uC_s} + \frac{1}{R_cC_s}\right) \end{bmatrix}, \quad B = \begin{bmatrix} 0 \\ \frac{1}{R_uC_s} \end{bmatrix}, \quad G = \begin{bmatrix} \frac{1}{C_c} \\ 0 \end{bmatrix}, \quad C = \begin{bmatrix} 0 & 1 \end{bmatrix}. \tag{2.10}$$

Remark 1. *The local observability of the thermal model (2.2)-(2.6) has been verified by computing the rank of the linearized system at the equilibrium points.*

2.3 Online Capacity Estimation Scheme

The goal of this work is to develop an online battery capacity estimation scheme. We present a hierarchical structure depicted in Figure 2.1. In Stage 1, heat generation $\dot{Q}$ in the T_c-dynamics (2.2) is treated as a bounded unknown input. An output error injection based state and unknown input estimation technique, along with the two-state thermal model are employed to estimate the unmeasured state (T_c) and unmeasured input ($\dot{Q}$), using the online measurements of input current (I) and surface temperature (T_s). Based on the thermal model parameter sensitivity analysis, R_c is updated in real time to improve model and estimation accuracy. Next, the estimated core temperature $\widehat{T}_c$ and heat generation $\widehat{\dot{Q}}$, as well as the measured terminal voltage (V_T), are utilized to algebraically compute a pseudo-measurement of OCV within Stage 2, where a sliding mode observer based on the SOC-model is applied to simultaneously estimate the unmeasured state (SOC) and unknown parameter (C_{bat}). In the following subsections, we detail the design of each stage.

Stage 1: Core Temperature & Heat Generation Estimation

The Stage 1 aims to estimate the core temperature (unmeasured state) and heat generation (unmeasured input).

Thermal Model Parameter Identification

We first evaluate the thermal parameter identifiability. The method for ranking output sensitivity with respect to parameters and determining parameter linear dependence is outlined in [29]. Consider the thermal model parameters:

$$\theta_t = \begin{bmatrix} C_c & C_s & R_c & R_u \end{bmatrix}^\top . \tag{2.11}$$

The sensitivity vector

$$S = \begin{bmatrix} \frac{\partial y}{\partial C_c} & \frac{\partial y}{\partial C_s} & \frac{\partial y}{\partial R_c} & \frac{\partial y}{\partial R_u} \end{bmatrix} \in \mathbb{R}^{N\times 4}, \tag{2.12}$$

represents each parameter's sensitivity in the output, where N is the number of measurements. The Gram-Schmidt orthonormalization of $S^\top S$ reveals information about linear dependence between parameters. Let $S^\top S = D^\top C D$ with $D \in \mathbb{R}^{4\times 4}$ and $C \in \mathbb{R}^{4\times 4}$, where $D(i,i) = \|S_i\|$ and $D(i,j) = 0$ for $i \neq j$, and $C(i,i) = 1$ and $C(i,j) = \frac{\langle S_i, S_j\rangle}{\|S_i\|\|S_j\|}$. Herein, $\|\cdot\|$ denotes the Euclidian norm and $\langle\cdot,\cdot\rangle$ is the inner product. Diagonal matrix D provides a quantification of parameter sensitivity. Strong linear dependence exists between $\theta_{t,i}$ and $\theta_{t,j}$ if the value of $\frac{\langle S_i, S_j\rangle}{\|S_i\|\|S_j\|}$ is near ± 1. This indicates that if the off-diagonal element of matrix C is near ± 1, then the corresponding pair of parameters are difficult to identify separately. An example of the thermal parameter sensitivity analysis based on the profile shown in the right plot of Figure 2.3 for a LFP cell is performed, and the result reveals that the model output is most sensitive to R_u (yet assumed to be constant in this work) and R_c, and strong linear dependence exists between R_u, C_c, and R_c. Consequently, R_c is chosen to be identified in real time, considering parameter sensitivity and linear dependence.

Remark 2. *According to Ref. [20], the heat capacities C_c and C_s are relatively constant over battery lifetime since they depend on the material thermal properties and the mass of the rolled electrode assembly and the casing. Meanwhile, R_u is affected by the coolant flow rate, which is assumed to be constant. Coincidently, the implication of sensitivity analysis matches the physical intuition, where the change of R_c over lifetime is the consequence of battery degradation.*

An online parameter estimation algorithm, which aims to minimize the instantaneous squared error between measured surface temperature and model output by updating R_c, is running in real time to ensure estimation accuracy. A parametric model for such identification can be derived by performing Laplace Transformation on thermal model (2.2)-(2.3)

[20]:

$$s^2T_s - sT_{s,0} = \frac{-1}{C_cC_sR_c}\left[(C_c+C_s)sT_s - C_sT_{s,0} - C_cT_{c,0}\right] + \frac{1}{C_cC_sR_c}\hat{\dot{Q}} + \frac{1}{C_cC_sR_cR_u}(T_f - T_s) + \frac{1}{C_sR_u}s(T_f - T_s), \tag{2.13}$$

where $T_{s,0}$ and $T_{c,0}$ are initial conditions of surface and core temperatures. Herein, notice in (2.13) that we feedback the heat generation estimation $\hat{\dot{Q}}$ from the upper block in Stage 1 to improve the estimates of thermal parameter, which is visualized by the red arrow in Figure 2.1. It is assumed that battery evolves from the steady state, and thus $T_{s,0} = T_{c,0}$. Further, the ambient temperature T_f is assumed to be constant, namely $sT_f = 0$:

$$s^2T_s - sT_{s,0} + \frac{1}{C_sR_u}sT_s = \frac{1}{R_c}\left[-\frac{C_c+C_s}{C_cC_s}(sT_s - T_{s,0}) + \frac{1}{C_cC_s}\hat{\dot{Q}} + \frac{1}{C_cC_sR_u}(T_f - T_s)\right], \tag{2.14}$$

To avoid time differentiation, a filter needs to be applied in both sides of (2.14). The filter takes the form

$$\frac{1}{\Lambda(s)} = \frac{1}{(s+\lambda_1)(s+\lambda_2)}, \tag{2.15}$$

where λ_1 and λ_2 are time constants of the filter [30]. Then we can derive a linear parametric model

$$Z(s) = \theta^\top \Phi(s). \tag{2.16}$$

with

$$Z(s) = \frac{s^2}{\Lambda(s)}T_s + \frac{1}{C_sR_u}\frac{s}{\Lambda(s)}T_s - \frac{s}{\Lambda(s)}T_{s,0}, \tag{2.17}$$

$$\theta = \frac{1}{R_c}, \tag{2.18}$$

$$\Phi(s) = \frac{1}{\Lambda(s)}\left[-\frac{C_c+C_s}{C_cC_s}(sT_s - T_{s,0}) + \frac{1}{C_cC_s}\hat{\dot{Q}} + \frac{1}{C_cC_sR_u}(T_f - T_s)\right], \tag{2.19}$$

Both observation Z and regressor Φ are measured or generated from measured signals. Parameter θ will be identified recursively. For practical implementation, the identification is formulated along with signals $z(t)$ and $\phi(t)$ in the time domain, where $Z(s)$ and $\Phi(s)$ are Laplace transform of $z(t)$ and $\phi(t)$. For instance, $z_1(t)$, whose Laplace transform is $Z_1(s) = s^2T_s/\Lambda(s)$ (the first term on the right hand side of (2.17)), can be obtained by computing the convolution of $T_s(t)$ and the inverse Laplace transform of $s^2/\Lambda(s)$. Hence, we would be able to avoid time differentiation of $T_s(t)$, which can be corrupted by noises.

With a linear parametric model, the recursive least squares algorithm is applied in an online fashion, as parameters are updated continuously by

$$\dot{\hat{\theta}} = P\epsilon(t)\phi(t), \tag{2.20}$$

$$\epsilon(t) = \frac{z(t) - \hat{\theta}^\top \phi(t)}{m^2(t)}, \tag{2.21}$$

$$\dot{P} = -P\frac{\phi\phi^\top}{m^2}P, \quad P(0) = P_0 \tag{2.22}$$

$$m^2(t) = 1 + \alpha\phi^\top(t)\phi(t), \quad \alpha > 0, \quad P_0 = P_0^\top \succ 0, \tag{2.23}$$

where $\hat{\theta}$ is the estimate of θ, $\alpha > 0$ is a scalar constant, and $P = P^\top \succ 0$ is a symmetric positive definite matrix.

Before running the above online parameter update law, a reasonable initialization $\hat{\theta}_0$ needs to be determined. For the initial offline parameter identification, particle swarm optimization (PSO) is employed to minimize the root mean squared error between the measured surface temperature and thermal model output. The initial thermal parameters identified by PSO are summarized in Table 2.1.

Table 2.1: Initial Thermal Parameters for an LFP Cell

C_c [J/K]	C_s [J/K]	R_c [K/W]	R_u [K/W]
59.5	4.4	1.61	3.14

Core Temperature & Heat Generation Estimation

We consider the following observer structure based on the thermal plant model (2.7)-(2.8):

$$\dot{\hat{x}}(t) = A\hat{x}(t) + Bu(t) + L\left[y(t) - \hat{y}(t)\right], \tag{2.24}$$

$$\hat{y}(t) = C\hat{x}(t), \tag{2.25}$$

where $\hat{x} = \begin{bmatrix}\widehat{T}_c & \widehat{T}_s\end{bmatrix}^\top$ denotes the estimated state vector, and $L = \begin{bmatrix}L_1 & L_2\end{bmatrix}^\top$, with $L_1, L_2 > 0$, is the observer gain vector to be designed. The following theorem provides the convergence results of the observer (2.24)-(2.25).

Theorem 1. *Consider the locally observable thermal system (2.7)-(2.8) with bounded heat generation $|\dot{Q}(t)| \le M_Q$, $\forall\ t \in \mathbb{R}^+$, and bounded model uncertainties $\nu < \overline{\nu}$, along with the observer (2.24)-(2.25). If there exists a gain matrix L and a positive definite matrix M such that*

$$(A - LC)^\top + (A - LC) = -M, \tag{2.26}$$

$$\lambda_{\min}(M)\|\tilde{x}(0)\| > 2\left(\overline{\Omega} + L\overline{n}\right), \tag{2.27}$$

then the state estimation error $\tilde{x}(t) = x(t) - \hat{x}(t)$ *remains bounded in the following sense as* $t \to \infty$*:*

$$\|\tilde{x}\| \leq R_b \triangleq \frac{2\left(\overline{\Omega} + L\overline{n}\right)}{\lambda_{\min}(M)}, \tag{2.28}$$

where $\overline{\Omega} = \|G\|M_Q + \|\overline{\nu}\|$ *and* $\lambda_{\min}(M)$ *denotes the minimum eigenvalue of matrix* M*.*

Theorem 1 leads to the notion of input-to-state (ISS) stability [31]. The proof for Theorem 1 is provided as follows.

Proof. Subtracting (2.24) from (2.7), the state estimation error dynamics can be written as

$$\begin{aligned}\dot{\tilde{x}}(t) = f(\tilde{x}) &= (A - LC)\tilde{x}(t) + G\dot{Q}(t) + \nu - Ln \\ &= (A - LC)\tilde{x}(t) + \Omega - Ln, \end{aligned} \tag{2.29}$$

where $\Omega = G\dot{Q}(t) + \nu$, and let $\|\Omega\| \leq \overline{\Omega} \triangleq \|G\|M_Q + \|\overline{\nu}\|$. As in [31], if there exists a class $\mathcal{KL}$ function $\beta(\cdot,\cdot)$ and a class $\mathcal{K}$ function $\gamma(\cdot)$, which is called a gain function, such that for any input $\dot{Q}(\cdot) \in L_\infty^m$ and any $\tilde{x}(0)$,

$$\|\tilde{x}(t)\| \leq \beta(\|\tilde{x}(0)\|, t) + \gamma(\|\dot{Q}(\cdot)\|_\infty), \tag{2.30}$$

then the system (2.29) is said to be ISS.

Consider the Lyapunov function candidate

$$V_1 = \tilde{x}^\top \tilde{x} = \|\tilde{x}\|^2, \tag{2.31}$$

The derivative of V along the trajectory of $\tilde{x}$ is

$$\begin{aligned}\dot{V}_1 &= \dot{\tilde{x}}^\top \tilde{x} + \tilde{x}^\top \dot{\tilde{x}} \\ &= [(A - LC)\tilde{x} + \Omega - Ln]^\top \tilde{x} + \tilde{x}^\top [(A - LC)\tilde{x} + \Omega - Ln] \\ &= \tilde{x}^\top [(A - LC)^\top + (A - LC)]\tilde{x} + 2\tilde{x}^\top(\Omega - Ln) \\ &\leq -\lambda_{\min}(M)\|\tilde{x}\|^2 + 2\|\tilde{x}\|\left(\overline{\Omega} + L\overline{n}\right) \\ &= -\lambda_{\min}(M)V_1 + 2\left(\overline{\Omega} + L\overline{n}\right)\sqrt{V_1}. \end{aligned} \tag{2.32}$$

Comparison principle [32] provides the solution to the differential inequality (2.32):

$$\|\tilde{x}\| \leq \|\tilde{x}(0)\| e^{-\frac{\lambda_{\min}(M)}{2}t} + \frac{2\left(\overline{\Omega} + L\overline{n}\right)}{\lambda_{\min}(M)}\left[1 - e^{-\frac{\lambda_{\min}(M)}{2}t}\right], \tag{2.33}$$

where M and $\|\tilde{x}(0)\|$ verify $\lambda_{\min}(M)\|\tilde{x}(0)\| > 2(\overline{\Omega} + L\overline{n})$. To satisfy the ISS condition, let

$$\beta(\|\tilde{x}(0)\|, t) = \|\tilde{x}(0)\|e^{-\frac{\lambda_{\min}(M)}{2}t}, \tag{2.34}$$

$$\gamma(\|\dot{Q}\|_\infty) = \frac{2\overline{\Omega}}{\lambda_{\min}(M)}\left[1 - e^{-\frac{\lambda_{\min}(M)}{2}t}\right], \tag{2.35}$$

and it is straightforward to show that β is a class $\mathcal{KL}$ function and γ is class $\mathcal{K}$. Hence we conclude that the system (2.29) is ISS. In addition, due to the exponentially decaying terms at right hand side of Eq. (2.33),

$$\|\tilde{x}\| \le R_b = \frac{2\left(\overline{\Omega} + L\overline{n}\right)}{\lambda_{\min}(M)} \text{ as } t \to \infty. \tag{2.36}$$

Therefore, with bounded unknown input $\dot{Q}$ and bounded uncertainties ν in thermal dynamics, $\|\tilde{x}\|$ will settle on or within a norm ball of radius R_b in the error space. ■

Remark 3. *The size of R_b may be reduced by optimally selecting gain L to balance convergence speed and robustness to uncertainty. A large L enlarges the denominator of R_b, but also amplifies the measurement noise in the numerator.*

According to [33], we can compute heat generation $\dot{Q}$ by inverting plant model dynamics (2.7). Nonetheless, we do not know the exact value of states $x(t)$. By using certainty equivalence [30], the unknown input estimate can be obtained by replacing the state $x(t)$ with its estimation $\hat{x}(t)$:

$$\widehat{\dot{Q}}(t) = G^\dagger\left(\dot{\hat{x}}(t) - A\hat{x}(t) - Bu(t)\right), \tag{2.37}$$

where $G^\dagger = (G^\top G)^{-1}G^\top$ is the left inverse of G. Heat generation estimation calculated in (2.37) will be utilized to design observers in Stage 2.

Remark 4. *There exists a loop between the two blocks in Stage 1. Specifically, the heat generation estimates are used for thermal parameter identification, and meanwhile the identified thermal parameters alter the system matrix A. Herein, we analyze each block separately, and only verify the stability of the coupling in the simulation.*

Stage 2: Battery SOC and Capacity Estimation

The Stage 2 simultaneously estimates battery SOC (unmeasured state) and capacity (unknown parameter) by receiving the core temperature and heat generation estimates from Stage 1 as input signals. We consider the following sliding mode observer structure for the

Stage 2:

$$\dot{\widehat{SOC}} = L_3 \cdot \operatorname{sgn}\left(OCV_m - \widehat{OCV}\right), \tag{2.38}$$

$$OCV_m = \frac{\widehat{\dot{Q}}}{I_m} + V_{T,m} + \widehat{T}\frac{dU}{dT}, \tag{2.39}$$

$$\widehat{T} = \frac{1}{2}\left(T_{s,m} + \widehat{T}_c\right), \tag{2.40}$$

where I_m, $V_{T,m}$, and $T_{s,m}$ are current, terminal voltage, and surface temperature measurements. Gain L_3 is the scalar observer gain to be designed. $\widehat{OCV}$ is the OCV estimation corresponds to SOC estimation $\widehat{SOC}$. Note that $\widehat{\dot{Q}}$ and $\widehat{T}_c$ are the estimated heat generation from (2.37) and estimated core temperature from (2.24). As analyzed in the previous section, the $\widehat{\dot{Q}}$ and $\widehat{T}_c$ estimation are biased due to thermal model uncertainties and unknown heat generation. Consequently, OCV_m obtained from (2.39) is biased. We model the uncertainty between OCV_m and the actual OCV by an additive error term ξ, with $OCV_m = OCV + \xi$. Note that ξ may also include the measurement noise from I_m and $V_{T,m}$. Under this scenario, we provide the convergence analysis of observer (2.38)-(2.40).

Theorem 2. *Consider the SOC dynamics (2.1), estimated heat generation and core temperature from Stage 1. Furthermore, assume OCV is a monotonically increasing function of SOC over domain* $0 \leq SOC \leq 1$. *Also, assume bounds* $M_I > 0, m_{C_{bat}} > 0$ *are known, where* $\left|I(t)\right| \leq M_I$, $\forall\ t \in \mathbb{R}^+$, $m_{C_{bat}} \leq C_{bat}$. *If the scalar observer gain* L_3 *verifies*

$$L_3 > \frac{M_I}{m_{C_{bat}}}, \tag{2.41}$$

then the estimation error $\widetilde{SOC}(t) = SOC(t) - \widehat{SOC}(t)$ *from observer (2.38)-(2.40) converges to an bounded error ball defined by* $\left|\widetilde{OCV}\right| \leq |\xi|$, *where* $\widetilde{OCV} = OCV - \widehat{OCV}$. *Furthermore, estimated battery capacity is given by*

$$\widehat{C}_{bat} = -\frac{I}{L_3 v}, \tag{2.42}$$

where v *is the filtered version of* $\operatorname{sgn}(OCV_m - \widehat{OCV})$, *computed by passing* $\operatorname{sgn}(OCV_m - \widehat{OCV})$ *through a low pass filter with unity steady-state gain in real time, i.e.* $v(t) = \{\omega/(s+\omega)\}\operatorname{sgn}(OCV_m(t) - \widehat{OCV}(t))$, *where* ω *is the cut-off frequency.*

Remark 5. *We have assumed that OCV is a monotonically increasing function of SOC over the 0%-100% SOC range. This assumption is verified for most of the popular Li-ion chemistry, e.g.* $LiCoO_2$ *-Graphite and* $LiFePO_4$*-Graphite [34].*

Proof. Under the condition of $\left|\widetilde{OCV}\right| > |\xi|$,

$$\operatorname{sgn}\left(OCV_m - \widehat{OCV}\right) = \operatorname{sgn}\left(\widetilde{OCV} + \xi\right) = \operatorname{sgn}\left(\widetilde{OCV}\right). \tag{2.43}$$

Strict monotonicity of the OCV-SOC relationship guarantees

$$\operatorname{sgn}\left(OCV - \widehat{OCV}\right) = \operatorname{sgn}\left(SOC - \widehat{SOC}\right). \tag{2.44}$$

Consequently, we can re-write observer (2.38) based on (2.44):

$$\dot{\widehat{SOC}} = L_3 \cdot \operatorname{sgn}\left(SOC - \widehat{SOC}\right). \tag{2.45}$$

The dynamics of $\widetilde{SOC} = SOC - \widehat{SOC}$ can be written as:

$$\dot{\widetilde{SOC}} = \dot{SOC} - \dot{\widehat{SOC}} = -\frac{I}{C_{bat}} - L_3 \operatorname{sgn}\left(\widetilde{SOC}\right). \tag{2.46}$$

We consider the following Lyapunov function candidate:

$$V_3(t) = \frac{1}{2}\widetilde{SOC}^2, \tag{2.47}$$

and the derivative of V_3 along the trajectories of $\widetilde{SOC}$ is

$$\begin{aligned} \dot{V}_3(t) &= \widetilde{SOC} \cdot \dot{\widetilde{SOC}} = \widetilde{SOC}\left[-\frac{I}{C_{bat}} - L_3 \cdot \operatorname{sgn}\left(\widetilde{SOC}\right)\right] \\ &= -\frac{I}{C_{bat}}\widetilde{SOC} - L_3 \cdot \operatorname{sgn}\left(\widetilde{SOC}\right) \cdot \widetilde{SOC} \\ &\le \frac{|I|}{C_{bat}}\left|\widetilde{SOC}\right| - L_3\left|\widetilde{SOC}\right| \\ &= \left|\widetilde{SOC}\right| \cdot \left(\frac{|I|}{C_{bat}} - L_3\right). \end{aligned} \tag{2.48}$$

Choose the gain L_3 high enough such that $L_3 > M_I/m_{C_{bat}}$. Furthermore, note from (2.47) and (2.48) that

$$\dot{V}_3 \le -\alpha\sqrt{2V_3}, \quad \text{where} \quad \alpha = L_3 - \frac{M_I}{m_{C_{bat}}}. \tag{2.49}$$

Applying the comparison principle on (2.49) suggests the finite time for $\widetilde{SOC}$ to converge to the error ball defined by $\left|\widetilde{OCV}\right| \le |\xi|$ to be $t_f = \sqrt{2V_3(0)}/\alpha$. Hence, based on the selection of some high gain L_3, $\dot{V}_3$ will decrease until $\left|\widetilde{OCV}\right| > |\xi|$ is violated. At the sliding mode, we have $\widetilde{SOC} = \varepsilon$, where ε is less than or equal to the size of the SOC error space corresponds to $\left|\widetilde{OCV}\right| < |\xi|$, and $\dot{\widetilde{SOC}} = 0$. Substituting these expressions in (2.46) yields:

$$\widehat{C}_{bat} = -\frac{I}{L_3 v}, \tag{2.50}$$

where $v(t)$ is the signal produced from low-pass filtering $\operatorname{sgn}\Big(OCV_m(t) - \widehat{OCV}(t)\Big)$. ■

Remark 6. *The battery capacity estimation computed from (2.50) is expected to be biased as a result of the Stage 1 estimation error ξ. Nevertheless, ξ can be reduced by optimally selecting observer gain L, based on Remark 3.*

Remark 7. *Given that the thermal parameters vary slowly, the lower block in Stage 1 operates on slow time scale (cycles) while the upper block and the entire Stage 2 evolve on a fast time scale (second).*

2.4 Benefits of Thermal model-based Capacity Estimation

The fundamental difference between the thermal based and the equivalent circuit based approach is that the thermal based scheme estimates capacity, thermal resistance, heat generation, temperature, and SOC without any need of output voltage model and estimates of R_s (internal resistance) and V_c (voltage of R-C pairs). In the equivalent circuit based SOH estimation, the SOH estimation error stems from the combined errors of capacity and internal resistance estimation. We hereby show conceptually how leveraging thermal dynamics enables to isolate away the estimation error of internal resistance. Essentially, we design an observer to estimate OCV using available online measurements.

Thermal model-based estimation: Consider the thermal model-based estimation scheme shown in Figure 2.1. In Stage 2, we use the estimated heat generation as the feedback signal in the observer. For a given input current profile and measured terminal voltage within a certain cycle, the heat generation estimation are given according to Eq. (2.4):

$$\hat{\dot{Q}}(t) = I_m(t)\left[\widehat{OCV}(t) - V_{T,m}(t) - \widehat{T}(t)\frac{dU}{dT}\right], \tag{2.51}$$

Subtract (2.51) from (2.4), the feedback error signal is given as

$$\tilde{\dot{Q}}(t) = I(t)\left[\widetilde{OCV}(t) - \widetilde{T}(t)\frac{dU}{dT}\right], \tag{2.52}$$

Assume $\widetilde{T}(t)$ is negligible due to robust temperature estimation in Stage 1, and the feedback error signal becomes:

$$\tilde{\dot{Q}}(t) = I(t)\cdot\widetilde{OCV}(t), \tag{2.53}$$

which captures OCV estimation error only, which is in turn dependent only on the capacity estimation error.

Electrical model-based estimation: In this case, we use terminal voltage as the feedback signal. Consequently, the feedback error signal is given as

$$\widetilde{V}_T(t) = \widetilde{OCV}(t) - \widetilde{V}_c(t) - I(t)\widetilde{R}_s, \tag{2.54}$$

where $\widetilde{V}_T$, $\widetilde{V}_c$, and $\widetilde{R}_s$ are the estimation errors for the terminal voltage, voltage across R-C pairs, and the internal resistance. Under this scenario, the estimation errors for capacity ($\widetilde{OCV}$) and internal resistance ($\widetilde{R}_s$) both emerge.

Methods that estimate capacity and internal resistance from an equivalent circuit perspective, e.g. [19], need crucial assumptions, e.g. linearly varying capacity and internal resistance with respect to time, to distinguish the estimation errors of capacity and internal resistance. However, the thermal based estimation completely decouples capacity estimation error from the combined SOH estimation error without requiring any such restrictive conditions.

Moreover, though the primary objective for this work is real-time battery charging capacity estimation, the algorithm presented in this chapter can be considered as a novel methodology for combined SOC/SOH estimation. Specifically, it provides estimates for SOC and charge capacity. Even more, Stage 1 produces estimates for thermal model parameters, core temperature, and internal heat generation. To the best of our knowledge, this is the first estimation framework in the literature to estimate all the aforementioned states and parameters simultaneously, with provable convergence properties, under suitable conditions.

2.5 Results and Discussion

We present studies on simulation and experiments to validate the performance of the proposed capacity estimation scheme. The battery under test is a $LiFePO_4/LiC_6$ A123 26650 cell with initial capacity of 2.3 Ah.

Simulation Study

This section presents the simulation study. The parameter values for thermal model (2.2)-(2.3) are taken from [11]. To illustrate the performance, we apply a driving cycle to the battery model. The left plots in Figure 2.2 demonstrate the evolution of input current and output terminal voltage from the plant model simulation. The estimates (unknown states, input, and parameter) are initialized with incorrect values to illustrate the convergence properties.

We first evaluate the performance of observer (2.24)-(2.25) and (2.37) in Stage 1. The core temperature estimate is initialized with 3°C error. Figure 2.2 portrays the evolution of the unknown state (T_c) and unknown input ($\dot{Q}$) from the simulation of thermal system

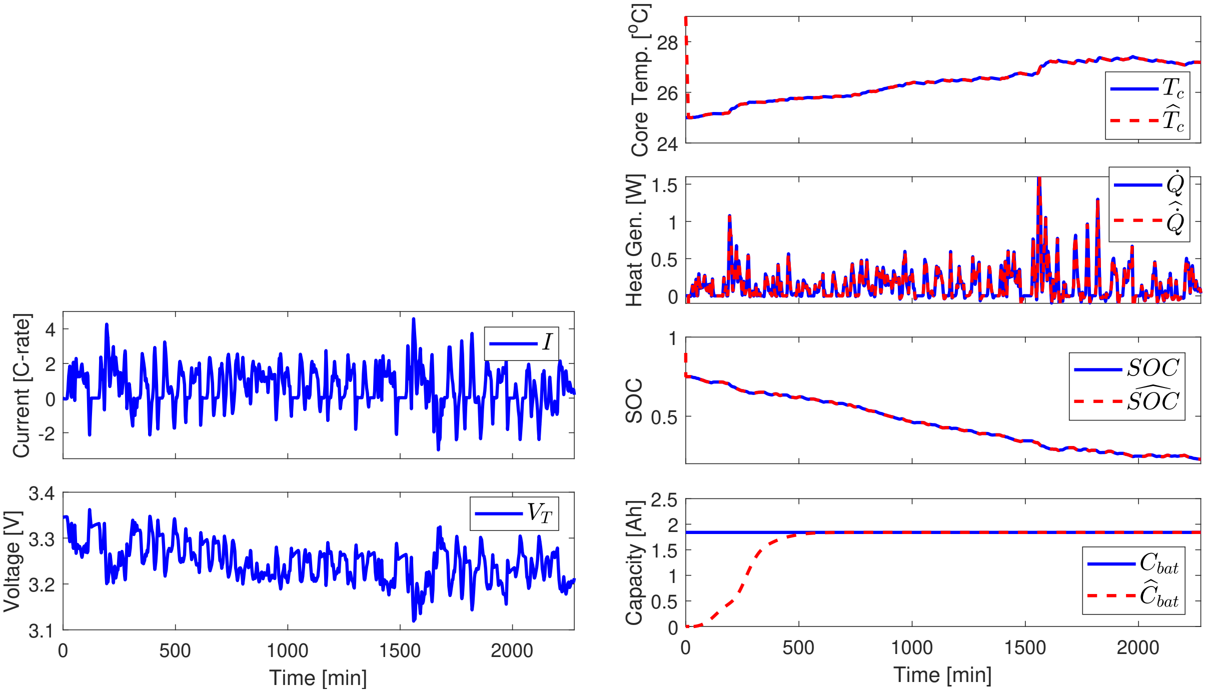

Figure 2.2: **Left:** Input current and output terminal voltage in the plant model. **Right:** Estimation performance for the charge-discharge cycle in simulation study, for core temperature, heat generation, SOC, and capacity.

(2.2)-(2.3), with their estimated values. Note that with an appropriate choice of observer gain L as presented in Theorem 1, $\widehat{T}_c$ and $\widehat{\dot{Q}}$ converge rapidly. Similarly the effectiveness of SOC and capacity (C_{bat}) estimation are investigated by initializing SOC estimate with 15% initial error. These results from Figure 2.2 confirm the finite-time convergence analysis conclusions for the Stage 2 observers in Section 2.3.

Experimental Studies

We further illustrate the proposed algorithm on experimentally obtained capacity data. The battery cell was placed inside of an ESPEC BTL-433 environmental chamber that maintains the ambient temperature at 25.5^oC (298.65 K). A thermocouple was attached to the surface of the cell to measure sueface temperature. A PEC SBT2050 cycler was used to apply a repeated charge-discharge cycle (a charging protocol based on SPMeT model - Fig. (10) in [35]) to the battery cell to induce aging (see left plots in Figure 2.3). The effect of battery aging on terminal voltage and surface temperature is noticeable, especially towards the final 50 cycles, where the cell experiences higher voltage and temperature changes for the same input.

Figure 2.3, on the right, shows the charge-discharge profile for the first cycle, along with the measured voltage (V_T) and surface temperature (T_s). The cell is first charged under

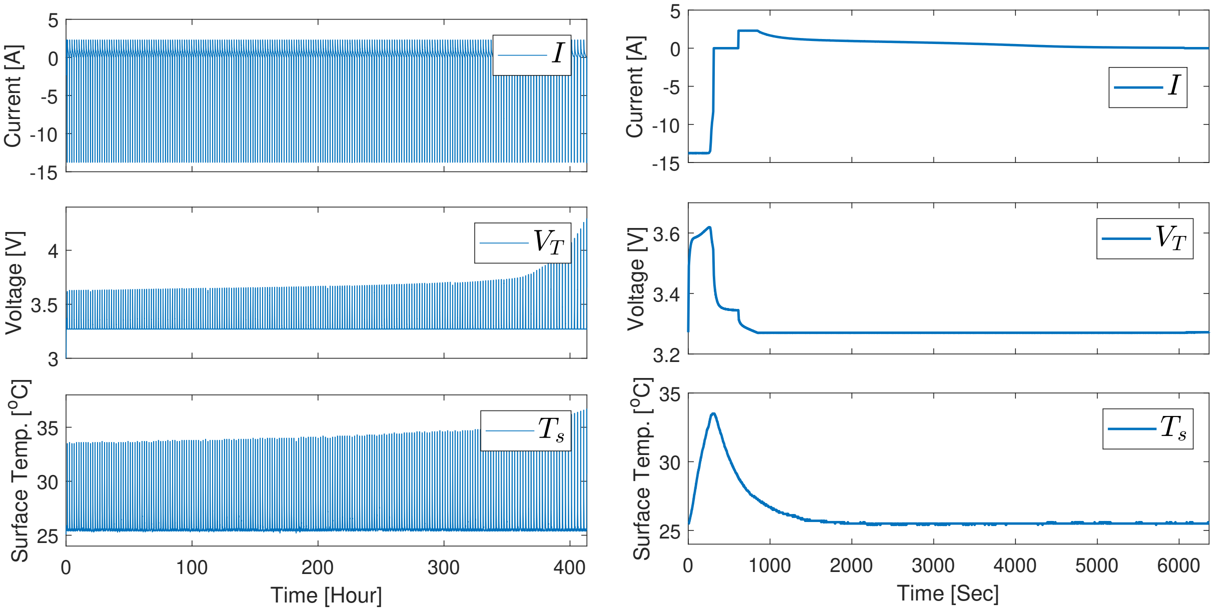

Figure 2.3: **Left:** Experimental data of a repeated charge-discharge profile for 210 cycles, including measurements of input current (I), output terminal voltage (V_T) and surface temperature (T_s). **Right:** The first cycle of the charge-discharge profile.

$I_{\max} = 6C$ constant current for 300 seconds which elevates SOC from initial value 25% to final value 75%, followed by a 300-second resting period ($I = 0$). In the discharge phase, the current initially holds constant but eventually decays over time, resulting in a constant voltage discharge. The capacity was determined using a 1C Constant Current-Constant Voltage (CC-CV) cycling test at cycle numbers {0, 10, 60, 110, 160, 210}. For real-time implementation, accurate parameter estimation in the thermal model plays a critical role in capacity estimation, due to the fact that the uncertainties in heat generation estimation and OCV_m could accumulate error, since a large portion (nearly 85%) of OCV plot lies in the flat region of OCV-SOC curve. Put simply, the SOC estimation is sensitive to OCV_m uncertainty.

Here, we demonstrate the estimation performance for the first charge-discharge cycle. The SOC estimate is initialized with 30% error and capacity estimate is initialized with 0.3 Ah (13%) error. Figure 2.4 presents the convergence of SOC and capacity estimates to their true values. The blue solid line in the upper figure represents the evolution of SOC generated by coulombic counting method. The value of measured battery capacity (2.31 Ah) is shown in the lower figure in blue.

Finally, we examine the capacity estimation performance across 210 cycles under two scenarios.

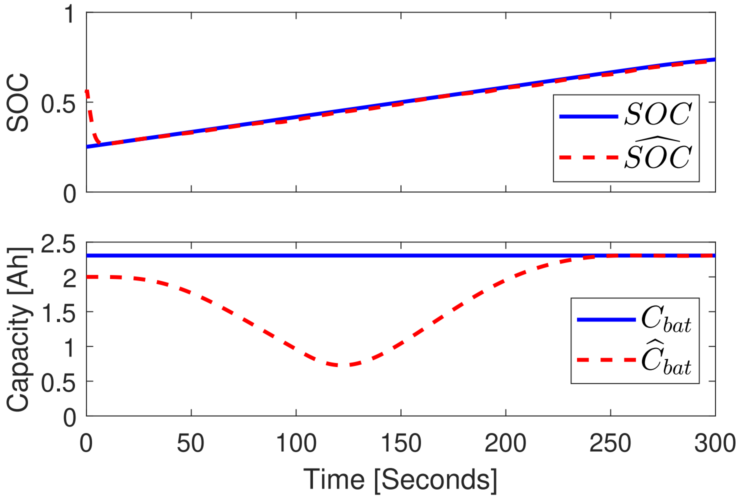

Figure 2.4: Evolution of true/estimated SOC and battery capacity (C_{bat}) for the charge period of the first charge-discharge cycle.

Effect of updating R_c in real time.

Figure 2.5(a) plots the values of R_c every five cycles as black dots. In spite of the apparent uncertainties stemming from the noisy experimental measurements, the trend of R_c over cycles bears accelerated growth behavior, especially towards the end of the experiments. The frequency for updating R_c (every 5 cycles) is somewhat arbitrary, but it is selected to adequately track the change rate. We explicitly evaluate the estimation results by comparing two cases: (i). when R_c is updated online, and (ii). when R_c remains at the value from the first cycle throughout the experiments. Specifically in Figure 2.5(b), the blue and green plus symbols ('+') represent the estimated capacities from case (i) and case (ii). Moreover, the red star symbols ('*') are the six capacity measurements, and the black dotted line is the fitted curve using the measured data. Note that both cases follow the black curve closely until R_c starts to deviate. Ultimately, after cycle 180, the estimation from case (ii) without R_c being updated experiences more disturbances and reveals relatively larger error. The same observation can be made in Figure 7(c) where the percentage errors of capacity estimation from both cases against the experimentally fitted values are plotted.

Effect of measurement uncertainties.

Despite the fact that the cycled data are experimentally collected, the measurement signals are in fact accurate and almost noise-free. In order to mimic the real-world applications, a 2% random error is manually added to the signals from Figure 2.3 to validate the robustness of the estimation scheme. One may clearly observe from Figure 2.5(d) that the capacity estimation result indeed suffers from errors. According to Remark 3, the observer gain L is supposed to be selected to appropriately balance the convergence rate and robustness to

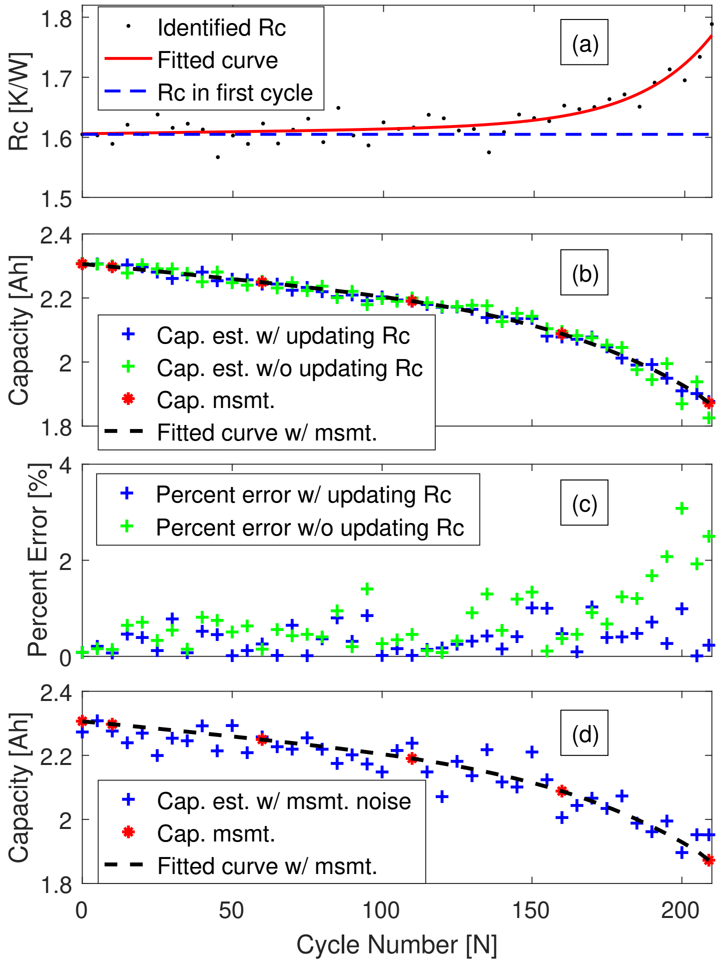

Figure 2.5: Battery capacity estimation results, plotted every five cycles. Figure (a) presents the evolution of R_c, and (b) and (c) suggest a more accurate estimation with updating R_c in real time. Figure (d) depicts the observer robustness against the measurement noise.

measurement noise to minimize the size of R_b. Here, the maximum percentage error between the estimates and the fitted capacity curve is 4.7%.

2.6 Conclusions

This chapter rigorously analyzes an online capacity estimation scheme for Li-ion batteries from a thermal prospective. Stage 1 estimates core temperature, heat generation, and thermal resistance based on a two-state thermal model, and the second stage receives these estimation signals to estimate SOC and capacity utilizing a sliding mode observer. The convergence for the observers are mathematically analyzed using Lyapunov stability theory. This approach only requires the tuning of three scalar observer gains, wheres the number of tuning parameters in commonly adopted KF based methods is polynomial with respect to the number of states. Experimental results demonstrate the capacity estimation accuracy and robustness by comparing with real data. The benefit of using thermal dynamics for capacity estimation is that it decouples capacity estimation error from the combined SOH estimation error.

Chapter 3

Battery Adaptive Observer for a Single Particle Model with Intercalation-Induced Stress

3.1 Introduction

Safe operation and degradation of Li-ion batteries have always been critical especially when the usage of batteries gets ubiquitous. Battery models are typically used in a BMS for inferring internal states based on measured current, voltage and temperature [36, 37]. The equivalent circuit models possess simple structure but sacrifice the information of internal states, while high-fidelity electrochemical models can capture the underlying physical and chemical processes [38]. Though electrochemical models accurately predict the internal states, their mathematical structures are often very complicated for control/estimation design. This point motivates model reduction techniques to reduce the complexity of full order electrochemical models. Among the numerous reduced order models, the single particle model (SPM) is the most commonly used one. The SPM is derived from the full order electrochemical model, and hence it inherits some important properties. Each electrode of the SPM is assumed to be a single spherical particle and the current distribution is uniform across both electrodes. In addition, the electrolyte concentration is assumed to be constant in space and time [37]. Based on the SPM, Kalman filter (KF) for SOC estimation was designed in [39, 40]. The shortcoming of KF approaches arise from the difficulties to verify the asymptotic convergence properties. The authors of [41] proposed a SOC estimation technique using the SPM, where the radial-domain dependence of solid phase lithium concentration is approximated by a fourth-order polynomial. One of the important drawbacks of the SPM is that it does not accurately predict voltage at high C-rate[1], since the electrolyte dynamics are neglected. In order to compensate this, models that combine the SPM with other components

---

[1] C-rate is a normalized measure of electric current. It is defined as the ratio of current in Amperes (A) to a cell's nominal capacity in Ampere-hours (Ah).

are developed. For instance, electrolyte phase contribution are approximated by polynomial functions in [42]. State estimation scheme with provable convergence for the SPM with electrolyte dynamics is derived and analyzed in [43]. Temperature distribution inside the battery is a crucial quantity for thermal management in BMS. An electrochemical model coupled with electrolyte dynamics and temperature dependent parameters is presented for SOC estimation [44]. Battery SOC and internal temperature are estimated from a reduced and reformulated electrochemical model in [45].

In recent years, battery SOH has gained increased focus due to concerns over battery safety and life. Various factors contribute toward battery degradation, e.g. capacity fade and resistance growth. See [13] for a particularly excellent review. Though simultaneous SOC and SOH estimation problem has been well-studied using circuit models [19, 46, 47], it is less examined for electrochemical models. Moura *et al.* created an adaptive PDE observer for combined SOC and SOH estimation by adopting PDE backstepping observer design procedure [48]. A nonlinear Luenberger-type adaptive observer is designed on a coupled electrochemical-thermal model in [49]. In the aforementioned papers, certain parameters, e.g. diffusion coefficient and contact resistance, are used as indicators of SOH, and these parameters are identified in real time.

Other than the model parameter dependent health indicator for Li-ion batteries, this chapter inspects another quantity for studying battery health, namely the intercalation-induced stress generated inside the solid phase particles. An important capacity fade mechanism is the particle fracture due to intercalation- and deintercalation-induced stresses [50]. Volume changes of the electrode particles due to stress generation may induce particle fracture if the stress (radial or tangential [51, 52]) exceeds the yielding stress of the material [53]. This phenomenon motivates the development of models that incorporate stress mechanics into the SPM. Seminal work conducted by Christensen and Newman developed a mathematical model to capture volume expansion and contraction during lithium insertion [53]. Later, models that combine the SPM with diffusion-induced stress was introduced in [54], relying on an analogy to thermal stress. In [55], a modified SPM that incorporates stress-enhanced diffusion and electrolyte concentration distribution was developed. This model strikes an intriguing balance of fidelity and structural simplicity. An interesting BMS application of these models is introduced in [56], where the authors performed optimal charging under stress constraints. It is worth noting that spatial non-uniformity in battery electrode can cause degradation even when operating within the manufacturer specified limits. Although applying the SPM-based model for battery SOH estimation and monitoring can not capture this spatial distribution of degradation patterns due to heterogeneities in electrode geometry [57], we seek quantitative aggregated stress prediction to better understand battery SOH in this chapter.

In summary, there now exists a keen interest to address the SOH estimation problem, and recent model developments on diffusion induced stress can be enabling. However, no work currently exists on state and parameter estimation with coupled SPM-Stress models to the authors' best knowledge. In this chapter, we design a nonlinear observer based on this coupled model to estimate the bulk SOC, the particle stress profile, and the anode lithium diffusivity from current and voltage measurements only [58]. Consequently, the real-time electrochemical model parameter can be monitored as a battery health indicator, and the electrode stress supports the studies on several physical degradation phenomena associated with battery health. This contribution departs from existing works in estimation for battery electrochemical models in the following ways:

- It makes one of the first attempts to exploit the stress-enhanced electrochemical model for the estimation of internal stress on top of SOC and model parameters. This issue is relevant for batteries consisting of electrodes that tend to expand and fracture due to stress.
- It considers a nonlinear state dynamical model stemming from intercalation-induced stress effects, which contrasts with linear state dynamics in [48, 49].
- A sliding mode observer based adaptive estimation scheme is proposed, which differs from e.g. output inversion and least squares estimation [48]. The used observer is known to be robust against model uncertainties.
- It performs state and parameter estimation simultaneously while providing convergence conditions for the proposed estimation scheme through a rigorous stability analysis.

The remainder of the chapter is organized as follows: Chapter 3.2 presents the battery single particle model with intercalation-induced stress. Chapter 3.3 motivates the importance of monitoring the electrode stress via a simulation example. Chapter 3.4 discusses model properties, model reduction, and state-space model formulation. The observer design with convergence analysis is presented in Chapter 3.5. Chapter 3.6 demonstrates the performance of designed observer via simulation and utilizing experimental data. The limitations of the proposed scheme and future work are enumerated in Chapter 3.7. Finally, conclusions are drawn in Chapter 3.8.

3.2 Model Description

Figure 3.1 portrays the concept of the SPM. In the full order electrochemical model (*a.k.a.* Doyle-Fuller-Newman model [38]), Li-ion transports in the solid and electrolyte phases. The key idea of the SPM is that the solid phase of each electrode can be modeled as a single spherical particle, and Li-ion concentration in electrolyte phase is assumed to be constant in space and time [48]. The SPM captures less dynamic behavior than the full order model, and specifically does not include mechanical responses, whose effect on diffusion becomes significant when the electrode material has high modulus and high partial molar volume [54].

The model equations for the coupled SPM and stress presented here closely follow the derivation by Zhang *et al.* [54]. A list of description for symbols can be found in Table 3.1.

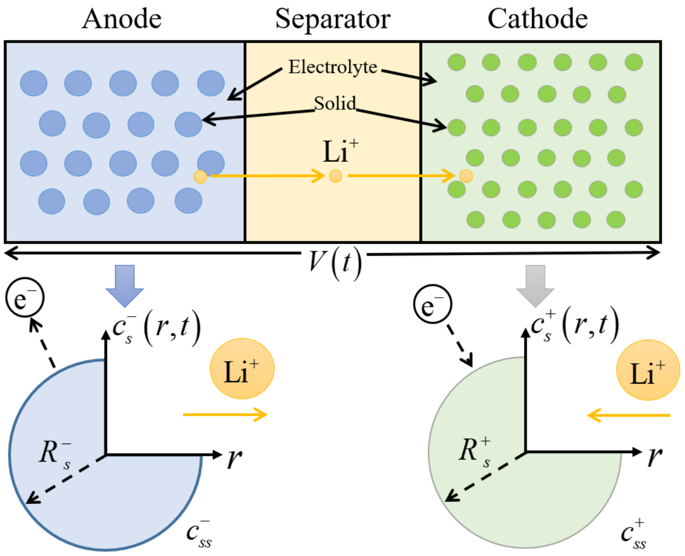

Figure 3.1: Sketch of the Single Particle Model (SPM) Concept

For the case of a two dimensional spherical particle, the intercalation of Li-ions in the solid phase is modeled as a process due to diffusion and stress generation, given by

$$\frac{\partial c_s^j}{\partial t} = D_s^j \left[\frac{\partial^2 c_s^j}{\partial r^2} - \frac{\Omega^j}{RT}\frac{\partial c_s^j}{\partial r}\frac{\partial \sigma_h^j}{\partial r} - \frac{\Omega^j}{RT} c_s^j \left(\frac{\partial^2 \sigma_h^j}{\partial r^2} + \frac{2}{r}\frac{\partial \sigma_h^j}{\partial r}\right)\right], \tag{3.1}$$

with the boundary condition

$$-D_s^j \left[\frac{\partial c_s^j}{\partial r}(R_s^j,t) - \frac{\Omega^j}{RT} c_s^j(R_s^j,t)\frac{\partial \sigma_h^j}{\partial r}(R_s^j,t)\right] = \frac{i_n^j(t)}{F}, \tag{3.2}$$

where $c_s^j = c_s^j(r,t) : [0, R_s^j] \times [0,\infty) \to \mathbb{R}$ maps the radial position and time to solid phase lithium concentration in electrode j, and $\sigma_h^j = \sigma_h^j(r,t) : [0, R_s^j] \times [0,\infty) \to \mathbb{R}$ maps the radial position and time to hydrostatic stress in electrode j. The current density i_n^j is proportional to the input current by the relation $i_n^j(t) = \pm I(t)/a^j A L^j$.

The stress tensor consists of radial stress σ_r and tangential stress σ_t, which are functions of the lithium concentration:

$$\sigma_r^j(r,t) = 2\beta^j \left[\frac{1}{(R_s^j)^3}\int_0^{R_s^j} \tilde{c}_s^j r^2 dr - \frac{1}{r^3}\int_0^r \tilde{c}_s^j \rho^2 d\rho\right], \tag{3.3}$$

$$\sigma_t^j(r,t) = \beta^j \left[\frac{2}{(R_s^j)^3}\int_0^{R_s^j} \tilde{c}_s^j r^2 dr + \frac{1}{r^3}\int_0^r \tilde{c}_s^j \rho^2 d\rho - \tilde{c}_s^j\right], \tag{3.4}$$

Table 3.1: SPM-Stress Model Symbol Description

Symbols	Description	Units
a^j	Specific interfacial surface area	$[\mathrm{m}^2/\mathrm{m}^3]$
A	Cell cross Chapteral area	$[\mathrm{m}^2]$
c_e^0	Li-ion concentration in electrolyte phase	$[\mathrm{mol}/\mathrm{m}^3]$
c_s^j	Solid phase Li-ion concentration	$[\mathrm{mol}/\mathrm{m}^3]$
c_{ss}^j	Li-ion concentration at particle surface	$[\mathrm{mol}/\mathrm{m}^3]$
$c_{s,\max}^j$	Max Li-ion concentration in solid phase	$[\mathrm{mol}/\mathrm{m}^3]$
$\tilde{c}_s^j$	Concentration change from stress-free value	$[\mathrm{mol}/\mathrm{m}^3]$
D_s^j	Solid phase diffusion coefficient	$[\mathrm{m}^2/\mathrm{sec}]$
E^j	Young's Modulus	[GPa]
F	Faraday's constant	[C/mol]
i_n^j	Particle surface current density	$[\mathrm{A}/\mathrm{m}^2]$
I	Applied current	[A]
k^j	Charge transfer reaction rate	$[\mathrm{A}\cdot\mathrm{m}^{2.5}/\mathrm{mol}^{1.5}]$
L^j	Electrode thickness	[m]
$n_{Li,s}$	Lithium in the solid phase	[mol]
r	Radial coordinate	[m]
R	Universal gas constant	[J/mol-K]
R_f	Contact film resistance	[Ohm]
R_s^j	Particle radius	[m]
t	Time	[Second]
T	Battery cell temperature	[K]
U^j	Open circuit potential	[V]
$\Theta_{\min}^j$	Lower stoichiometry point	[-]
$\Theta_{\max}^j$	Upper stoichiometry point	[-]
α^j	Charge transfer coefficient	[-]
ε_s^j	Volume fraction of solid phase	[-]
ν^j	Poisson's ratio	[-]
σ_h^j	Hydrostatic stress	[MPa]
Ω^j	Partial molar volume	$[\mathrm{mol}/\mathrm{m}^3]$

where $\beta^j = \Omega^j E^j / 3(1-\nu^j)$. The hydrostatic stress is a weighted sum of σ_r and σ_t:

$$\sigma_h^j = \frac{\sigma_r^j + 2\sigma_t^j}{3} = \frac{2}{3}\beta^j \left[\frac{3}{(R_s^j)^3} \int_0^{R_s^j} \tilde{c}_s^j r^2 dr - \tilde{c}_s^j \right]. \tag{3.5}$$

Substituting (3.5) into (3.1) yields

$$\frac{\partial c_s^j}{\partial t} = D_s^j \left[(1+\theta^j c_s^j)\left(\frac{\partial^2 c_s^j}{\partial r^2} + \frac{2}{r}\frac{\partial c_s^j}{\partial r}\right) + \theta^j \left(\frac{\partial c_s^j}{\partial r}\right)^2 \right], \tag{3.6}$$

where $\theta^j = (\Omega^j/RT)[(2\Omega^j E^j)/9(1-\nu^j)]$ is a constant depending on electrode material mechanical properties. The boundary condition is obtained by substituting (3.5) into (3.2):

$$-D_s^j \left(1+\theta^j c_s^j(R_s^j,t)\right) \frac{\partial c_s^j}{\partial r}(R_s^j,t) = \frac{\pm I(t)}{F a^j A L^j}. \tag{3.7}$$

For well-posedness, the Neumann boundary condition at $r=0$ is required:

$$\frac{\partial c_s^j}{\partial r}(0,t) = 0. \tag{3.8}$$

The two variables, concentration and stress involved in PDE (3.1), are decoupled into a single nonlinear PDE (3.6) that describes the diffusion of Li-ion under the influence of stress, and concentration-dependent radial and tangential stresses in (3.3) and (3.4). Therefore, the dynamical equation for the solid phase Li-ion concentration with intercalation-induced stress is given by (3.6), with the boundary conditions (3.7)-(3.8). The nonlinearities in PDE (3.6) can be regarded as a diffusion with state-dependent diffusivity as well as a square of the spatial derivative of the state. Note that the intercalation-induced stress effect is ignored if $\theta^j = 0$, resulting in the regular SPM.

The output terminal voltage V_T is a function of solid phase surface concentration, open circuit potentials, electric overpotentials, and Butler-Volmer kinetics:

$$\begin{aligned} V_T(t) = {} & \frac{RT}{\alpha^+ F}\sinh\left[\frac{-I(t)}{2a^+AL^+ i_0^+(c_{ss}^+(t))}\right] - \frac{RT}{\alpha^- F}\sinh\left[\frac{I(t)}{2a^-AL^- i_0^-(c_{ss}^-(t))}\right] \\ & + U^+(c_{ss}^+(t)) - U^-(c_{ss}^-(t)) - R_f I(t), \end{aligned} \tag{3.9}$$

where the exchange current density $i_0^j(\cdot)$ is

$$i_0^j(c_{ss}^j) = k^j \sqrt{c_e^0 c_{ss}^j(t)(c_{s,\max}^j - c_{ss}^j(t))}, \tag{3.10}$$

$$c_{ss}^j(t) = c_s^j(R_s^j, t). \tag{3.11}$$

$U^+(\cdot)$ and $U^-(\cdot)$ in Eq. (3.9) are the equilibrium potentials of positive and negative electrode material as functions of solid phase surface concentrations.

3.3 Motivation

In this section, we illustrate the importance of monitoring stress inside the electrode solid particle via a simulation study. The model parameters are identified from the experimental data presented in Figure 3.5(a) in Chapter 3.6, and they correspond to a commercial

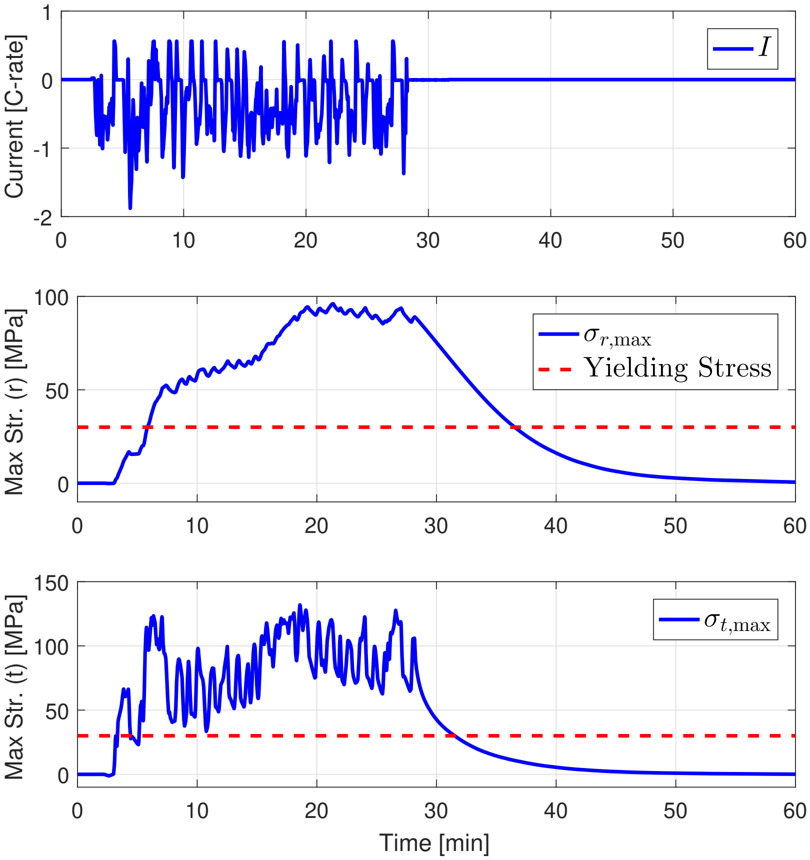

Figure 3.2: Maximum radial and tangential stresses for a commercial NMC cell under UDDS cycle loads

$LiNiMnCoO_2$ (NMC) - LiC_6 cell. A transient electric vehicle-like charge/discharge cycle generated from urban dynamometer driving schedule (UDDS) is applied, and the maximum absolute radial and tangential stresses for anode (graphite) are simulated and plotted in Figure 3.2. The maximum absolute radial and tangential stresses are located at the center and the surface of the electrode particle, respectively [54], and they are dependent on the change of radial Li-ion concentration from its stress-free value:

$$\sigma^-_{r,\max}(t) = 2\beta^- \left[\frac{1}{(R_s^-)^3}\int_0^{R_s^-} \tilde{c}_s^- r^2 dr - \frac{1}{3}\tilde{c}_s^-(0,t)\right], \tag{3.12}$$

$$\sigma^-_{t,\max}(t) = \beta^- \left[\frac{3}{(R_s^-)^3}\int_0^{R_s^-} \tilde{c}_s^- r^2 dr - \tilde{c}_s^-(R_s^-,t)\right]. \tag{3.13}$$

The dotted red lines in Figure 3.2 represent the yielding stress for graphite. It is evident that the yielding stresses of materials are generally lowered by repeated cycling, and it is possible that the yielding stress of carbonaceous materials will fall below 30 MPa when the cell is cycled [53]. Consequently, the maximum absolute radial and tangential stresses exceed the yielding stress at approximately 4 minutes and 1.2 minutes after the current switches to non-zero value, respectively. The anode particle may fracture during the large portion of this driving cycle since the maximum stresses are significantly higher than the yielding stress. Hence, from the safety point of view, the users of the BMS shall greatly benefit from the real-time particle stress information to ensure safe operation and longevity of the battery.

Remark 8. *The electrode particles are very likely to fracture if the maximum stresses exceed the yielding stress of the electrode material. However, the stresses at which particles actually fracture may greatly vary, and the yielding stress of the material is an upper limit on the stress required for particle fracture. It is possible to fracture during cycling even when the maximum stress is below the yielding stress [59]. Although the exact condition for particles to fracture may not be determined, criteria for electrode fracture tendency have been identified in [52], namely strength-based and energy-based criteria.*

3.4 Model Analysis and Reduction

This Chapter presents model properties, system observability analysis, and state-space formulation for observer design.

Conservation of solid-phase lithium

The moles of lithium in the solid phase $n_{Li,s}$ is conserved, where

$$n_{Li,s}(t) = \sum_{j\in\{+,-\}} \frac{\varepsilon_s^j L^j A}{\frac{4}{3}\pi (R_s^j)^3} \int_0^{R_s^j} 4\pi r^2 c_s^j(r,t)dr. \tag{3.14}$$

The lithium conservation can be verified by differentiating (3.14) with respect to time:

$$
\begin{aligned}
\frac{d}{dt} n_{Li,s} &= \sum_{j\in\{+,-\}} \frac{\varepsilon_s^j L^j A}{\frac{4}{3}\pi (R_s^j)^3} \int_0^{R_s^j} 4\pi r^2 \frac{\partial c_s^j(r,t)}{\partial t} dr \\
&= \sum_{j\in\{+,-\}} \frac{D_s^j \varepsilon_s^j L^j A}{\frac{4}{3}\pi (R_s^j)^3} \int_0^{R_s^j} 4\pi r^2 \left[\theta^j \left(\frac{\partial c_s^j}{\partial r} \right)^2 \right. \\
&\quad \left. + (1 + \theta^j c_s^j) \left(\frac{\partial^2 c_s^j}{\partial r^2} + \frac{2}{r} \frac{\partial c_s^j}{\partial r} \right) \right] dr \\
&= \sum_{j\in\{+,-\}} \frac{3 D_s^j \varepsilon_s^j L^j A}{R_s^j} \left[(1 + \theta^j c_s^j(R_s^j,t)) \frac{\partial c_s^j(R_s^j,t)}{\partial r} \right] \\
&= \sum_{j\in\{+,-\}} -\frac{3 D_s^j \varepsilon_s^j L^j A}{R_s^j} \frac{\pm I}{D_s^j F a^j A L^j} \\
&= \frac{I}{F} - \frac{I}{F} = 0,
\end{aligned}
\tag{3.15}
$$

where the second equality comes from the dynamical equation (3.6), the third equality follows from integration by parts, the fourth equality results from the boundary conditions (3.7), and the last equality utilizes the relation $\varepsilon^j = a^j R_s^j/3$.

The lithium conservation property will be leveraged for model reduction in the next section.

Model Reduction

The cell voltage in (3.9) depends on $U^+(c_{ss}^+) - U^-(c_{ss}^-)$, which makes the difference of the open circuit potential observable from the voltage measurement but does not guarantee the observability of each open circuit potential [40]. This chapter adopts the idea in [40] to overcome this issue by seeking a relation between the positive and negative solid phase surface concentrations by the lithium conservation property in (3.14):

$$
c_{ss}^+ = \frac{n_{Li} - \varepsilon_s^- L^- A c_{ss}^-}{\varepsilon_s^+ L^+ A},
\tag{3.16}
$$

and the output function (3.9) can be adjusted accordingly:

$$
\begin{aligned}
V_T(t) = {} & \frac{RT}{\alpha^+ F} \sinh\left[\frac{-I(t)}{2a^+ A L^+ i_0^+(\gamma c_{ss}^-(t) + \kappa)} \right] - \frac{RT}{\alpha^- F} \sinh\left[\frac{I(t)}{2a^- A L^- i_0^-(c_{ss}^-(t))} \right] \\
& + U^+(\gamma c_{ss}^-(t) + \kappa) - U^-(c_{ss}^-(t)) - R_f I(t),
\end{aligned}
\tag{3.17}
$$

where $\gamma = -(\varepsilon_s^- L^-)/(\varepsilon_s^+ L^+)$ and $\kappa = n_{Li}/(\varepsilon_s^+ L^+ A)$. The reduced system is then modeled by the anode dynamics (c_s^--system) from diffusion equation (3.6) and output function (3.17).

Ideally, we intend to check the observability of the reduced nonlinear PDE system (3.6) and (3.17), but the theoretical results of the PDE system observability is not well-developed, and as a result we discretize the PDE system into a system of ODEs in the subsequent Chapter and evaluate the local observability of the spatially discretized system.

Remark 9. *In the present work, we introduce state and parameter observer for the graphite anode in particular. Although the above model reduction is motivated by the observability condition from control theory perspective, the anode selection arises from the physics. The graphite anodes are prone to degradation due to volume changes and concentration gradients [60, 61, 62], and such degradation results in diffusion-induced stress that might lead to particle fracture [53, 63].*

State-Space Model Formulation and Analysis

There is a growing but small body of theoretical results on adaptive estimation of parabolic PDEs. For instance, an extended Luenberger-type observer is designed for a class of semi-linear parabolic PDEs in [64], achieving exponential stability of the linearized observer error dynamics. However, the model therein reflects only semi-linearity and no parameter uncertainties. The methods introduced in [65] stands out as it provides a thorough analysis and proof of adaptive scheme using output feedback for linear parabolic PDEs with spatially varying coefficients. Nonetheless, this approach doesn't directly extend to this chapter as the SPM-Stress model contains highly nonlinear components. In [66], the authors developed an adaptive boundary observer for parabolic PDEs with both domain and boundary parameter uncertainties, with convergence results, where the PDE is linear in the states and parameters, making it more tractable for the backstepping technique. In the context of battery applications, Ascencio derives an adaptive PDE observer for the SPM, including a parameter estimate for the diffusion coefficient [67]. Sum-of-squares programming is used for solving the kernel PDE online. Although these results have advanced our understanding of adaptive estimation for parabolic PDEs in infinite dimensional space, the considered problem in this chapter is still extremely difficult. Hence, we use model discretization so that finite dimensional estimation tools can be leveraged.

Henceforth, we will only consider dynamics for anode and drop the subscripts and superscripts to simplify notation, namely $c = c_s^-$, $D = D_s^-$, $R_s = R_s^-$, $a = a^-$, $L = L^-$, and $\theta = \theta^-$. Suppose $(N+1)$ nodes are used for discretization in the r direction, and $\Delta r = R_s/N$. Define the parameter

$$\tau = \frac{D}{(\Delta r)^2}. \tag{3.18}$$

The central difference method is used for discretizing the PDEs into ODEs. The system of ODEs for the internal nodes of the anode diffusion dynamics are

$$\frac{\partial c_i}{\partial t} = \tau \left[(1+\theta c_i)(c_{i-1} - 2c_i + c_{i+1}) + \left(\frac{2}{i} + \theta \frac{c_{i+1} - c_{i-1}}{2} + \frac{2\theta}{i} c_i \right) \left(\frac{c_{i+1} - c_{i-1}}{2} \right) \right], \tag{3.19}$$

where $i \in \{1, 2, \cdots, N-1\}$. At the right boundary point $i = N$ ($r = R_s$), the method of imaginary points is utilized to discretize the governing equations:

$$\begin{aligned}\frac{\partial c_N}{\partial t} &= \tau\left[(1+\theta c_N)\left(c_{N-1} - c_N - \frac{I \cdot N}{3\tau\varepsilon FAL(1+\theta c_N)}\right)\right] \\ &\quad + \tau\left[\frac{1}{N} + \frac{\theta}{4}\left(c_N - c_{N-1} - \frac{I \cdot N}{3\tau\varepsilon FAL(1+\theta c_N)}\right) + \frac{\theta}{N}c_N\right] \\ &\quad \times \left[c_N - c_{N-1} - \frac{I \cdot N}{3\tau\varepsilon FAL(1+\theta c_N)}\right]. \end{aligned} \tag{3.20}$$

The terms including $1/r$ has singularity at $r = 0$. Applying L'Hopital's rule eliminates the singularity, and (3.6) becomes

$$\frac{\partial c}{\partial t} = D\left[3(1+\theta c)\frac{\partial^2 c}{\partial r^2} + \theta\left(\frac{\partial c}{\partial r}\right)^2\right]. \tag{3.21}$$

Method of imaginary points can be employed again to discretize the governing equation at $i = 0$ ($r = 0$):

$$\frac{\partial c_0}{\partial t} = 6\tau(1+\theta c_0)(c_1 - c_0). \tag{3.22}$$

The state-space model can be written in the following form based on (3.19), (3.20), (3.22), and (3.17):

$$\begin{aligned}\dot{x} &= \tau\mathcal{A}x + \tau\theta f(x,\tau,u), \\ y &= h(c_N, u),\end{aligned} \tag{3.23}$$

where the state vector $x = \begin{bmatrix} c_0 & c_1 & c_2 & \dots & c_N \end{bmatrix}^\top \in \mathbb{R}^{N+1}$, input $u = I \in \mathbb{R}$ is the applied current, output terminal voltage $y = h(c_N, u) = V_T \in \mathbb{R}$, nonlinear function $f(x,\tau,u) = \begin{bmatrix} f_0(x) & f_1(x) & \dots & f_{N-1}(x) & f_N(x,\tau,u) \end{bmatrix}^\top \in \mathbb{R}^{N+1}$, and matrix $\mathcal{A} \in \mathbb{R}^{(N+1)\times(N+1)}$. Following the derivation from (3.19), (3.20), and (3.22), we have

$$\mathcal{A} = \begin{bmatrix} -6 & 6 & 0 & 0 & \cdots & \cdots & 0 \\ 0 & -2 & 2 & 0 & \cdots & \cdots & 0 \\ 0 & \frac{1}{2} & -2 & \frac{3}{2} & \cdots & \cdots & 0 \\ 0 & 0 & \frac{2}{3} & -2 & \cdots & \cdots & 0 \\ \vdots & \vdots & \vdots & \ddots & \ddots & \ddots & \vdots \\ 0 & 0 & 0 & 0 & \cdots & -2 & \frac{N}{N-1} \\ 0 & 0 & 0 & 0 & \cdots & \frac{N-1}{N} & -\frac{N-1}{N} \end{bmatrix}, \tag{3.24}$$

and

$$f(x,\tau,u)=\begin{bmatrix} 6c_0(c_1-c_0) \\ \vdots \\ c_i\left(\frac{i-1}{i}c_{i-1}-2c_i+\frac{i+1}{i}c_{i-1}\right)+\frac{(c_{i+1}-c_{i-1})^2}{4} \\ \vdots \\ f_N(c_{N-1},c_N,\tau,u) \end{bmatrix}, \tag{3.25}$$

where

$$\begin{aligned} f_N(c_{N-1},c_N,\tau,u) &= -\frac{N+1}{\theta N}\frac{I\cdot N}{3\tau\varepsilon FAL(1+\theta c_N)}+c_N\left[c_{N-1}-c_N-\frac{I\cdot N}{3\tau\varepsilon FAL(1+\theta c_N)}\right] \\ &+\left[\frac{1}{4}\left(c_N-c_{N-1}-\frac{I\cdot N}{3\tau\varepsilon FAL(1+\theta c_N)}\right)+\frac{1}{N}c_N\right]\left[c_N-c_{N-1}-\frac{I\cdot N}{3\tau\varepsilon FAL(1+\theta c_N)}\right]. \end{aligned} \tag{3.26}$$

Assumption 1. *It has been verified by numerous literature, e.g. [68], that the nonlinear output function $h(c_N,u)$ is strictly increasing with respect to the surface concentration c_N. We can conclude that for any given finite input u and any two different surface concentration values $c_{N,i}, c_{N,j} \in [\Theta^-_{\min},\Theta^-_{\max}]\cdot c^-_{s,\max}$, the following expression holds:*

$$\operatorname{sgn}\big(h(c_{N,i},u)-h(c_{N,j},u)\big)=\operatorname{sgn}\left(c_{N,i}-c_{N,j}\right), \tag{3.27}$$

where the operator sgn$(\cdot)$ is the signum function.

This property will become important, as it eases the analysis of observer convergence in the next section.

Remark 10. *The function $f(x,\tau,u)$ is continuously differentiable with respect to the state x and the parameter τ, a sufficient condition for Lipschitz continuity [68]. For any two vectors $X_1, X_2 \in \mathbb{R}^{N+1}$, where each entry of X_1 and X_2 is within the range $[\Theta^-_{\max},\Theta^-_{\min}]\cdot c^-_{s,\max}$, a Lipschitz constant with respect to the state x can be obtained by computing the infinity norm of $\partial f/\partial x$, i.e., $K_x=\|\partial f/\partial x\|_\infty$, such that*

$$\|f(X_1,\tau,u)-f(X_2,\tau,u)\|\le K_x\|X_1-X_2\|. \tag{3.28}$$

Similarly, for any two scalars T_1, $T_2\in\mathbb{R}$, a Lipschitz constant with respect to the parameter τ is expressed as $K_\tau=\|\partial f/\partial\tau\|_\infty$, such that

$$\|f(x,T_1,u)-f(x,T_2,u)\|\le K_\tau\|T_1-T_2\|. \tag{3.29}$$

From (3.28) and (3.29), a multi-variable Lipschitz continuous condition for the function $f(x,\tau,u)$ is inferred:

$$\|f(X_1,T_1,u)-f(X_2,T_2,u)\|\le K_x\|X_1-X_2\|+K_\tau\|T_1-T_2\|. \tag{3.30}$$

It also immediately follows from (3.28) that $f_N(c_N, c_{N-1}, \tau, u)$ *is bounded within the compact operating interval* $c_{N-1}, c_N \in [\Theta^-_{\min}, \Theta^-_{\max}] \cdot c^-_{s,\max}$*, for all finite input current* u *and finite parameter* τ*. Mathematically, for any* (c_{N-1}, c_N) *and* (c'_{N-1}, c'_N)*,*

$$|f_N(c_{N-1}, c_N, \tau, u) - f_N(c'_{N-1}, c'_N, \tau, u)| \leq M, \tag{3.31}$$

where $0 < M < \infty$*.*

Remark 11. *It should be pointed out that the considered set-up can be readily transferred to the case of concentration dependent parameters, eg.* $D = D(c)$ *and* $\theta = \theta(c)$*. Suppose the dependence is continuous, then the Lipschitz continuity property on nonlinear function* $f(x, \tau, u)$ *introduced in Remark 3 still holds since the discretized concentration* c_i *is bounded by* $[\Theta^-_{\min}, \Theta^-_{\max}] \cdot c^-_{s,\max}$*.*

Observability Analysis

The observbility of a nonlinear finite-dimensional system can be verified by a rank test based on the concept of *Lie Derivatives.* It should be pointed out that the local observability of a nonlinear system is not equivalent to the observability of the linearized system, which was examined previously in [69, 70] for battery equivalent circuit models. Here, we present local observability rank test by considering the following form of nonlinear system:

$$\dot{x} = \eta(x) + \sum_{i=1}^{m} u_i g_i(x), \tag{3.32}$$

$$y = \phi(x), \tag{3.33}$$

where $x \in \mathbb{R}^n$ is the state, $u_i \in \mathbb{R}$ is the input, $y \in \mathbb{R}$ is the output, and η, g_i, and ϕ are real-valued smooth functions. The gradient of ϕ, denoted by $\mathrm{d}\phi$, is expressed by

$$\mathrm{d}\phi = \begin{bmatrix} \frac{\partial \phi}{\partial x_1} & \frac{\partial \phi}{\partial x_2} & \cdots & \frac{\partial \phi}{\partial x_n} \end{bmatrix}. \tag{3.34}$$

The Lie Derivative of ϕ with respect to function η is denoted by

$$L_\eta \phi = \mathrm{d}\phi \cdot \eta = \sum_{i=1}^{n} \frac{\partial \phi}{\partial x_i} \cdot \eta_i. \tag{3.35}$$

The following theorem [71] provides the rank test for local observability of a nonlinear system in the form of (3.32)-(3.33).

Theorem 3. *Suppose* $x_0 \in \mathbb{R}^n$ *is given. Consider the expression*

$$\Gamma = (\mathrm{d}L_{z_s} L_{z_{s-1}} \cdots L_{z_1} \phi)(x_0), \tag{3.36}$$

where $s \geq 0, z_i \in \{\eta, g_1, \cdots, g_m\}$*, evaluated at* x_0*. If there are* n *linearly independent row vectors in* Γ*, then the system is locally observable around* x_0*.*

Herein, for the simplicity of the calculation, we evaluate the local observability under constant input current. The expressions of $\eta(x)$, $g_1(x)$, $g_2(x)$, and $\phi(x)$ can be derived from the state-space model (3.23)-(3.26), and $u_1 = I$ and $u_2 = I^2$. The calculation of Γ in (3.36) reveals that the system is locally observable at x_0.

3.5 Observer Design and Analysis

The state and parameter estimation problem seeks to design an adaptive observer system to reconstruct the unknown state x and parameter τ in the plant model (3.23) with the knowledge of output y and input u measurements. In this present work, the available energy of the battery cell is quantified by the bulk SOC in the anode, and it can be computed from normalizing the anode volume average of Li-ion concentration against the maximum concentration:

$$SOC(t) = \frac{3}{(R_s^-)^3 c_{s,\max}^-} \int_0^{R_s^-} r^2 c_s^-(r,t) dr. \tag{3.37}$$

Note that the SOC calculation in (3.37) yields an un-normalized value. The actual bulk SOC should be normalized with respect to the difference of upper and lower stoichiometry points of anode material. The estimation of radial and tangential stresses are computed using solid phase Li-ion concentration estimation by (3.3)-(3.4).

Remark 12. *The magnitude of diffusion induced electrode stress is not a comprehensive indicator of battery health, but certainly is a contributor to several physical degradation phenomena associated with battery health. Examples include the growth of particle surface cracks as a function of maximum tangential stress according to Paris' Law [72], and mechanical fatigue described by the Palmgren-Milner (PM) rule [73].*

The primary unknown parameter considered in this chapter is the diffusivity in the anode D_s^-, or equivalently τ, as it directly affects the dynamics of Li-ion transportation in the solid phase. There is also consensus within the literature that the diffusion coefficient is one of the most sensitive parameters to the battery cycling aging [74]. Aside from improving the state estimation accuracy, the estimated parameter can be regarded as an indicator of SOH. Thus, the battery health condition is assessed by both model parameter values and physical degradation phenomena associated with the diffusion induced stress.

Systematic ways for adaptive observer design for nonlinear systems have been studied in the existing literature [75, 76]. These approaches often consider certain dynamic model structures with linear model output function, where the linearity in the output is an essential property for deriving the update law for parameter estimate. Nonetheless, the output map in the battery application is highly nonlinear with respect to the states and input, which makes the adaptive observer design intricate. In this chapter, we adopt a similar approach as in [75], with the extension to (i) a nonlinear output equation and (ii) a more general model

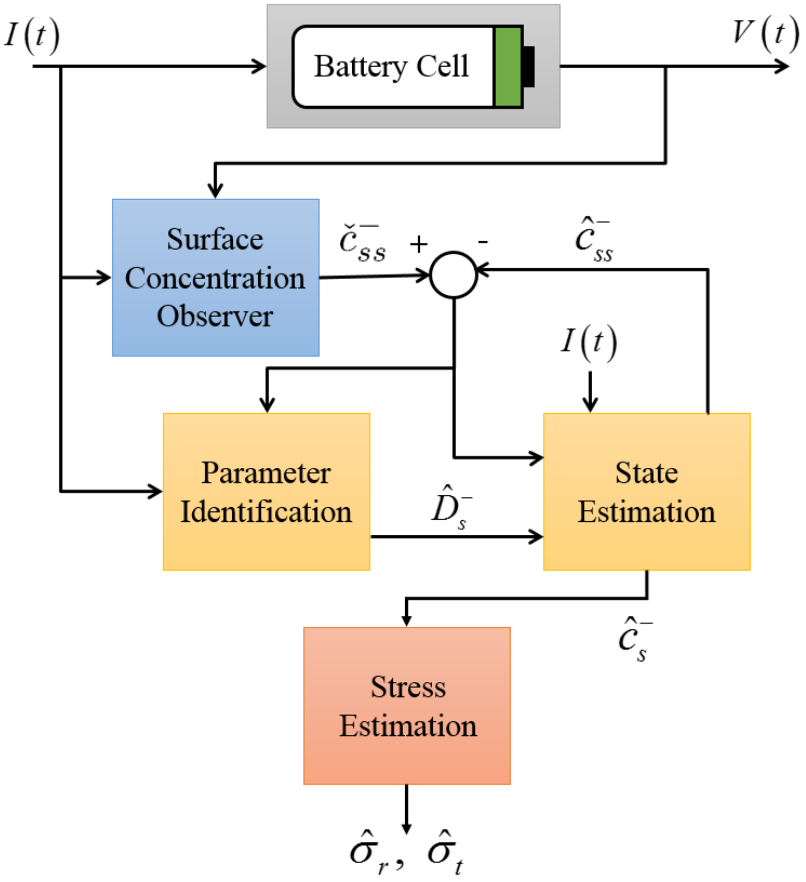

Figure 3.3: Block diagram of adaptive observer structure. It consists of the solid phase surface concentration observer (blue), the adaptive observer (yellow), and the stress estimation calculation (coral). The adaptive observer is comprised of two parts: diffusion coefficient identification (yellow/left) and and full state observer (yellow/right). The observers utilize measurements of input current and output terminal voltage only.

dynamics structure. The stability of the the proposed observer will be rigorously analyzed by the Lyapunov's direct method.

Figure 3.3 depicts the observer design concept. The surface concentration observer (blue block) takes the measurements of input current and output voltage to estimate the surface concentration only. The estimated surface concentration becomes a pseudo-measurement signal utilized in the subsequent adaptive observer (yellow blocks). The model used for adaptive observer design is reformulated such that the surface concentration estimation becomes the model output, which is a linear function of the state vector. Finally the stress estimation (coral block) can be calculated from the state estimates. The details are illustrated in the following sections.

Surface Concentration Observer Design

In this section, we present the observer design for estimating solid phase surface concentration (blue block in Figure 3.3), and the corresponding convergence analysis using the Lyapunov's direct method.

In order to obtain surface concentration information and reformulate the state space model for adaptive observer design, we separate the state vector x into two components, namely define $\xi = \begin{bmatrix} c_0 & c_1 & \cdots & c_{N-1} \end{bmatrix}^\top$ that contains the first N entries of x, and $x = \begin{bmatrix} \xi^\top & c_N \end{bmatrix}^\top$. Re-write the plant model (3.23) as

$$\dot{\xi} = \tau \overline{\mathcal{A}} x + \tau F(x), \tag{3.38}$$

$$\dot{c}_N = \tau \frac{N-1}{N} c_{N-1} - \tau \frac{N-1}{N} c_N + \tau \theta f_N(x, u), \tag{3.39}$$

$$y = h(c_N, u), \tag{3.40}$$

where $\overline{\mathcal{A}}$ is the matrix $\mathcal{A}$ excluding the last row, and $F(x) = \begin{bmatrix} f_0(\xi) & f_1(\xi) & \cdots & f_{N-1}(x) \end{bmatrix}^\top$. Note that in the plant model (3.38)-(3.40), the unknown parameter is τ and the unknown states are ξ and c_N. Despite the fact that τ is unknown, proper upper and lower bounds of τ is assumed. These bounds can be retrieved from existing literature based on the electrode materials. Mathematically, we have

$$0 < \underline{\tau} \leq \tau \leq \overline{\tau} < \infty. \tag{3.41}$$

Consider the following observer structure:

$$\dot{\check{c}}_N = \tau^o \frac{N-1}{N} \check{c}_{N-1} - \tau^o \frac{N-1}{N} \check{c}_N + \tau^o \theta \check{f}_N + L \cdot \operatorname{sgn}\left(y - \check{y}\right), \tag{3.42}$$

where the quantities with the "inverse hat" symbols denote their estimation, and the scalar observer gain $L > 0$ is to be designed such that the estimation converges to the actual value. Moreover, $\check{f}_N = f_N(\check{c}_{N-1}, \check{c}_N, \tau^o, u)$. The parameter τ^o is a nominal value chosen *a priori* such that $\underline{\tau} \leq \tau_o \leq \overline{\tau}$, and we further assume that $\tau = \tau^o + \delta\tau$. Our objective is to estimate the surface concentration with the presence of parameter uncertainty, which can be achieved by selecting a sufficiently high observer gain L. The above sliding mode observer structure adopts the error injection concept and is well-known for its robustness against parameter/model uncertainty when applied to nonlinear systems [77].

Proposition 1. *Consider the surface concentration dynamics (3.39) with bounded unknown parameter $\underline{\tau} \leq \tau \leq \overline{\tau}$, and observer (3.42). If there exists a scalar gain such that*

$$L > \overline{\tau} \frac{N-1}{N} |\tilde{c}_{N-1}|_{\max} + \overline{\tau} \theta M + \overline{\Psi}, \tag{3.43}$$

in which $\overline{\Psi} > 0$ is finite and given by (3.45), then the estimation error $\tilde{c}_N = c_N - \check{c}_N$ converges to zero in finite time.

Proof. Consider the estimation errors $\tilde{c}_N = c_N - \check{c}_N$ and $\tilde{c}_{N-1} = c_{N-1} - \check{c}_{N-1}$. Subtracting (3.42) from (3.39), and the error dynamics can be written as:

$$\begin{aligned}\dot{\tilde{c}}_N = {} & \tau^o \frac{N-1}{N}\tilde{c}_{N-1} - \tau^o \frac{N-1}{N}\tilde{c}_N + \tau^o \theta \tilde{f}_N - L\mathrm{sgn}(\tilde{c}_N) \\ & + \delta\tau \frac{N-1}{N} c_{N-1} - \delta\tau \frac{N-1}{N} c_N + \delta\tau\theta f_N,\end{aligned} \tag{3.44}$$

where $\tilde{f}_N = f_N(c_{N-1}, c_N, \tau, u) - f_N(\check{c}_{N-1}, \check{c}_N, \tau^o, u)$. Notice that we have utilized the monotonicity property of y (see Assumption 1) to substitute $\mathrm{sgn}(y - \check{y})$ with $\mathrm{sgn}(\tilde{c}_N)$. Based on the fact that c_N, c_{N-1} and f_N are bounded under finite input current, let

$$\Psi \triangleq \delta\tau \frac{N-1}{N} c_{N-1} - \delta\tau \frac{N-1}{N} c_N + \delta\tau\theta f_N \leq \overline{\Psi}, \tag{3.45}$$

with $\overline{\Psi} > 0$ being the upper bound of Ψ.

We analyze the error dynamics (3.44) using the Lyapunov function candidate

$$V = \frac{1}{2}\tilde{c}_N^2, \tag{3.46}$$

and the derivative of the Lyapunov function along the trajectory of $\tilde{c}_N$ is

$$\begin{aligned}\dot{V} &= \tilde{c}_N \dot{\tilde{c}}_N \\ &= \tilde{c}_N \left[\tau^o \frac{N-1}{N}\tilde{c}_{N-1} - \tau^o \frac{N-1}{N}\tilde{c}_N + \tau^o\theta\tilde{f}_N - L\mathrm{sgn}(\tilde{c}_N) + \Psi\right] \\ &\leq |\tilde{c}_N| \left[\overline{\tau}\frac{N-1}{N}|\tilde{c}_{N-1}| + \overline{\tau}\theta|\tilde{f}_N| + \overline{\Psi}\right] - L\tilde{c}_N\mathrm{sgn}(\tilde{c}_N) - \tau^o\frac{N-1}{N}\tilde{c}_N^2 \\ &\leq |\tilde{c}_N| \left[\overline{\tau}\frac{N-1}{N}|\tilde{c}_{N-1}| + \overline{\tau}\theta|\tilde{f}_N| + \overline{\Psi}\right] - L|\tilde{c}_N| \\ &\leq |\tilde{c}_N| \left[\overline{\tau}\frac{N-1}{N}|\tilde{c}_{N-1}| + \overline{\tau}\theta M + \overline{\Psi} - L\right].\end{aligned} \tag{3.47}$$

If the gain L is chosen high enough such that

$$L > \overline{\tau}\frac{N-1}{N}|\tilde{c}_{N-1}|_{\max} + \overline{\tau}\theta M + \overline{\Psi}, \tag{3.48}$$

then we have that $\dot{V}_1 \leq 0$.

Choose L^* that meets the condition in (3.48), and define

$$\rho = L^* - \left[\overline{\tau}\frac{N-1}{N}|\tilde{c}_{N-1}|_{\max} + \overline{\tau}\theta M + \overline{\Psi}\right] > 0. \tag{3.49}$$

From (3.47) and (3.49), we have that

$$\dot{V} \leq -\sqrt{2}\rho\sqrt{V}. \tag{3.50}$$

The time required for $\tilde{c}_N$ to converge to zero can be analytically computed by solving (3.50) for V using the comparison principle [32], and setting $V = 0$ and solving for t_f:

$$t_f = \frac{\sqrt{2V(0)}}{\rho}, \tag{3.51}$$

where $V(0)$ is the initial condition of V. Therefore after $t \geq t_f$, $\tilde{c}_N \to 0$. Finite time convergence of $\check{c}_N \to c_N$ is attained. ■

Adaptive Observer Design

In this Chapter, we develop the adaptive observer by extending the results from [75]. The surface concentration estimation $\check{c}_N$ from the surface concentration observer is leveraged as a pseudo-measurement signal for a reformulated plant model. The dynamical equations in (3.23) are preserved while the output is reformulated as a linear function of the state vector:

$$\begin{aligned} \dot{x} &= \tau \mathcal{A} x + \tau \theta f(x, \tau, u), \\ y_s &= C x, \end{aligned} \tag{3.52}$$

where $y_s = c_N$ and $C = \begin{bmatrix} 0 & 0 & \cdots & 0 & 1 \end{bmatrix} \in \mathbb{R}^{1\times(N+1)}$. The adaptive observer is designed such that the unknown state x and parameter τ are converging to their actual values simultaneously. The estimation system consists of a copy of the plant model (3.52) plus the output error injection, as follows:

$$\begin{aligned} \dot{\hat{x}} &= \hat{\tau} \mathcal{A} \hat{x} + \hat{\tau} \theta f(\hat{x}, \hat{\tau}, u) + L_a(y_s - \hat{y}_s), \\ \hat{y}_s &= C \hat{x}, \end{aligned} \tag{3.53}$$

where the quantities with the “hat" symbols denote their estimation, and $L_a \in \mathbb{R}_+^{N+1}$ is a vector of positive scalar gains to be designed. We seek to derive an update law for $\hat{\tau}$ and conditions on L_a that guarantee the convergence of state and parameter estimates. Theorem 1 summarizes the convergence results for adaptive observer (3.53).

Theorem 4. *Consider the plant model (3.52) and observer system (3.53), given accurate estimation of surface concentration from Proposition 1. Let the error between the actual and the estimated quantities to be $\tilde{x} = x - \hat{x}$, $\tilde{\tau} = \tau - \hat{\tau}$, and $\tilde{y}_s = y_s - \hat{y}_s$. Furthermore, assume the actual value of the unknown parameter is bounded by $\underline{\tau} \leq \tau < \overline{\tau}$. Then the estimation error $\tilde{x}$ and $\tilde{\tau}$ converge to zero asymptotically, if the observer gain vector L_a is designed such that for all $\tau^\dagger \in [\underline{\tau}, \overline{\tau}]$, there exists a positive semidefinite matrix Q that verifies*

$$\tau^\dagger \mathcal{A} + \overline{\tau} \theta K_x I_N - L_a C \preceq -Q, \tag{3.54}$$

and $\hat{\tau}$ evolves according to the system

$$\dot{\hat{\tau}} = \frac{\tilde{y}_s C \mathcal{A} \hat{x} + \tilde{y}_s \theta f_N(\hat{x}, \hat{\tau}, u)}{\gamma}, \tag{3.55}$$

where I_N denotes a $(N+1) \times (N+1)$ identity matrix, and $\gamma > 0$.

Proof. The state error dynamics are expressed by subtracting (3.53) from (3.52):

$$\begin{aligned}\dot{\tilde{x}} &= \tau\mathcal{A}x - \hat{\tau}\mathcal{A}\hat{x} + \tau\theta f(x,\tau,u) - \hat{\tau}\theta f(\hat{x},\hat{\tau},u) - L_a\tilde{y}_s,\\ \tilde{y}_s &= C\tilde{x}.\end{aligned} \tag{3.56}$$

The Lyapunov function candidate is chosen as

$$V_a = \frac{1}{2}\tilde{x}^\top\tilde{x} + \frac{1}{2}\gamma\tilde{\tau}^2, \quad \text{where } \gamma > 0. \tag{3.57}$$

The derivative of V_a along the trajectory of $\tilde{x}$ is

$$\begin{aligned}\dot{V}_a &= \frac{1}{2}\dot{\tilde{x}}^\top\tilde{x} + \frac{1}{2}\tilde{x}^\top\dot{\tilde{x}} + \gamma\tilde{\tau}\dot{\tilde{\tau}}\\ &= \tilde{x}^\top\dot{\tilde{x}} + \gamma\tilde{\tau}\dot{\tilde{\tau}}\\ &= \tilde{x}^\top[\tau\mathcal{A}x - \hat{\tau}\mathcal{A}\hat{x} + \tau\theta f(x,\tau,u) - \hat{\tau}\theta f(\hat{x},\hat{\tau},u) - L_a\tilde{y}_s] + \gamma\tilde{\tau}\dot{\tilde{\tau}}\\ &= \tilde{x}^\top[\tau\mathcal{A}x - (\tau-\tilde{\tau})\mathcal{A}\hat{x} + \tau\theta f(x,\tau,u) - (\tau-\tilde{\tau})\theta f(\hat{x},\hat{\tau},u) - L_aC\tilde{x}] + \gamma\tilde{\tau}\dot{\tilde{\tau}}\\ &= \tilde{x}^\top[\tau\mathcal{A}\tilde{x} + \tilde{\tau}\mathcal{A}\hat{x} + \tau\theta(f(x,\tau,u) - f(\hat{x},\hat{\tau},u)) + \tilde{\tau}\theta f(\hat{x},\hat{\tau},u) - L_aC\tilde{x}] + \gamma\tilde{\tau}\dot{\tilde{\tau}}\\ &\leq \tilde{\tau}[\tilde{x}^\top\mathcal{A}\hat{x} + \tilde{x}^\top\theta f(\hat{x},\hat{\tau},u) - \gamma\dot{\hat{\tau}}] + \tilde{x}^\top(\tau\mathcal{A} - L_aC)\tilde{x} + \tau\theta\|\tilde{x}\|\|f(x,\tau,u) - f(\hat{x},\hat{\tau},u)\|\\ &\leq \tilde{\tau}[\tilde{x}^\top\mathcal{A}\hat{x} + \tilde{x}^\top\theta f(\hat{x},\hat{\tau},u) - \gamma\dot{\hat{\tau}}] + \tilde{x}^\top(\tau\mathcal{A} - L_aC)\tilde{x} + \overline{\tau}\theta\|\tilde{x}\|(K_x\|\tilde{x}\| + K_\tau\|\tilde{\tau}\|)\\ &= \tilde{\tau}[\tilde{x}^\top\mathcal{A}\hat{x} + \tilde{x}^\top\theta f(\hat{x},\hat{\tau},u) - \gamma\dot{\hat{\tau}}] + \tilde{x}^\top(\tau\mathcal{A} + \overline{\tau}\theta K_xI_N - L_aC)\tilde{x} + \overline{\tau}\theta K_\tau\|\tilde{x}\|\|\tilde{\tau}\|,\end{aligned} \tag{3.58}$$

where we have applied the Lipschitz continuity of the function f with respect to x and τ at the second inequality according to Remark 3, and the last equality follows from $\|\tilde{x}\|\|\tilde{x}\| = \tilde{x}^\top\tilde{x}$.

Now choose the update law for $\hat{\tau}$ by eliminating the terms associated with $\tilde{\tau}$ in the last line of (3.58):

$$\tilde{x}^\top\mathcal{A}\hat{x} + \tilde{x}^\top\theta f(\hat{x},\hat{\tau},u) - \gamma\dot{\hat{\tau}} = 0. \tag{3.59}$$

Since $\tilde{x}$ is unavailable because the actual states are unknown, we multiply both sides of (3.59) by $CC^\top = 1$ to get

$$\tilde{y}_sC\mathcal{A}\hat{x} + \tilde{y}_sC\theta f(\hat{x},\hat{\tau},u) - \gamma\dot{\hat{\tau}} = 0. \tag{3.60}$$

Then the update law for $\hat{\tau}$ can be explicitly written as

$$\dot{\hat{\tau}} = \frac{\tilde{y}_sC\mathcal{A}\hat{x} + \tilde{y}_s\theta f_N(\hat{x},\hat{\tau},u)}{\gamma}, \tag{3.61}$$

and the inequality (3.58) is simplified to

$$\dot{V}_a \leq \tilde{x}^\top(\tau\mathcal{A} + \overline{\tau}\theta K_xI_N - L_aC)\tilde{x} + \overline{\tau}\theta K_\tau\|\tilde{x}\|\|\tilde{\tau}\|. \tag{3.62}$$

Choose gain L_a such that for all $\tau^\dagger \in [\underline{\tau}, \overline{\tau}]$, there exists a positive semidefinite matrix Q that satisfies

$$\tau^\dagger\mathcal{A} + \overline{\tau}\theta K_xI_N - L_aC \preceq -Q, \tag{3.63}$$

and therefore,

$$\begin{aligned}\dot{V}_a &\leq -\tilde{x}^\top Q\tilde{x} + \overline{\tau}\theta K_\tau\|\tilde{x}\|\|\tilde{\tau}\| \\ &\leq -\lambda_{\min}(Q)\|\tilde{x}\|^2 + \overline{\tau}\theta K_\tau\|\tilde{x}\|\|\tilde{\tau}\| \\ &= -\begin{bmatrix}\|\tilde{x}\| & \|\tilde{\tau}\|\end{bmatrix}\begin{bmatrix}\lambda_{\min}(Q) & -\overline{\tau}\theta K_\tau \\ 0 & 0\end{bmatrix}\begin{bmatrix}\|\tilde{x}\| \\ \|\tilde{\tau}\|\end{bmatrix} \\ &\triangleq -\tilde{v}P\tilde{v}^\top,\end{aligned} \tag{3.64}$$

where $\tilde{v} = \begin{bmatrix}\|\tilde{x}\| & \|\tilde{\tau}\|\end{bmatrix}$. Apparently the matrix P is positive semidefinite since the eigenvalues of P are $\{\lambda_{\min}(Q), 0\}$, where $\lambda_{\min}(Q) \geq 0$. Hence, it follows that $\dot{V}_a \leq 0$. Next we analyze the convergence of state and parameter estimation errors.

Convergence of state estimation

Integrating both sides of (3.64) and we have that

$$V_a(t) \leq V_a(0) - \int_0^t \tilde{v}^\top P\tilde{v}dt, \tag{3.65}$$

which implies $0 \leq V_a(t) \leq V_a(0)$, so $V_a \in L_\infty$. From (3.57), $\tilde{x} \in L_\infty$ and $\tilde{\tau} \in L_\infty$. Moreover, $\hat{x} = x - \tilde{x} \in L_\infty$ and $\hat{\tau} = \tau - \tilde{\tau} \in L_\infty$. Since $V_a(0)$ is finite and $V_a(t) \in L_\infty$, $\tilde{x} \in L_2$. In addition, from (3.56) and the fact that f is bounded, we have $\dot{\tilde{x}} \in L_\infty$. According to Barbalat's Lemma [78], $\tilde{x}, \dot{\tilde{x}} \in L_\infty$ and $\tilde{x} \in L_2$ allows us to conclude that

$$\lim_{t\to\infty} \tilde{x} = 0. \tag{3.66}$$

Therefore, $\hat{x}$ converges to x asymptotically.

Convergence of parameter estimation

It has been shown in the previous suctions that $\tilde{x}$ is differentiable and has a finite limit as $t \to \infty$. Since f is Lipschitz continuous, f is immediately uniformly continuous. Let $\chi = \tau\mathcal{A}x - \hat{\tau}\mathcal{A}\hat{x} - L_a\tilde{y}_s = \tau\mathcal{A}\tilde{x} + \tilde{\tau}\mathcal{A}\hat{x} - L_aC\tilde{x}$, which are the terms at the right hand side of (3.56) that are not associated with function f, and we would like to show χ is uniformly continuous by verifying the boundedness of $\dot{\chi}$. Taking the derivative of χ with respect to time:

$$\dot{\chi} = \tau\mathcal{A}\dot{\tilde{x}} + \dot{\tilde{\tau}}\mathcal{A}\hat{x} + \tilde{\tau}\mathcal{A}\dot{\hat{x}} - L_aC\dot{\tilde{x}}. \tag{3.67}$$

Since $\hat{x} \in L_\infty$ and f is bounded, we have $\dot{\hat{x}} \in L_\infty$ from (3.53). Based on (3.61), $\dot{\tilde{\tau}} = -\dot{\hat{\tau}}$ is bounded because $\hat{x}$ and f are bounded. Then it can be concluded that $\dot{\chi}$ is bounded, which reveals that χ is uniformly continuous. Therefore, $\dot{\tilde{x}}$ is uniformly continuous. Again, apply Barbalat's Lemma [78],

$$\lim_{t\to\infty} \dot{\tilde{x}} = 0. \tag{3.68}$$

Table 3.2: Summary of Observer Design

System	**Variables**	**Design Params.**	**Convergence Type**
Surface Concentration Observer	$\check{c}_{ss}$	L in (3.42)	Finite-Time
Solid Phase Concentration	$\hat{x}$	L_a in (3.53)	Asymptotic
Parameter - Diffusivity	$\hat{\tau}$	γ in (3.61)	Asymptotic

Consider the first N state error dynamical equations in (3.56), and it implies that when $t \to \infty$,

$$\tau\overline{\mathcal{A}}x - \hat{\tau}\overline{\mathcal{A}}\hat{x} + \tau\theta F(x) - \hat{\tau}\theta F(\hat{x}) \to 0. \tag{3.69}$$

Theoretically if the states converge asymptotically, i.e. $\hat{x} \to x$ as $t \to \infty$, then from (3.69) we have

$$\left[\overline{\mathcal{A}}x + \theta F(x)\right](\tau - \hat{\tau}) \to 0 \quad \text{as } t \to \infty, \tag{3.70}$$

so $\hat{\tau}$ converges to τ asymptotically. ■

The value which $\hat{\tau}$ converges to highly relies on whether $\hat{x}$ provides an accurate estimation. In other words, the state estimation error determines how accurate the parameter estimation will be. The uncertainties in the adaptive observer may result from uncertainties in current and voltage measurements, and model mismatch. Additionally, the performance of the adaptive observer is highly sensitive to the accuracy of the surface concentration observer since its output becomes the input of the adaptive observer. Any uncertainties in the surface concentration observer are passed into the adaptive observer stage.

Summary of Observer Design

The design of the complete observer is summarized in Table 3.2. It lists equations for each subsystem, the corresponding design parameters, as well as the convergence type based on the analysis in previous sections.

3.6 Results and Discussion

In this Chapter, we present results from simulation and experimental data to demonstrate the performance of the proposed nonlinear observers.

Table 3.3: SPM-Stress Model Parameters

Symbols	Simulation	Experimental	Units
L^-	100×10^{-6}	123×10^{-6}	m
L^+	100×10^{-6}	119×10^{-6}	m
D_s^-	3.9×10^{-14}	7.98×10^{-16}	m^2/s
R_s^-	10×10^{-6}	8.21×10^{-6}	m
ε_s^-	0.6	0.7215	N/A
ε_s^+	0.5	0.6516	N/A
k^-	1×10^{-5}	2.19×10^{-6}	$\mathrm{A{\cdot}m}^{2.5}/\mathrm{mol}^{1.5}$
k^+	3×10^{-7}	2.68×10^{-7}	$\mathrm{A{\cdot}m}^{2.5}/\mathrm{mol}^{1.5}$
R_f	1.0×10^{-3}	1.0×10^{-3}	$\Omega \times \mathrm{m}^2$
$n_{Li,s}$	2.5	0.14	mol
$c_{s,\max}^-$	24983	31168	$\mathrm{mol/m}^3$
$c_{s,\max}^+$	46171	42649	$\mathrm{mol/m}^3$
A	1	0.049	m^2
E_n	60	60	GPa
ν_n	0.25	0.25	N/A
Ω_n	4.926×10^{-6}	4.926×10^{-6}	$\mathrm{m}^3/\mathrm{mol}$

Simulation Study

The parameters used in the simulation are adopted from the DUALFOIL simulation package that is publicly available [79]. The model parameters for anode, including diffusion and mechanical properties, are enumerated in Table 3.3. The mechanical parameters of anode material are obtained from [55]. We illustrate the observer performance by initializing the state and parameter estimates at incorrect values.

We apply a constant 1C discharge cycle for around 45 minutes. Figure 3.4(a) and 3.4(b) portrays the evolution of input current and the surface concentration estimate from the surface concentration observer. The surface concentration estimation is initialized with a 12.8% error to validate the convergence property. Notice that with a proper selection of the gain as presented in (3.48), the convergence time for $\check{c}_{ss}^-$ is 15 seconds. Next, the surface concentration estimate is fed into the adaptive observer as a pseudo-measurement signal for combined state and parameter estimation. The estimation for surface concentration, terminal voltage, bulk SOC, and anode diffusivity are plotted against their simulated values from the plant model (3.23) in Figure 3.4(c)-(f). Figure 3.4(g)-(h) provide the plots of the estimation for maximum absolute radial and tangential stresses over time, which are located at the center and the surface of the anode electrode particle, respectively. With an appropriate choice of gain as presented in Chapter 3.5, the estimates effectively converge to their simulated values from plant model. It is worth mentioning that the internal stress estimates can be monitored in real time to prevent it from getting higher than the yielding stress of the electrode material,

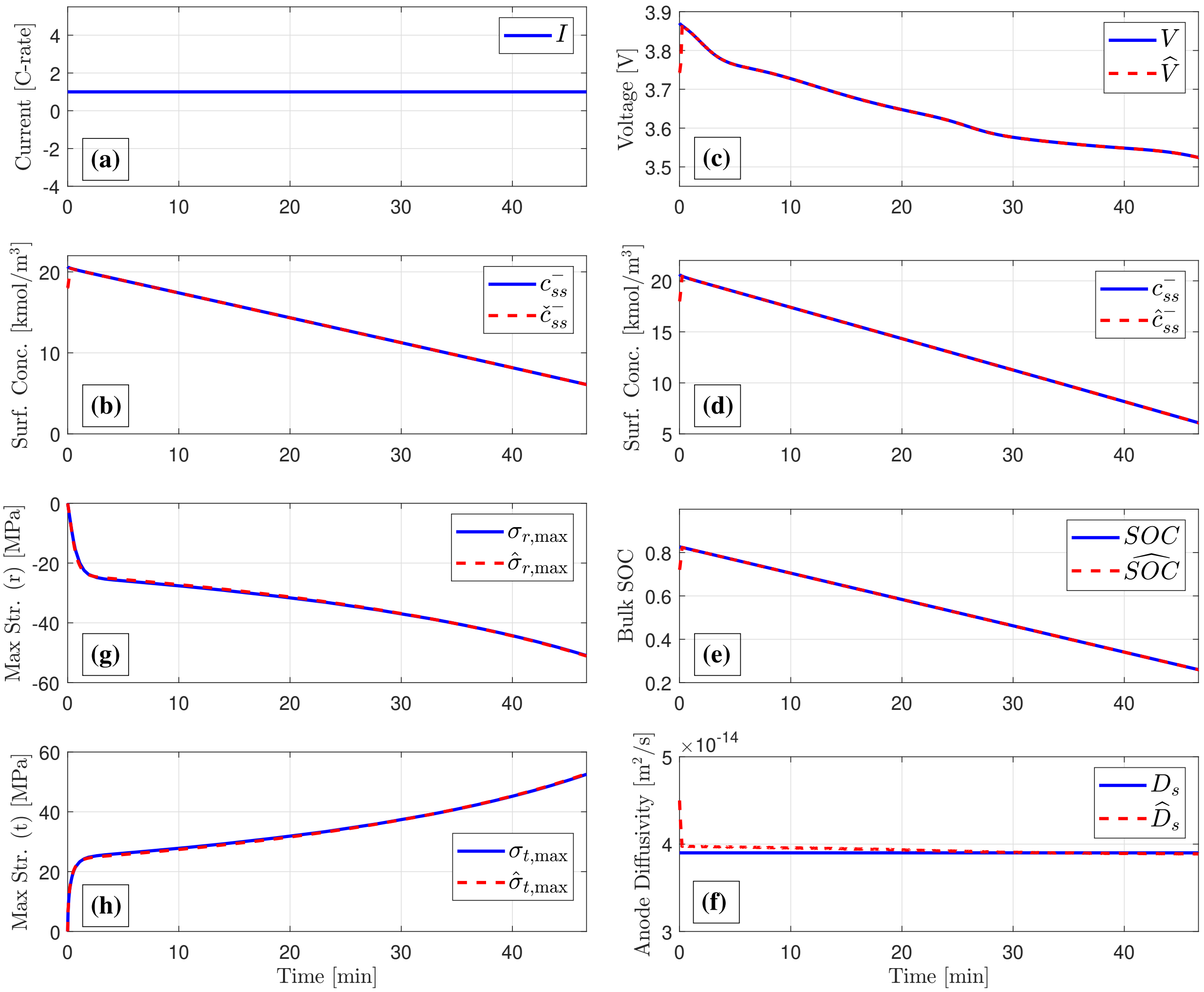

Figure 3.4: Estimation performance under an 1C discharge current in simulation. (a) input current; (b) surface concentration; (c) voltage; (d) surface concentration from adaptive observer; (e) bulk SOC; (f) anode diffusivity; (g) max radial stress; (h) max tangential stress.

and utilized to analyze the stress-related physical degradation.

Experimental Studies

In this Chapter, the performance of the designed adaptive observer is demonstrated via experimental data from a commercial $LiNiMnCoO_2$ (NMC) – LiC_6 cell. The ambient temperature of the battery cell under test is retained at 25.5 °C inside an ESPEC BTL-433 environmental chamber, and an Arbin High Current Cylindrical Cell Holder is used to hold

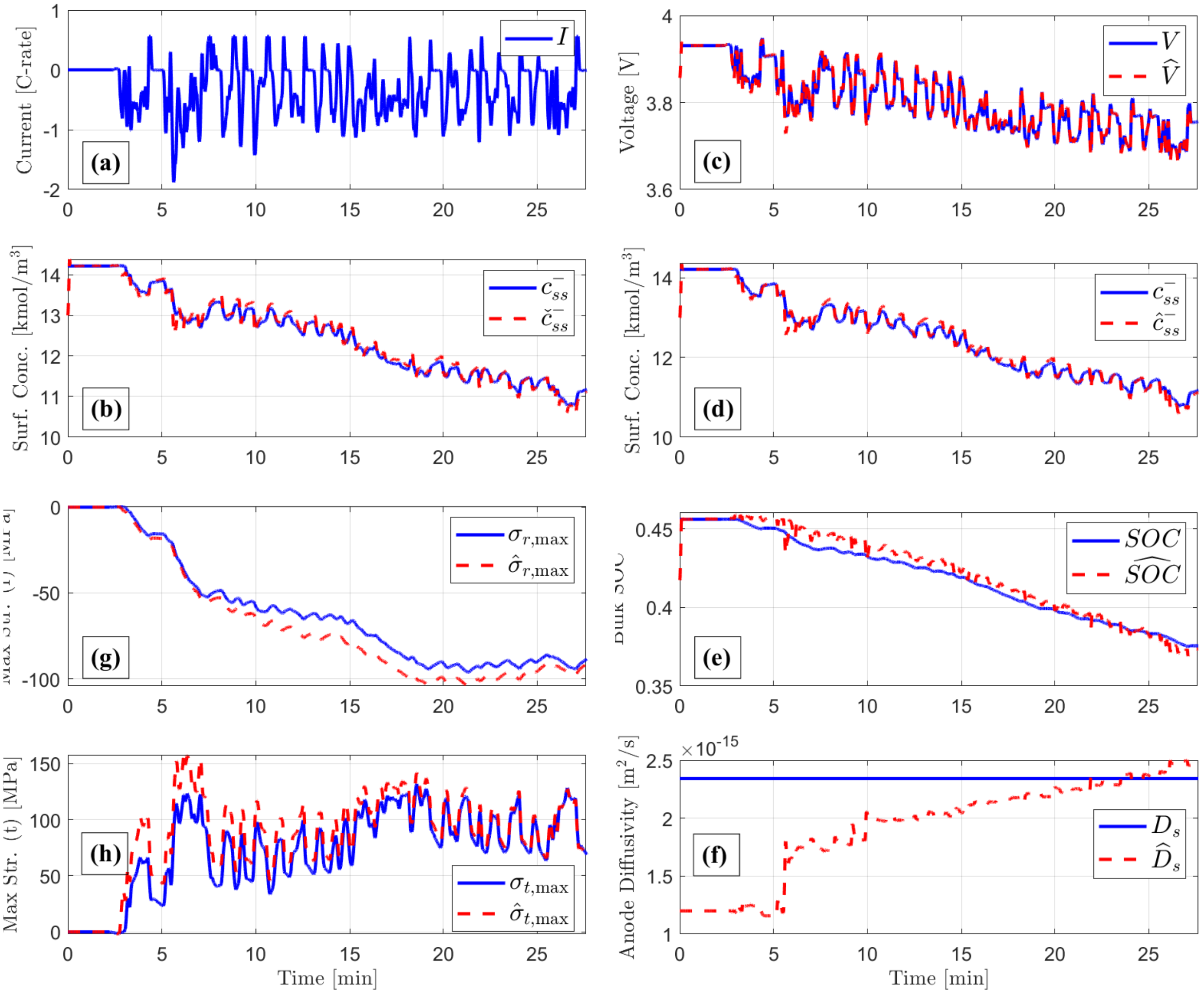

Figure 3.5: Estimation performance from experimental data under an UDDS drive cycle. (a) input current; (b) surface concentration; (c) voltage; (d) surface concentration from adaptive observer; (e) bulk SOC; (f) anode diffusivity; (g) max radial stress; (h) max tangential stress.

the battery cell. A PEC SBT2050 cycler applies a vehicle charge-discharge cycle. The experimentally collected data, current and voltage, have been used for identification of SPM-Stress model parameters. For the model identification, we utilized Particle Swarm Optimization (PSO) to minimize the root mean squared voltage error between experimental data and model output to get the best model fit [80]. Besides the parameters associated with battery geometry, mechanical properties, and equilibrium structure, the model parameters that are fitted by PSO are D_s^-, R_s^-, k^-, and k^+. The mechanical parameters are adopted from [55] for graphite. A summary of the parameter values are listed in Table 3.3. The state and parameter estimation are initialized with random (incorrect) guess to evaluate the convergence of the observers. Unlike the cases in the simulation study, we no longer know the true solid phase Li-ion concentration and SOC. As a consequence, the criteria for assessing the observer performance is through the comparison of measured voltage and voltage estimates computed from Li-ion concentration estimation.

The "actual" quantities plotted in the figures are obtained through the following ways:

- The "actual" diffusion coefficient is obtained by fitting the voltage output from the plant model in (3.23) to the experimental voltage measurement offline by PSO.
- The "actual" surface concentration, maximum radial stress, and maximum tangential stress are simulated utilizing the plant model (3.23) with the identified parameters from the last step.
- The "actual" bulk SOC is computed by the coulomb counting technique, by integrating the applied current normalized with battery capacity.

During the experiment, the battery cell was first charged to 100% SOC using a standard constant-current-constant-voltage (CCCV) protocol, followed by a discharge period until the SOC drops down to 80% SOC. An electric vehicle-like charge-discharge cycle is then applied to the battery cell, plotted in Figure 3.5(a). The results for the surface concentration observer and adaptive observer are given in Figure 3.5(b) and 3.5(c)-(f), respectively. The root mean squared percentage error (RMSPE) is selected to quantified the estimation accuracy:

$$\text{RMSPE}(z, \hat{z}) = \sqrt{\frac{1}{n}\sum_{i=1}^{n}\left(\frac{\hat{z}_i - z_i}{z_i} \times 100\%\right)^2}, \tag{3.71}$$

where z and $\hat{z}$ denote the true and estimated quantities and n is the number of data points. After the initial transition period, the RMSPE between the voltage estimation and experimentally measured voltage is 0.143%. Similarly, the RMSPE for SOC and anode diffusivity estimation against their true values are 1.24% and 5.53%, respectively. As expected, the estimated variables converge to their actual values starting with an incorrect initialization. Notice that the estimated variables from the adaptive observer exhibit large uncertainties at the beginning, mainly because the adaptive observer requires correct surface concentration estimation from the previous stage.

This chapter presents and rigorously analyzes simultaneous state and parameter estimation utilizing the nonlinear coupled SPM and stress model. Similar to most other existing techniques [74, 60], the method proposed here is capable of estimating aging related parameters in the battery model, e.g. diffusivity. Moreover, estimation of stresses generated inside the electrode particles provide another crucial measure for evaluating stress-related battery degradation phenomena.

Remark 13. *This work addresses observer design for nonlinear PDEs by projecting the PDEs onto a finite-dimension subspace, and applying nonlinear observer design for ODEs.*

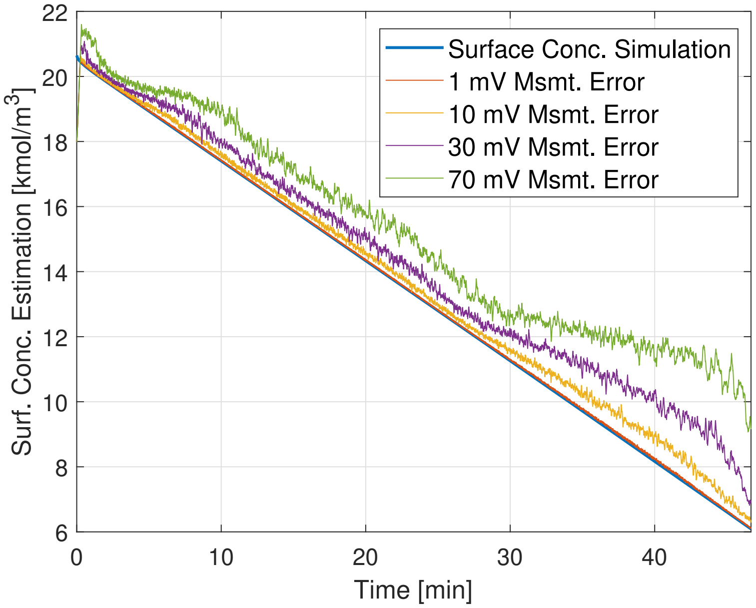

Figure 3.6: The effect of measurement noise on the sliding mode observer in the Surface Concentration Observer stage with constant input current (in simulation). Uniformly distributed noise with magnitudes of 1 mV, 10 mV, 30 mV, and 70 mV are manually injected to the voltage signal.

For linear PDEs, one can avoid projection in the observer design by utilizing methods such as backstepping [81] or optimal estimation [82]. Unfortunately, a unified theory for nonlinear PDE observer design does not yet exist. Nevertheless, results can be obtained in special cases - a topic for future work.

3.7 Limitation of the Proposed Scheme

The adaptive estimation performance is reasonably well in the simulation study and using experimental data. Nonetheless, there are limitations in the proposed algorithm. In this Chapter, we discuss and illustrate these limitations.

Flatness of Anode OCP

For the purpose of system observability, we reduce the coupled SPM and stress model by only considering the anode dynamics. A potential issue is that the open circuit potential (OCP) of the anode is generally flat, which means the sensitivity of output voltage with respect to the state is low. This may lead to large estimation error due to sensor and modeling uncertainties [83]. In order to compensate for the low sensitivity, observer with high gain is proposed. However, high gains amplify the output measurement noise, but we expect the sliding mode observer to provide certain robustness. The effect of measurement noise on the sliding mode observer performance in the surface concentration observer stage is tested in simulation with constant input current (see Figure 3.6). Uniformly distributed noise with magnitudes of 1 mV, 10 mV, 30 mV, and 70 mV are manually injected to the voltage signal. Due to the effect of high observer gain, the surface concentration estimation deviates from the actual (simulated) signal when uncertainties grow. This illustration reveals that the measurement uncertainty weakens the effectiveness of the estimation scheme owing to high observer gain.

Modeling Inadequacy

The coupled SPM and stress model adopted from [54] is derived from physical principles relying on an analogy to thermal stress, and provides a quantitative aggregated stress prediction, which is useful to understand battery SOH associated with stress. This model also has desired computational simplicity for our application. However, the model is never validated against experimental data. It is derived based on the SPM, so (i) it cannot capture the electrode localized stress as a function of position along the electrode, and (ii) its accuracy can be compromised for high input current, and electrolyte dynamics are expected to be incorporated as the electrode region in which fracture takes place depends on the electrolyte properties [84]. Moreover, reviewing dynamical equation (3.6) and Remark 4, it is evident that the effects of temperature and concentration on θ^j and D_s^j were not taken into account. Finally, the model used here does not account for phase change and staging in the electrodes, which have a significant impact on the stress generation of some materials [59].

Unknown Actual Initial Condition

To compute the estimates $\hat{\sigma}_{r,\max}$ and $\hat{\sigma}_{t,\max}$ in real time, one needs to know the change of solid phase concentration estimation from the actual stress-free value, which is recognized as the concentration profile after relaxation. In the numerical studies, the “stress-free value of concentration" is simply the actual initial condition of the solid-phase concentration in the battery cell, and apparently this information is unavailable. In the above numerical studies (for instance see Figure 3.5(a)), zero current is injected at the beginning of an input profile, which allows 1) the battery cell to relax and 2) the state observer to converge to the actual initial concentration instantly. The concentration estimation at the end of zero current can be used as the “actual” initial concentration. However, the convergence of observer within zero-current period is not guaranteed.

3.8 Conclusion

This chapter presents a nonlinear observer for mechanical stress estimation in Li-ion batteries, along with solid-phase Li-ion concentration, i.e. state of charge, and diffusion coefficient estimation. A key feature is utilizing a single particle model coupled with an intercalation-induced stress model. Monitoring the mechanical response of electrode materials is crucial because particle fracture due to stress generation is a major source of battery capacity fade. The reduced PDE system for the SPM-Stress model is approximated by nonlinear ODEs using the finite difference method. A nonlinear observer based on the sliding mode observer concept is proposed for estimating the surface concentration from current and voltage measurements only. The estimated surface concentration is then utilized as a pseudo-measurement signal for combined state and parameter estimation in the subsequent adaptive observer. The observers' convergence is mathematically proved using Lyapunov stability theory and Barbalat's Lemma. Real-time monitoring of aging related parameters in battery model and internal mechanical stress enables (i) a BMS to apply optimal control methods that protect against particle fracture, and consequently extend battery life, and (ii) further understanding of battery degradation behavior associated with diffusion-induced stress. Studies from simulation and experimental data are carried out to demonstrate observer performances.

Chapter 4

State of Charge Estimation for battery Packs With Heterogeneous Cells

A battery pack system generally consists of hundreds or thousands of single cells connected in parallel and series connections in order to fulfill the requirements of high-energy and high-power applications [85]. It is well-known that Li-ion cells are sensitive to over-charge and over-discharge [86]. An accurate estimation of the internal states for battery packs, including SOC, enables a BMS to prolong battery service life by ensuring individual cells within a pack do not over-charge or over-discharge.

Battery pack system modeling can be divided into three categories. The first approach treats the entire pack as one lumped single cell [87]. However, the internal states of individual cells within the pack are likely to be different, due to parameter heterogeneity. Therefore, some cells are more prone to violate safety-critical constraints than others, which cannot be resolved from the lumped single cell approach. The second modeling approach also relies on a single cell model, but it focuses on a set of specific in-pack cells – the weakest and the strongest ones, as representatives of the pack dynamics [85, 88]. The last modeling approach is based on the interconnection of single cell models [89, 90, 91]. This approach benefits from high fidelity cell-by-cell resolution, but it might suffer from high real-time computational burden. To counteract this computational challenge, most of these approaches resort to equivalent circuit models, which tend to have a low complexity when compared to more sophisticated electrochemical models.

The state estimation problem for series arrangements of battery cells has been studied previously [86, 92], whereas the estimation for cells in parallel has been overlooked for multiple reasons. First, cells in parallel are widely considered to behave as one single cell. However, an implicit assumption behind this reasoning is that the applied current is evenly split amongst the cells in parallel. This is hardly true in practice due to cell heterogeneities, such as non-uniform parameter values and temperatures [93]. This fact makes the estimation problem for parallel battery cells relevant. Secondly, the estimation problem for battery cells in series is arguably easier to solve than the parallel counterpart, because in the series case the input current to each battery cell is the same and it can be practically measured. In the parallel case, each cell's local currents are unknown and determined by algebraic constraints. Due to sensing limitations, only the total current can be measured. Therefore, the parallel configuration turns out to be a differential algebraic equation (DAE) system that requires non-trivial estimation theories.

A DAE system, *a.k.a.* a descriptor system, involving both differential and algebraic equations, is a powerful modeling framework that generalizes ordinary differential (normal) systems [94]. The state observer design for linear descriptor systems is a rich research topic [94, 95, 96, 97]. In contrast, state observers for nonlinear descriptor systems is less prolific. Some relevant contributions encompass a local asymptotic state observer [98], looking at the system as differential equations on a restricted manifold [99], and an index-1 DAE observer [100]. Other works consider the case of Lipschitz nonlinearities [101], which have served as a basis for Lyapunov-based observer design using the linearized system [102], and LMI approaches producing state observers in singular [103] and non-singular [104] forms. Another Lipschitz system was considered in [105], where the temporal separation between slow and fast dynamics was exploited to design a robust state observer. Nonlinear descriptor systems have also been estimated through moving horizon approaches [106] and Kalman filters [107, 108, 109].

An important fact often ignored during battery modeling is the time-varying electrical parameters. In practice, electrical model parameters, e.g. resistances and capacitance, are non-linearly dependent on the cell's SOC and temperature. High-fidelity temperature models have more accurate predictions, but suffer from high computational cost, rendering them of little use for on-board thermal management [110]. First principles-based two-state thermal model for the cell's core and surface temperatures provide a balanced trade-off between computational efficiency and fidelity [111]. Coupled equivalent circuit-thermal models with temperature dependent parameters have been studied and used for state estimation via an adaptive observer in [112]. Existing techniques for battery pack state estimation includes Luenberger observers [113], Kalman filters [114], unscented Kalman filters [115], and sliding mode observers [116], among others. However, all the previously mentioned techniques require a state observer for each cell, making them computationally intractable for large packs.

In the stochastic estimation/filtering framework, the process and measurement noises are often assumed to be Gaussian. The system characteristics, e.g. mean and variance, are required by filtering algorithms. Nonetheless, the statistical and calibration procedures to obtain these characteristics are often tedious [117]. In contrast, interval estimation [117, 118, 119] assumes that the measurement and process noises are unknown but bounded. In a battery pack with thousands of cells, executing state estimation algorithms based on highly nonlinear and coupled dynamics for every single cell in real time becomes intractable. The interval observer benefits from its scalability by deriving only upper and lower bounds that enclose all unmeasured internal states for all cells in a pack. Previously, only Perez *et al.* designed a sensitivity-based interval observer for single cell SOC estimation from an electrochemical perspective [120], but without provable observer stability and inclusion properties.

In light of the aforementioned literature, the contributions of this chapter are fourfold:

1. Propose a novel framework for modeling Li-ion battery cells in parallel as a nonlinear descriptor system. Existing studies for cells in series yield ODEs;
2. Conduct observability analysis of such a system;
3. Design a Lyapunov-based asymptotic state observer for both differential and algebraic state estimation, using only voltage and total current measurements;
4. Design/apply a novel interval observer with guaranteed stability and inclusion, given uncertain model parameters, initial conditions, and measurements.

This chapter is organized as follows. Chapter 4.1 introduces the modeling framework for parallel cells using constant electrical parameters. Chapter 4.2 motivates cell heterogeneity in a parallel cell arrangement and the importance of observer design with cell heterogeneity. Chapter 4.3 provides the local observability analysis for the nonlinear descriptor system. Chapter 4.4 discusses the state observer design and its convergence analysis. Further, a coupled electrical-thermal model considering state-dependent model parameters is developed in Section 4.5, for battery cells connected in parallel. Monotone system based interval observer preliminaries are given in Section 4.6. The interval observer design for batteries is pursued in Section 4.7. Finally, the effectiveness of the proposed approaches is illustrated in Chapter 4.8 via numerical simulations. Conclusions are drawn in Chapter 4.9.

Notation. Throughout this chapter, the symbols $I_{p\times q}$ and $\mathbf{0}_{p\times q}$ denote the identity matrix and the zero matrix with dimension $p \times q$, respectively. The symbols Id_n denotes the identity matrix with dimension $n \times n$. For a matrix $A \in \mathbb{R}^{n\times n}$, $\|A\|_{\max} = \max_{i,j=1,2,\cdots,n}\big|A_{i,j}\big|$ (the elementwise maximum norm). The relation $Q \succ 0$ ($Q \prec 0$) means that the matrix $Q \in \mathbb{R}^{n\times n}$ is positive (negative) definite. The inner product between $x, y \in \mathbb{R}^n$ is given by

$$\langle x, y\rangle = \sum_{i=1}^{n} x_i y_i .$$

4.1 Parallel Battery Model With Constant Prameters

This section first reviews an equivalent circuit model (ECM) for a single battery cell, which is then electrically interconnected with other cell models to form a parallel arrangement of cells.

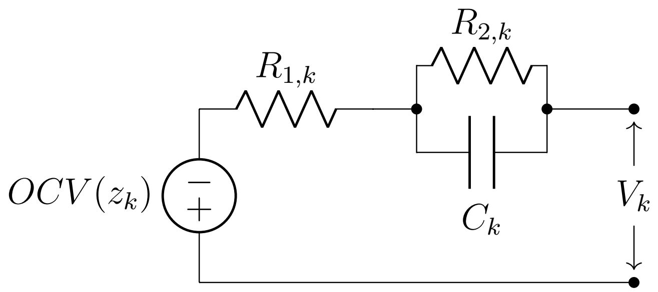

Figure 4.1: The schematic of an equivalent circuit model

Single Battery Cell

Consider the ECM for a single battery cell, shown in Fig. 4.1, represented by the following continuous-time state-space representation,

$$\dot{x}_k(t) = \overline{A}_k x_k(t) + \overline{B}_k u_k(t), \tag{4.1}$$

$$y_k(t) = h_k(x_k(t)) + \overline{D}_k u_k(t), \tag{4.2}$$

where $x_k \in \mathbb{R}^2$ is the state vector for k-th battery cell in the parallel connection defined as

$$x_k = \begin{bmatrix} z_k & V_{c,k} \end{bmatrix}^\top,$$

with z_k as the SOC and $V_{c,k}$ as the capacitor voltage of the RC pair for the k-th battery cell. In (4.1), $u_k \in \mathbb{R}$ is the applied current $u_k = I_k(t)$, and state matrix $\overline{A}_k \in \mathbb{R}^{2\times 2}$ and input matrix $\overline{B}_k \in \mathbb{R}^{2\times 1}$ are given by

$$\overline{A}_k = \begin{bmatrix} 0 & 0 \\ 0 & -\frac{1}{R_{2,k}C_k} \end{bmatrix}, \quad \overline{B}_k = \begin{bmatrix} \frac{1}{Q_k} \\ \frac{1}{C_k} \end{bmatrix}, \tag{4.3}$$

where Q_k represents the capacity of cell k, and $R_{1,k}$, $R_{2,k}$, C_k are resistances and capacitance shown in Fig. 4.1. The output equation (4.2) for the k-th cell provides the voltage response characterized by the nonlinear function,

$$h_k(x_k) = OCV(z_k) + V_{c,k}, \quad \overline{D}_k = R_{1,k}, \tag{4.4}$$

where $y_k \in \mathbb{R}$ is the battery terminal voltage, function $h_k : \mathbb{R}^2 \to \mathbb{R}$ consists of the open circuit voltage as a function of SOC denoted as $OCV(z_k)$, voltage across the RC pair $V_{c,k}$, and voltage response due to an ohmic resistance $R_{1,k}$.

Parallel Arrangement of Battery Cells

For a block of n cells in parallel, in order to reduce sensing effort, we assume only the total current and voltage for one of the cells are measured. Fig. 4.2 depicts a parallel connection of

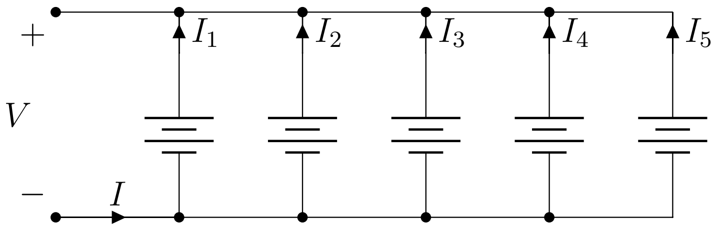

Figure 4.2: Parallel connection of five battery cells. Each battery cell is modeled by an ECM given in Fig. 4.1.

$n = 5$ cells. Electrically, Kirchhoff's voltage law indicates that a parallel connection of cells constraints terminal voltage to the same value for all cells. Kirchhoff's current law indicates that the overall current is equal to the summation of cell local currents. Mathematically, the following nonlinear algebraic constraints, according to Kirchhoff's voltage law, need to be enforced:

$$OCV(z_i) + V_{c,i} + R_{1,i}I_i = OCV(z_j) + V_{c,j} + R_{1,j}I_j, \;\; \forall i, j \in \{1, 2, \cdots, n\}, \; i \neq j. \tag{4.5}$$

Similarly, Kirchhoff's current law poses the following linear algebraic constraint with respect to cell local currents,

$$\sum_{k=1}^{n} I_k(t) = I(t), \tag{4.6}$$

where $I(t)$ is the total current applied to the parallel battery system. It is worth highlighting that (4.5) imposes $(n-1)$ nonlinear algebraic constraints with respect to differential states and local currents, whereas (4.6) imposes 1 algebraic constraint with respect to local currents. In this manuscript, it is assumed that all cells have different electrical model parameters. In addition, when only the total current is measured, the local currents of cells are unknown. Hence, the system of differential-algebraic equations must be solved such that the algebraic equations (4.5) and (4.6) are fulfilled for all t. Such methodology is realized by augmenting the local currents to the differential state vector to form a nonlinear descriptor system [94], which takes the form

$$E\dot{w}(t) = Aw(t) + \theta(w(t)), \tag{4.7}$$

$$y(t) = Hw(t) + \phi(w(t)), \tag{4.8}$$

where $w = [x \quad u]^\top \in \mathbb{R}^{3n}$ with

$$x = \begin{bmatrix} x_1 & x_2 & \cdots & x_n \end{bmatrix}^\top \in \mathbb{R}^{2n}, \tag{4.9}$$

$$u = \begin{bmatrix} I_1 & I_2 & \cdots & I_n \end{bmatrix}^\top \in \mathbb{R}^{n}, \tag{4.10}$$

$$y = \begin{bmatrix} y_1 & y_2 & \cdots & y_n \end{bmatrix}^\top \in \mathbb{R}^{n}. \tag{4.11}$$

Equation (4.7) encodes both the system dynamical equations and algebraic equations, and the matrix E is a singular matrix of the form

$$E = \begin{bmatrix} I_{2n\times 2n} & \mathbf{0}_{2n\times n} \\ \mathbf{0}_{n\times 2n} & \mathbf{0}_{n\times n} \end{bmatrix} \in \mathbb{R}^{3n\times 3n}, \tag{4.12}$$

where $I_{2n\times 2n}$ is an identity matrix of size $2n$-by-$2n$. Matrix A accounts for the linear part of the system equations with

$$A = \begin{bmatrix} A_{11} & A_{12} \\ A_{21} & A_{22} \end{bmatrix} \in \mathbb{R}^{3n\times 3n}, \tag{4.13}$$

where

$$\begin{aligned}
A_{11} &= \operatorname{diag}\left(\overline{A}_1, \overline{A}_2, \cdots, \overline{A}_n\right), \quad A_{12} = \operatorname{diag}\left(\overline{B}_1, \overline{B}_2, \cdots, \overline{B}_n\right), \\
A_{21} &= \begin{bmatrix} 0 & 1 & S & 0 & \cdots & 0 \\ 0 & 1 & 0 & S & \cdots & 0 \\ \vdots & \vdots & \vdots & \vdots & \ddots & \vdots \\ 0 & 1 & 0 & 0 & \cdots & S \\ 0 & 0 & 0 & 0 & \cdots & 0 \end{bmatrix} \in \mathbb{R}^{n\times 2n}, \quad S = \begin{bmatrix} 0 & -1 \end{bmatrix}, \\
A_{22} &= \begin{bmatrix} R_{1,1} & -R_{1,2} & 0 & \cdots & 0 \\ R_{1,1} & 0 & -R_{1,3} & \cdots & 0 \\ \vdots & \vdots & \vdots & \ddots & \vdots \\ R_{1,1} & 0 & 0 & \cdots & -R_{1,n} \\ 1 & 1 & 1 & \cdots & 1 \end{bmatrix} \in \mathbb{R}^{n\times n}.
\end{aligned} \tag{4.14}$$

Notice that matrix A_{22} is full rank, i.e. the linear part of the descriptor model is regular and impulsive free.

Function $\theta(w)$ constitutes the nonlinear portion in the system equations from the voltage algebraic constraints (4.5):

$$\theta(w) = \begin{bmatrix} \theta_x(w) \\ \theta_u(w) \end{bmatrix} = \begin{bmatrix} \mathbf{0}_{2n\times 1} \\ OCV(z_1) - OCV(z_2) \\ \vdots \\ OCV(z_1) - OCV(z_n) \\ -I(t) \end{bmatrix} \in \mathbb{R}^{3n}, \tag{4.15}$$

where $\theta_x \in \mathbb{R}^{2n}$ represents nonlinearity in the dynamical equations and corresponds to row 1 through row $2n$ of $\theta(w)$, and $\theta_u \in \mathbb{R}^n$ is nonlinearity appears in the algebraic equations and corresponds to row $(2n+1)$ through row $3n$ of $\theta(w)$. The output (4.8) models the voltage of each battery cell, with

$$H = \left[H_x \;\; H_u\right], \quad \phi(w) = \left[OCV(z_1) \;\; \cdots \;\; OCV(z_n)\right]^\top \tag{4.16}$$

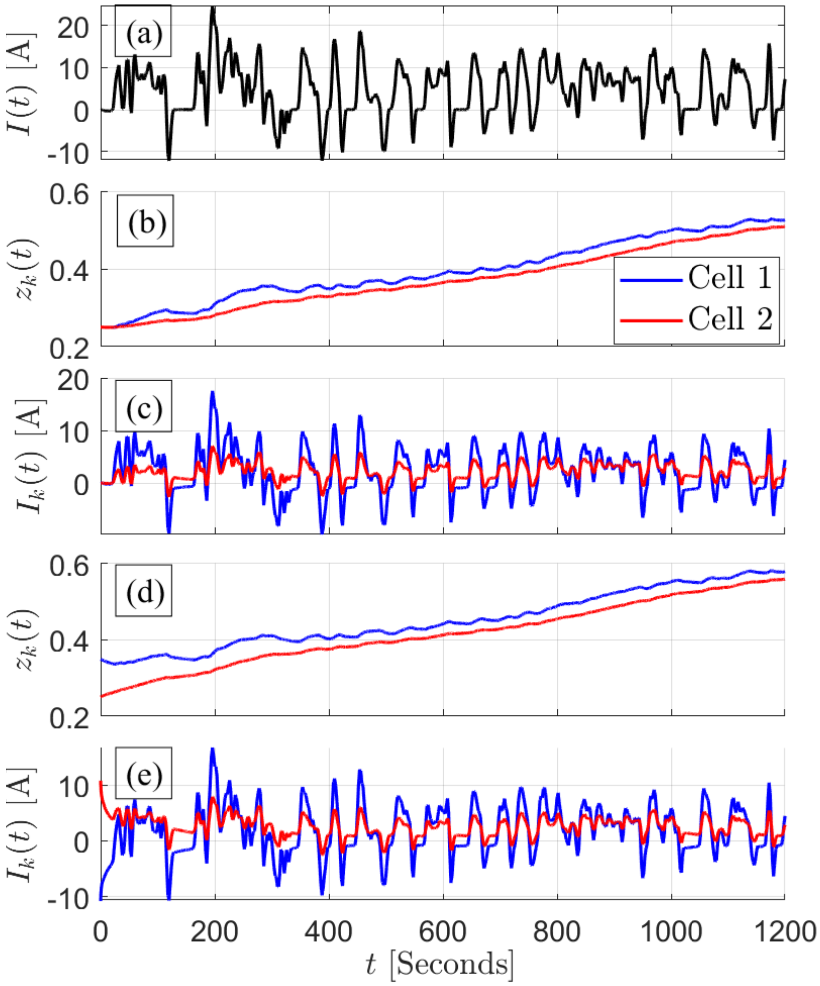

Figure 4.3: Simulation results of two cells in parallel using coupled electrical-thermal dynamics with temperature and SOC dependent electrical parameters. In (b)-(c), cells are initialized at the same SOC, and the total current distributes unevenly due to parameter heterogeneity. In (d)-(e), the initial cell SOCs are distinct. The total current again distributes unevenly due to both parameter and initialization heterogeneity.

where H_x corresponds to column 1 through column $2n$ of matrix H, and H_u corresponds to column $(2n+1)$ through column $3n$ of matrix H:

$$H_x = \text{diag}(-S, -S, \cdots, -S) \in \mathbb{R}^{n\times 2n}, \tag{4.17}$$

$$H_u = \text{diag}(R_{1,1}, R_{1,2}, \cdots, R_{1,n}) \in \mathbb{R}^{n\times n}. \tag{4.18}$$

The model introduced above will be used in the analysis and designs in the subsequent sections.

4.2 Motivation

We demonstrate heterogeneity for cells connected in parallel via an open-loop simulation. Without loss of generality, we study a block configuration of two $\mathrm{LiNiMnCoO_2}$/Graphite (NMC) type cells with 2.8 Ah nominal capacity in parallel. In this embodiment, the cells have identical SOC-OCV relationship, and the heterogeneity arises from:

- Difference in SOC initialization;
- Difference in electrical parameters;
- Unevenly distributed currents due to parameter variation;
- Difference in temperature due to uneven current distribution;

A transient electric vehicle-like charge/discharge cycle generated from urban dynamometer driving schedule (UDDS) is applied. Specifically, the total applied current (summation of local currents) is plotted in Fig. 4.3(a).

Two cases are examined here. In the first case, the cells are initialized at the same SOC, $z_k(0) = 0.25$ for $k \in \{1, 2\}$, but they differ in model parameters. Since Cell 2 has larger resistance, its local current is smaller in magnitude relative to local current of Cell 1, while the summation of the local currents equals to the total applied current for all t, as shown in Fig. 4.3(b) and (c). In the second case, illustrated in Fig. 4.3(d) and (e), the cells are initially different in both SOC initialization ($z_1(0)$ at 0.35 and $z_2(0)$ at 0.25) and model parameters. It can be observed that even though the applied total current is small (around zero) initially, Cell 1 takes large negative current (around -10 A) and Cell 2 positions itself at a large positive current (around 10 A). This occurs because $z_1(0)$ is initialized higher, and even though the z values for two cells follow a similar trend, they do not synchronize. Since conventional BMSs do not monitor the local current of each parallel cell, some cells might be operating outside their safe operating region. Therefore, it will be of significant value to estimate and monitor the local currents and SOCs caused by cell heterogeneity to ensure safe battery pack operation.

Additionally, in a battery pack composed of hundreds or thousands of heterogeneous cells, executing state estimation algorithms based on a highly nonlinear and coupled model consists of differential-algebraic equations for every single cell in real-time is intractable and not scalable. This motivates the study on interval observers to increase algorithm scalability and reduce computation and design complexity

4.3 Observability Analysis

In this section, we mathematically analyze the observability of the nonlinear descriptor system with the input-output setup, via (i) linearization and (ii) Lie algebra.

Observability from Linearization

In order to study the observability of the nonlinear descriptor system (4.7)-(4.8), we linearize the system around an equilibrium point $w = \overline{w}$ and check the observability conditions for the linearized system. If the linearized system is observable at $w = \overline{w}$, then the nonlinear system is locally observable. However, the observability conditions arising from linearizing the nonlinear system can be conservative, and nothing can be concluded for the nonlinear system if the linearized system is *not* observable. The linearized model of (4.7)-(4.8) takes the form

$$E\dot{w}(t) = Fw(t) + Bu(t), \tag{4.19}$$

$$y(t) = Cw(t), \tag{4.20}$$

where the state matrix $F \in \mathbb{R}^{3n\times 3n}$ and output matrix $C \in \mathbb{R}^{n\times 3n}$ are given by

$$F = A + \frac{d\theta}{dw}(w)\bigg|_{w=\overline{w}}, \quad C = H + \frac{d\phi}{dw}(w)\bigg|_{w=\overline{w}}. \tag{4.21}$$

with matrix A and H provided in (4.13) and (4.16), respectively.

Let us now introduce the definition of complete observability (C-observability) for the descriptor system (4.19)-(4.20).

Theorem 5 ([94]). *The regular descriptor linear system* (4.19)-(4.20) *is C-observable if and only if the following two conditions hold:*

C.1 rank $\left\{[E^\top, C^\top]^\top\right\} = 3n$;

C.2 rank $\left\{[(sE - F)^\top, C^\top]^\top\right\} = 3n, \ \forall s \in \mathbb{C}$.

Condition C.1 concerns C-observability of the fast (algebraic) subsystem while C.2 involves the slow (dynamic) subsystem. Focusing first on condition C.1, it can be verified by construction since all cells in a parallel connection have the same voltage and therefore it is equivalent to measure the voltage of cell i or j, with $i \neq j$. Looking at condition C.2, it can be verified if the considered battery cells in parallel are different in terms of any model parameter among $\{Q, R_1, R_2, C, \mathrm{d}OCV/\mathrm{d}z\}$. Finally, $\mathrm{d}OCV/\mathrm{d}z \neq 0$ is also required in order to guarantee condition C.2, i.e. if one of the cell's OCV curves becomes flat, then the observability of the dynamic linearized subsystem is lost. Notice that the verification of condition C.2 requires the numerical computation of the generalized eigenvalues of the pair (E, A).

Local Observability from Lie Algebra

To elucidate if less conservative observability conditions exist, we analyze local observability for the nonlinear system resulting from a reduced descriptor system. That is, we analyze the system that results from eliminating the algebraic states through substitution. System

(4.7)-(4.8) can be divided into differential and algebraic states with an explicit input current, i.e.

$$\begin{bmatrix} I_{2n\times 2n} & 0 \\ 0 & 0 \end{bmatrix} \dot{w}(t) = \begin{bmatrix} A_{11} & A_{12} \\ A_{21} & A_{22} \end{bmatrix} w(t) + \begin{bmatrix} 0 \\ \theta_I \end{bmatrix} I(t) + \begin{bmatrix} \theta_x(w) \\ \theta_{OCV}(w) \end{bmatrix}, \tag{4.22}$$

$$y(t) = \begin{bmatrix} H_1 & H_2 \end{bmatrix} w(t) + \phi(w). \tag{4.23}$$

where $\theta_I = [0, \cdots, -1]^\top \in \mathbb{R}^n$ and $\theta_{OCV}(w) = \theta_u(w) - \theta_I I(t)$. Eq. (4.22) can be solved for the algebraic state, resulting in the following transformation

$$u = -A_{22}^{-1}\left(A_{21}x(t) + \theta_I I(t) + \theta_{OCV}(w)\right) \tag{4.24}$$

where matrix A_{22} in (4.14) is non-singular. Notice that (4.24) is an explicit solution for the algebraic state $u(t)$, i.e. the w-dependent functions $\theta_{OCV}(w)$ and $\phi(w)$ are now only dependent on the dynamic state $x(t)$. With an abuse of notation, these functions are denoted as $\theta_{OCV}(x)$ and $\phi(x)$ in the remainder of this Chapter. For its part, $\theta_x(w) = \mathbf{0}_{2n\times 1} = \theta_x$.

Substituting (4.24) back into the differential part of the state equation (4.22) and the output equation (4.23) yields the following nonlinear (control affine) reduced model

$$\dot{x}(t) = f(x(t)) + g(x(t))I(t), \tag{4.25}$$

$$\overline{y}(t) = h(x(t)), \tag{4.26}$$

with

$$f(x) = (A_{11} - A_{12}A_{22}^{-1}A_{21})x(t) - A_{12}A_{22}^{-1}\theta_{OCV}(x) + \theta_x, \tag{4.27}$$

$$g(x) = -A_{12}A_{22}^{-1}\theta_I, \tag{4.28}$$

$$h(x) = (H_1 - H_2A_{22}^{-1}A_{21})x(t) - H_2A_{22}^{-1}\theta_{OCV}(x) + \phi(x), \tag{4.29}$$

where the output $\overline{y}(t) = y(t) - H_2A_{22}^{-1}\theta_I I(t)$.

Let us now introduce the notion of local observability [121] for system (4.25)-(4.26).

Theorem 6. *The system* (4.25)-(4.26) *is locally observable around* $x_0 \in X$ *if there exists* n *linearly independent row vectors in the set*

$$(\mathrm{d}L_{z_s}L_{z_{s-1}}\dots L_{z_1}h_j)(x_0)$$

where $L_{z_s}h_j$ *are Lie derivatives of* h_j *with respect to* z_s *and* $\mathrm{d}h_j$ *is the gradient of* h_j *to be defined below,* $s \geq 0$ *and* $z_i \in \{f, g\}$*, with* $j = 1, \dots, p$ *(*p *is the number of outputs) and* $i = 1, \dots, s$ *(for* $s = 0$*, the set comprises* $\mathrm{d}h_j(x_0)$*).*

In Theorem 6, the gradient of h_j and Lie derivatives of h_j with respect to function f are given by

$$\mathrm{d}h_j = \begin{bmatrix} \frac{\partial h_j}{\partial x_1} & \frac{\partial h_j}{\partial x_2} & \cdots & \frac{\partial h_j}{\partial x_n} \end{bmatrix},$$

$$L_f h_j = \langle \mathrm{d}h_j, f \rangle, \tag{4.30}$$

and similarly for function g. The 0th order Lie derivative $L_f^0 h_j$ is defined as h_j whereas the 2nd order Lie derivative takes the form $L_f^2 h_j = L_f L_f h_j$.

According to Theorem 6, the observability rank condition can be derived. Define the observability matrix as

$$\mathcal{O}(x) = \begin{bmatrix} \mathrm{d}h(x) \\ \mathrm{d}L_f h(x) \\ \mathrm{d}L_g h(x) \\ \mathrm{d}L_f^2 h(x) \\ \mathrm{d}L_g^2 h(x) \\ \vdots \end{bmatrix}. \tag{4.31}$$

Then the model (4.25)-(4.26) is locally observable around x_0 if $\mathrm{rank}(\mathcal{O}) = 2n$. Note first that the observability matrix $\mathcal{O}$ is not bounded from above. Secondly, this matrix depends on states $x_k = [z_k, V_{c,k}]^\top$, functions $OCV_k(z_k)$ as well as parameters $\theta_k = [R_{1,k}, \tau_k, C_k, Q_k]^\top$, where $\tau_k = -1/(R_{2,k}C_k)$.

To keep the observability analysis tractable, we consider two cells in parallel, i.e. $k \in \{1, 2\}$. From the observability rank condition, we conclude: (i) the system is locally observable at x_0 if cells have different parameter values θ_k, and (ii) observability conditions are not fulfilled if the cells are completely equivalent, i.e. all parameter values are uniform across the cells. In the second case, the cells are presumably indistinguishable and a single cell model can be utilized to represent the parallel connection. In between these two extremes, the observability conditions cannot be verified if any of the following conditions hold:

1. the parameters $\tau_1 = \tau_2$ and $R_{1,1}Q_1 = R_{1,2}Q_2$ and $R_{1,1}C_1 = R_{1,2}C_2$;
2. the functions $OCV(z_1) = OCV(z_2)$ and $\mathrm{d}OCV(z_1)/\mathrm{d}z_1 = \mathrm{d}OCV(z_2)/\mathrm{d}z_2$;
3. at least one of the l-th OCV derivatives satisfy $\mathrm{d}^l OCV(z_j)/\mathrm{d}z_j^l = 0$, for the j-th cell and $l = 1, \ldots, \infty$.

Note that a classical approach to study observability of a single ECM is to linearize the model, as done in e.g. [122], for the case of two battery cells in parallel. By doing so, the ECM is observable if $\mathrm{d}OCV/\mathrm{d}z \neq 0$. This condition on the first OCV derivative is conservative as it was found in [123] through the local observability analysis of a single cell. This more detailed analysis showed that an OCV derivative must be different than zero to guarantee local observability, but it does not need to be the first derivative. This fact was also verified above with a similar analysis for two ECMs in parallel.

A similar observability analysis as the one proposed here was also carried out in [86] considering cells in series. However, the observability matrix for a series string differs from that of a parallel arrangement. Namely, in the series arrangement, each cell's parameters/states appear in a column of $\mathcal{O}$. This is not the case for a parallel topology, where parameters/states of the cells are scattered all over the different entries in $\mathcal{O}$. Therefore, parameters/states of one cell influence the local observability of the neighbouring cell in a parallel arrangement.

When compared to the observability analysis of Theorem 5 based on the linearized descriptor system, the local observability analysis of the nonlinear system using Theorem 6 is less conservative [121] and more informative. The latter aspect relies on the fact that the observability matrix $\mathcal{O}$ explicitly depends on model parameters, and it can be analytically obtained through e.g. symbolic software.

4.4 Design of State Observers

The following observer with linear output error injection is proposed for the plant model (4.7)-(4.8)

$$E\dot{\hat{w}} = A\hat{w} + \theta(\hat{w}) + K(y - H\hat{w} - \phi(\hat{w})), \tag{4.32}$$

$$\hat{y} = H\hat{w} + \phi(\hat{w}), \tag{4.33}$$

where $K \in \mathbb{R}^{3n}$ is the observer gain vector to be designed and $\hat{w}$ is the estimation for w. The following theorem based on [101, 102] establishes the convergence results of the proposed observer.

Theorem 7. *Consider the plant model dynamics (4.7)-(4.8), and suppose the matrix* $\begin{bmatrix} A_{22} & H_u \end{bmatrix}^\top$ *has rank* n. *Let*

$$G = (A - KH) = \begin{bmatrix} G_{11} & G_{12} \\ G_{21} & G_{22} \end{bmatrix}, \tag{4.34}$$

and define the matrix

$$\widetilde{G} = (G_{11} - G_{12}G_{22}^{-1}G_{21}). \tag{4.35}$$

Suppose the function

$$f(w) = \theta_x(w) - G_{12}G_{22}^{-1}\theta_u(w) + (G_{12}G_{22}^{-1}K_u - K_x)\phi(w), \tag{4.36}$$

is Lipschitz continuous with respect to x, *i.e.,*

$$\|f(x_1, u) - f(x_2, u)\| \leq \gamma\|x_1 - x_2\|, \tag{4.37}$$

where $\gamma \in \mathbb{R}$ *is the Lipschitz constant. If the observer gain* K *is chosen to ensure that* $\widetilde{G}$ *is stable, and*

$$\min_{\omega \in \mathbb{R}^+} \lambda_{\min}(A - KH - j\omega I_{3n\times 3n}) > \gamma, \tag{4.38}$$

then the zero equilibrium of the dynamics of estimation error $e(t) = w(t) - \hat{w}(t)$ *given by*

$$E\dot{e} = Ge + \theta(w) - \theta(\hat{w}) - K\left[\phi(w) - \phi(\hat{w})\right] \tag{4.39}$$

is asymptotically convergent to zero.

Proof. Let the state estimation error $e = \begin{bmatrix} e_x & e_u \end{bmatrix}^\top$, with $e_x = x - \hat{x}$ being the estimation error for the differential states and $e_u = u - \hat{u}$ the estimation error for the algebraic states. Then (4.39) can be written as

$$\begin{bmatrix} I_{2n\times 2n} & \mathbf{0} \\ \mathbf{0} & \mathbf{0} \end{bmatrix} \begin{bmatrix} \dot{e}_x \\ \dot{e}_u \end{bmatrix} = \begin{bmatrix} G_{11} & G_{12} \\ G_{21} & G_{22} \end{bmatrix} \begin{bmatrix} e_x \\ e_u \end{bmatrix} + \begin{bmatrix} \theta_x(w) - \theta_x(\hat{w}) \\ \theta_u(w) - \theta_u(\hat{w}) \end{bmatrix} - \begin{bmatrix} K_x \\ K_u \end{bmatrix} [\phi(w) - \phi(\hat{w})]. \quad (4.40)$$

We highlight that G_{22} can be non-singular (i.e., invertible) if the linear part of (4.7) is impulse observable [102], i.e., the matrix $\begin{bmatrix} A_{22} & H_u \end{bmatrix}^\top$ has rank n. Then the estimation error system (4.40) is equivalently described by

$$\begin{aligned} \dot{e}_x = & \left(G_{11} - G_{12}G_{22}^{-1}G_{21}\right) e_x + \left[\theta_x(w) - G_{12}G_{22}^{-1}\theta_u(w)\right] - \left[\theta_x(\hat{w}) - G_{12}G_{22}^{-1}\theta_u(\hat{w})\right] \\ & + \left(G_{12}G_{22}^{-1}K_u - K_x\right)\phi(w) - \left(G_{12}G_{22}^{-1}K_u - K_x\right)\phi(\hat{w}) \\ = & \widetilde{G}e_x + f(w) - f(\hat{w}), \end{aligned} \quad (4.41)$$

along with the algebraic equation

$$e_u = -\,G_{22}^{-1}G_{21}e_x - G_{22}^{-1}\left[\theta_u(w) - \theta_u(\hat{w})\right] + G_{22}^{-1}K_u\left[\phi(w) - \phi(\hat{w})\right]. \quad (4.42)$$

Consider the following Lyapunov function for the error system (4.41), corresponding to the differential states e_x,

$$W(t) = \frac{1}{2}e_x^\top P e_x. \quad (4.43)$$

The derivative of the Lyapunov function $W(t)$ along the trajectory of e_x is computed by

$$\begin{aligned} \dot{W} &= \frac{1}{2}\dot{e}_x^\top P e_x + \frac{1}{2}e_x^\top P \dot{e}_x \\ &= \frac{1}{2}e_x^\top(\widetilde{G}^\top P + P\widetilde{G})e_x + e_x^\top P\left[f(w) - f(\hat{w})\right] \\ &\le \frac{1}{2}e_x^\top(\widetilde{G}^\top P + P\widetilde{G})e_x + \|Pe_x\|\left[\|f(w) - f(\hat{w})\|\right] \\ &\le \frac{1}{2}e_x^\top(\widetilde{G}^\top P + P\widetilde{G})e_x + \gamma\|Pe_x\|\|e_x\| \\ &\le \frac{1}{2}e_x^\top\left[\widetilde{G}^\top P + P\widetilde{G} + \gamma^2 PP + I\right]e_x, \end{aligned} \quad (4.44)$$

where the inequality

$$2\gamma\|Pe_x\|\|e_x\| \le \gamma^2 e_x^\top PPe_x + e_x^\top e_x \quad (4.45)$$

has been utilized. According to Theorem 2 in [101], the estimation error e_x is asymptotically stable if the conditions of Theorem 7 hold. Under this scenario, when $t \to \infty$, $[\theta_u(w) - \theta_u(\hat{w})] \to \mathbf{0}_{n\times 1}$, and $[\phi(w) - \phi(\hat{w})] \to 0$. Hence, the estimation error e_u for the algebraic states also converge to zero asymptotically. ■

In the subsequent sections, we incorporate battery thermal dynamics and SOC and temperature dependent electrical parameters for a more realistic representation of battery packs. In this scenario, estimation of the states for each individual cell in a parallel connection becomes intractable to design and execute. This fact stimulates the interval observer design, which is detailed in Chapter 4.6 and 4.7.

4.5 Parallel Battery Model With State-Dependent Parameters

This section reviews an equivalent-circuit model coupled with a two-state thermal model for a single battery cell, which is then electrically and thermally interconnected with other cell models to form a parallel arrangement of cells.

Single Battery Cell

The ECM for a single cell k, consisting of an open circuit voltage (OCV) in series connection with an ohmic resistance and an $R-C$ pair in parallel, is described by

$$\dot{z}_k(t) = \frac{1}{Q_k} I_k(t), \tag{4.46}$$

$$\dot{V}_{c,k}(t) = -\frac{1}{R_{2,k}(z_k, T_k) C_k(z_k, T_k)} V_{c,k}(t) + \frac{1}{C_k(z_k, T_k)} I_k(t), \tag{4.47}$$

$$V_k(t) = OCV(z_k(t)) + V_{c,k}(t) + R_{1,k}(z_k, T_k) I_k(t), \tag{4.48}$$

where $z_k(t)$ represents the SOC for the k-th cell, and $V_{c,k}(t)$ denotes the voltage across the $R_{2,k} - C_k$ pair. Symbol $R_{1,k}$ is the ohmic resistance, and T_k is the cell temperature given by (4.52). The electrical model parameters, namely $R_{1,k}$, $R_{2,k}$, and C_k, are dependent on cell local SOC and temperature, and such dependence can be explicitly characterized via an offline experimental procedure for a cell of interest (see [11] for an example for a $LiFePO_4$/Graphite cell). The output equation (4.48) for the k-th cell provides the voltage response characterized by a nonlinear open circuit voltage (OCV) as a function of SOC, voltage from the R-C pair, and voltage associated with an ohmic resistance $R_{1,k}$. We specify positive current for charging and negative current for discharging.

A two-state thermal model for a cylindrical cell describes the dynamics of core and surface temperatures [11]:

$$C_c\dot{T}_{c,k}(t) = \dot{Q}_k(t) + \frac{T_{s,k}(t) - T_{c,k}(t)}{R_c}, \tag{4.49}$$

$$C_s\dot{T}_{s,k}(t) = \frac{T_{f,k}(t) - T_{s,k}(t)}{R_u} - \frac{T_{s,k}(t) - T_{c,k}(t)}{R_c}, \tag{4.50}$$

$$\dot{Q}_k(t) = \Big| I_k(t)\left[V_k(t) - OCV(z_k(t))\right]\Big|, \tag{4.51}$$

$$T_k(t) = \frac{1}{2}\left(T_{s,k}(t) + T_{c,k}(t)\right), \tag{4.52}$$

where $T_{c,k}$ and $T_{s,k}$ are the core and surface temperatures for the k-th cell. Symbols R_c, R_u, C_c, and C_s represent heat conduction resistance between core and surface, convection resistance between ambient and surface, core heat capacity, and surface heat capacity, respectively. Symbol $\dot{Q}_k(t) \geq 0$ is the internal heat generation from resistive dissipation. Note that the electrical model (4.46)-(4.48) and the thermal model (4.49)-(4.52) are coupled via $\dot{Q}_k(t)$ in a nonlinear fashion.

The measured quantities for the coupled electrical-thermal model (4.46)-(4.52) are the cell voltage and surface temperature:

$$y_k(t) = \left[V_k(t),\ T_{s,k}(t)\right]. \tag{4.53}$$

Parallel Arrangement of Battery Cells

As described in Chapter 4.1, for a block of n cells in parallel, only the voltage and total current for the block are measured. Electrically, Kirchhoff's voltage law and current must be obeyed. See Chapter 4.1 for more details.

On the other hand, when cells are packed. they are thermally coupled through coolant flow and heat exchange between adjacent cells [124]. For cell k,

$$C_c\dot{T}_{c,k}(t) = \dot{Q}_k(t) + \frac{T_{s,k}(t) - T_{c,k}(t)}{R_c}, \tag{4.54}$$

$$C_s\dot{T}_{s,k}(t) = \frac{T_{f,k}(t) - T_{s,k}(t)}{R_u} - \frac{T_{s,k}(t) - T_{c,k}(t)}{R_c} + \frac{T_{s,k-1}(t) + T_{s,k+1}(t) - 2T_{s,k}(t)}{R_{cc}}, \tag{4.55}$$

$$T_{f,k}(t) = T_{f,k-1}(t) + \frac{T_{s,k-1}(t) - T_{f,k-1}(t)}{R_u C_f}, \tag{4.56}$$

$$\dot{Q}_k(t) = \Big| I_k(t)\left[y_k(t) - OCV(z_k(t))\right]\Big|, \tag{4.57}$$

$$T_k(t) = \frac{1}{2}(T_{s,k}(t) + T_{c,k}(t)), \tag{4.58}$$

where $T_{f,k}$ is the coolant flow temperature at the k-th cell, and R_{cc} denotes heat conduction resistance between adjacent battery cell surfaces. Heat conduction between battery cells is driven by the temperature difference between cell surfaces, and this process is described by the third term on the right hand side of (4.55). Inside the block of n cells in parallel, the coolant flows through individual cells, and the coolant flow temperature at the k-th cell is determined by the flow heat balance of the previous cell, as illustrated in (4.56). Suppose that all the battery cells have the same thermal parameters, namely R_c, R_u, C_c, and C_s.

4.6 Interval Observer Preliminaries

The development of finite-dimensional interval observers based on monotone system theory closely follows the work in [117, 118, 119]. In this section, the preliminaries is reviewed.

Consider the following nonlinear model dynamics [119]:

$$\dot{x} = f(x) + B(\theta(t))u + \delta f(x, \theta(t)), \tag{4.59}$$

$$y = h(x) + \delta h(\theta(t))u, \tag{4.60}$$

where $x \in \mathbb{R}^n$ is the state vector, and $u \in \mathbb{R}$ and $y \in \mathbb{R}$ are the system input and output, respectively. The considered system is single-input-single-output (SISO). The functions $f(x)$ and $h(x)$ are deterministic and smooth, and δf is uncertain and assumed to be locally Lipschitz continuous with respect to x. It is noted that the nominal terms $f(x)$ and $h(x)$ can be freely assigned by the designer via the modification of δf and δh. The initial conditions for the states belong to a compact set $x_0 \in [\underline{x}_0, \overline{x}_0]$, where $\underline{x}_0$ and $\overline{x}_0$ are given. Suppose the uncertain parameters $\theta(t)$ belong to a compact set $\Theta \subset \mathbb{R}^p$, where p is the number of parameters. The values of the parameter vector $\theta(t)$ are not available for measurement, and only the set of admissible values Θ is known. One can obtain a nominal system of (4.59)-(4.60) by setting $B = 0$, $\delta f = 0$, and $\delta h = 0$:

$$\dot{x} = f(x), \tag{4.61}$$

$$y = h(x). \tag{4.62}$$

According to [117, 31], a time-varying nonlinear and invertible state transformation, based on the Lie derivatives, yields a partial-linear dynamics in the new state coordinate.

Denote the gradient of a scalar field h by $\mathrm{d}h$, and the Lie derivative of h along a vector field f is given by the inner product $L_f h(x) = \langle \mathrm{d}h(x), f(x) \rangle$. High-order Lie derivatives are computed with the iteration $L_f^k h(x) = L_f(L_f^{k-1} h(x))$ where $L_f^0 h(x) = h(x)$. The nominal system (4.61)-(4.62) is locally observable around $x = x_e$ if the matrix

$$\mathcal{O}(x_e) = \begin{bmatrix} \mathrm{d}h(x_e) \\ \mathrm{d}L_f h(x_e) \\ \vdots \\ \mathrm{d}L_f^{n-1} h(x_e) \end{bmatrix} \tag{4.63}$$

has full rank. Under this scenario, the vectors $h(x)$, $L_f h(x)$, $\cdots$, $L_f^{n-1}h(x)$ form the new coordinate for the states in a neighborhood of x defined by

$$\Phi(x) = \begin{bmatrix} \phi_1(x) \\ \phi_2(x) \\ \vdots \\ \phi_n(x) \end{bmatrix} = \begin{bmatrix} h(x) \\ L_f h(x) \\ \vdots \\ L_f^{n-1}h(x) \end{bmatrix}, \tag{4.64}$$

and the transformation map $\xi = \Phi x$ is a local diffeomorphism. The coordinate transformation obtained from the locally observable nominal system (4.61)-(4.62) is then utilized to transform the original uncertain system (4.59)-(4.60) into a partial-linear expression

$$\dot{\xi} = A_0\xi + \delta A(\theta)\xi + b(\xi, \theta), \tag{4.65}$$

$$y = H\xi + v(\theta, t), \tag{4.66}$$

where $v(\theta, t) = \delta h(\theta)u$. The matrix $A_0 \in \mathbb{R}^n$ is deterministic and the matrix $\delta A(\theta) \in \mathbb{R}^n$ represents the uncertain part inherited from the uncertain nonlinear system (4.59)-(4.60). Symbol $b(\xi, \theta)$ indicates a lumped uncertain nonlinear function. Since $\theta \in \Theta$, the following assumptions will be used.

Assumption 2. *$\underline{\delta A} \le \delta A(\theta) \le \overline{\delta A}$, $\underline{b}(t) \le b(\xi, \theta) \le \overline{b}(t)$, $\left|v(\theta, t)\right| \le V(t)$, for all $\theta \in \Theta$ and $t \ge 0$.*

Definition 1 ([118])**.** *For a matrix $\mathcal{A} \in \mathbb{R}^{n\times n}$, define $\mathcal{A}^+ = \max\{0, \mathcal{A}\}$ and $\mathcal{A}^- = \mathcal{A}^+ - \mathcal{A}$. For a vector $\xi \in \mathbb{R}^n$, define $\xi^+ = \max\{0, \xi\}$ and $\xi^- = \xi^+ - \xi$.*

According to Assumption 2 and Definition 1, the following lemma is then realized.

Lemma 8 ([118])**.** *Let $\underline{\delta A} \le \delta A(\theta) \le \overline{\delta A}$ for some $\underline{\delta A}, \delta A, \overline{\delta A} \in \mathbb{R}^{n\times n}$, and $\underline{\xi} \le \xi \le \overline{\xi}$ for $\underline{\xi}, \overline{\xi}, \xi \in \mathbb{R}^n$, then*

$$\underline{\delta A}^+\underline{\xi}^+ - \overline{\delta A}^+\underline{\xi}^- - \underline{\delta A}^-\overline{\xi}^+ + \overline{\delta A}^-\overline{\xi}^- \le \delta A(\theta)\xi \le \overline{\delta A}^+\overline{\xi}^+ - \underline{\delta A}^+\overline{\xi}^- - \overline{\delta A}^-\underline{\xi}^+ + \underline{\delta A}^-\underline{\xi}^-. \tag{4.67}$$

For a vector $L \in \mathbb{R}^n$, system (4.65)-(4.66) can be rewritten as

$$\begin{aligned} \dot{\xi} &= A_0\xi + \delta A(\theta)\xi + b(\xi, \theta) + L(y - H\xi - v(\theta, t)) \\ &= (A_0 - LH)\xi + \delta A(\theta)\xi + b(\xi, \theta) + L(y - v(\theta, t)), \end{aligned} \tag{4.68}$$

The following interval observer structure is proposed [118],

$$\dot{\underline{\xi}} = (A_0 - LH)\underline{\xi} + (\underline{\delta A}^+\underline{\xi}^+ - \overline{\delta A}^+\underline{\xi}^- - \underline{\delta A}^-\overline{\xi}^+ + \overline{\delta A}^-\overline{\xi}^-) + \underline{L}y - |\underline{L}|\, V(t) + \underline{b}(t), \tag{4.69}$$

$$\dot{\overline{\xi}} = (A_0 - LH)\overline{\xi} + (\overline{\delta A}^+\overline{\xi}^+ - \underline{\delta A}^+\overline{\xi}^- - \overline{\delta A}^-\underline{\xi}^+ + \underline{\delta A}^-\underline{\xi}^-) + \overline{L}y + \left|\overline{L}\right| V(t) + \overline{b}(t) \tag{4.70}$$

The following theorem provides a sufficient condition for stability and enclosure of the interval observer design.

Theorem 9 ([118]). *Let Assumption 2 be satisfied and the matrices* $(A_0 - \underline{L}H)$ *and* $(A_0 - \overline{L}H)$ *are Metzler. Then* $\underline{\xi}(t) \leq \xi(t) \leq \overline{\xi}(t)$, $\forall\ t \geq 0$ *is satisfied provided that* $\underline{\xi}_0 \leq \xi_0 \leq \overline{\xi}_0$. *Furthermore, if there exists* $P \in \mathbb{R}^{2n \times 2n}$, $P = P^\top \succ 0$ *and* $\gamma > 0$ *such that the following Riccati matrix inequality is verified*

$$G^\top P + PG + 2\gamma^{-2}P^2 + \gamma^2\eta^2 Id_{2n} + Z^\top Z \prec 0, \tag{4.71}$$

where $\eta = 2n\|\overline{\delta A} - \underline{\delta A}\|_{\max}$, $Z \in \mathbb{R}^{s \times 2n}$, $0 < s \leq 2n$ *and*

$$G = \begin{bmatrix} A_0 - \underline{L}H + \underline{\delta A}^+ & -\underline{\delta A}^- \\ -\overline{\delta A}^- & A_0 - \overline{L}H + \overline{\delta A}^+ \end{bmatrix}, \tag{4.72}$$

then $\underline{\xi}$, $\overline{\xi} \in \mathcal{L}_\infty^n$. *Moreover,*

$$\underline{x} = \inf\left(\Phi^{-1}(\eta)\right), \quad \overline{x} = \sup\left(\Phi^{-1}(\eta)\right), \tag{4.73}$$

where $\eta \in \left[\underline{\xi}, \overline{\xi}\right]$.

The proof for Theorem 9 is omitted here. Interested readers may refer to [118] Theorem 7 for more details. This theory is translated to battery pack state estimation next.

4.7 Interval Observer for Batteries

In this section, the interval observer design introduced in Section 4.6 is applied to the Li-ion battery state estimation problem. Two scenarios are examined – (i) a single battery cell with temperature and SOC-dependent electrical parameters; (ii) electrically and thermally coupled cells in parallel, with SOC and temperature-dependent electrical parameters.

Single Battery Cell

It is hereby assumed that the input current, terminal voltage and surface temperature of the k-th single cell are experimentally measured. Ideally, a deterministic state observer could be proposed for the state estimation of the coupled nonlinear electrical-thermal system (4.46)-(4.53). However, this approach is intractable due to the system nonlinearities like electrical-thermal coupling, state-dependent parameters and voltage output function. To tackle this issue, the electrical parameters' dependence on the internal states is suppressed, and we treat these parameters as uncertain. Specifically, $\theta \in \Theta \subset \mathbb{R}^4$, where $\theta = \begin{bmatrix} R_{1,k} & R_{2,k} & C_k & Q_k \end{bmatrix}^\top$. The objective is to design a robust interval observer, using the measurements, to determine the set of admissible values for cell SOC at each time instant, when the plant model is subject to bounded uncertainties in the parameters and states' initial conditions.

Let $\tau_k = 1/(R_{2,k}C_k)$, and consider a known nominal value $\tau_{k,0}$ such that $\tau_k = \tau_{k,0} + \delta\tau_k$, where $\tau_{k,0}$ is a deterministic scalar and $\delta\tau_k$ represents the uncertain component. The single cell electrical system (4.46)-(4.48) can thus be formulated in terms of uncertain system (4.59)-(4.60), with

$$x = \begin{bmatrix} x_1 \\ x_2 \end{bmatrix} = \begin{bmatrix} z_k \\ V_{c,k} \end{bmatrix},\ f(x) = \begin{bmatrix} 0 \\ -\tau_{k,0}x_2 \end{bmatrix}, \delta f(x,\theta) = \begin{bmatrix} 0 \\ -\delta\tau_k x_2 \end{bmatrix},\ B(\theta) = \begin{bmatrix} \frac{1}{Q_k} \\ \frac{1}{C_k} \end{bmatrix},\ u = I_k(t),$$
$$h(x) = OCV(x_1) + x_2,\ \delta h(\theta) = R_{1,k}. \tag{4.74}$$

It is assumed that the following upper and lower bounds are imposed on the uncertain parameters:

$$R_{1,k} \in \left[\underline{R}_{1,k}, \overline{R}_{1,k}\right], \quad \delta\tau_k \in \left[\underline{\delta\tau}, \overline{\delta\tau}\right], \quad C_k \in \left[\underline{C}, \overline{C}\right], \quad Q_k \in \left[\underline{Q}, \overline{Q}\right], \tag{4.75}$$

so that Θ is a four-dimensional polytope. These bounds might be found in practice through parameter identification of the weakest and strongest cells in the pack. The local observability matrix for the nominal system is then given by

$$\mathcal{O}(x) = \begin{bmatrix} \mathrm{d}h(x) \\ \mathrm{d}L_f h(x) \end{bmatrix} = \begin{bmatrix} \frac{\mathrm{d}OCV}{\mathrm{d}x_1}(x_1) & 1 \\ 0 & -\tau_{k,0} \end{bmatrix}, \tag{4.76}$$

whose rank is 2 if and only if the first derivative of the OCV function with respect to SOC is non-zero around an equilibrium point $x_1 = x_{1,e}$ and $\tau_{k,0} \neq 0$, i.e.

$$\frac{\mathrm{d}OCV}{\mathrm{d}x_1}(x_{1,e}) \neq 0, \quad \tau_{k,0} \neq 0, \tag{4.77}$$

which aligns with existing results on local observability for battery models [125]. Hence, the coordinate transformation based on Lie algebra

$$\Phi(x) = \begin{bmatrix} \xi_1(x) \\ \xi_2(x) \end{bmatrix} = \begin{bmatrix} OCV(x_1) + x_2 \\ -\tau_{k,0}x_2 \end{bmatrix} \tag{4.78}$$

transforms the system (4.59), (4.60), with (4.74) to the nonlinear parameter-varying system (4.65)-(4.66), with

$$A_0 = \begin{bmatrix} 0 & 1 \\ 0 & -\tau_{k,0} \end{bmatrix},\ \delta A(\theta) = \begin{bmatrix} 0 & \frac{\delta\tau_k}{\tau_{k,0}} \\ 0 & -\delta\tau_k \end{bmatrix},\ H = \begin{bmatrix} 1 & 0 \end{bmatrix},\ b(\xi,\theta) = \begin{bmatrix} \frac{1}{Q_k}\varphi\big(\xi_1 + \frac{1}{\tau_{k,0}}\xi_2\big) + \frac{1}{C_k} \\ -\frac{\tau_{k,0}}{C_k} \end{bmatrix} I, \tag{4.79}$$

where

$$\varphi(\cdot) = \frac{\mathrm{d}OCV}{\mathrm{d}x}\left(OCV^{-1}(\cdot)\right). \tag{4.80}$$

An interval observer can be designed based on (4.69)-(4.70) and Theorem 9. The bounding functions $\overline{\delta A}$ and $\underline{\delta A}$ for δA can be readily obtained by applying the parameter bounds. The bounding functions $\overline{b}(t)$ and $\underline{b}(t)$ are carefully evaluated according to the direction of current $I(t)$ for all t.

Battery Cells in Parallel

As opposed to having one interval observer for a single cell in the preceding discussion, the proposed design is generalized for a cluster of battery cells in parallel. One practical advantage for using an interval observer for a group of cells is its scalabilty. An interval observer, composed of only two dynamical systems estimating upper and lower bounds that all trajectories of unknown states live in, significantly reduces computation and design effort. Due to cell heterogeneity, an interval observer constructs two trajectories that upper and lower bound all SOC trajectories, without dealing with the differential-algebraic nature of the circuit dynamics.

The interval observer design for parallel cells inherits the essence of the design for single cells. The only difference is to compute a single set of bounding functions that bound uncertainties from all cell in the parallel configuration.

Remark 14. *A crucial step in designing interval observers for cells in parallel is to find the bounding functions for the uncertainties. Namely, the bounding functions are closely associated with the instantaneous bounds on the local currents. Unlike the single cell scenario, the local currents of parallel cells are not available for measurement. In this work, it is assumed that appropriate bounds on the local currents are given.*

Remark 15. *The width/tightness of the estimated intervals is dependent on the magnitude of model uncertainties, and our knowledge of the uncertainties when defining the bounding functions.*

4.8 Simulation Studies

In this section, we illustrate the performance of i) the observer for the nonlinear descriptor system, and ii) the interval observer.

Observer for Parallel Cells via A Descriptor System

A simulation study using a battery block with $n = 2$ NMC cells connected in parallel is conducted to evaluate the performance of the proposed estimation scheme. Without loss of generality, a pair of cells is preferred over a larger block to facilitate the presentation of results. Consider the situation in which the cells may differ in their initial SOCs and model parameters, but subject to the same SOC-OCV relationship. The considered setup guarantees local observability based on the analysis in Chapter 4.3.

The model parameters and initial SOCs are shown in Table 4.1. Under these circumstances, the state vector is given by

$$w = \begin{bmatrix} z_1 & V_{c,1} & z_2 & V_{c,2} & I_1 & I_2 \end{bmatrix}^\top \in \mathbb{R}^6. \tag{4.81}$$

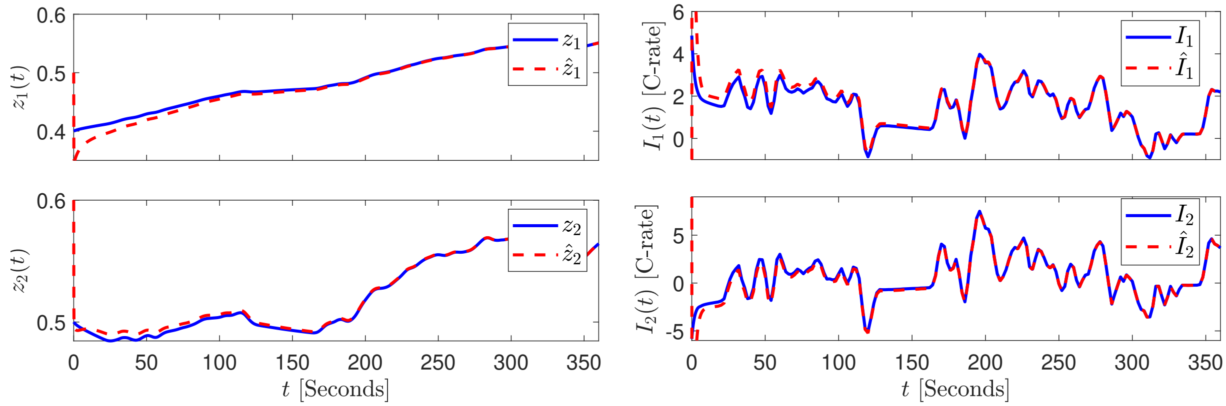

Figure 4.4: **Left:** The estimation performance for SOCs of a two-cell parallel configuration. **Right:** The estimation performance for local currents of a two-cell parallel configuration. The results verify the asymptotic convergence.

Table 4.1: Model Parameters in Simulation Study

	Cell 1	Cell 2	Units
$R_{1,k}$	0.0025	0.0015	[Ω]
$R_{2,k}$	0.004	0.0035	[Ω]
C_k	1500	2000	[F]
Q_k	2.3	2.0	[Ah]
z_0	0.4	0.5	[–]

In this simulation study, the total applied current comes from a UDDS drive cycle provided in Fig. 4.3(a) with appropriate scaling. The observer in (4.32)-(4.33) is used to estimate the individual cell SOCs and the local currents by using only the voltage and overall current measurements. The initial SOC errors between the plant model and the observer are 15% and 10%, respectively. The observer gain is chosen to be $L = [-30\ \ -30\ \ -20\ \ 2\ \ 4\ \ -20]^\top$, which satisfies the conditions of Theorem 7.

Figs. 4.4 demonstrates the estimation performance, where the solid blue curves are the true states (differential and algebraic) from the plant model and the dashed red curves are the estimated ones. The left plots in Fig. 4.4 displays the estimates for the differential states (SOCs), whereas the right ones portray the estimates for the algebraic states (local currents). The state observer is able to recover the true signals quickly (in approximately 100 seconds) from large initial estimation errors. These results confirm the asymptotic zero error convergence conclusions in Theorem 7.

Interval Observer for Parallel Cells

In order to validate the interval observer design, numerical studies are carried out on NMC battery cells modeled with a lumped electrical-thermal model (4.46)-(4.6). The state-dependent electrical model parameters are taken from [11]. The total current fed to the battery is a UDDS driving cycle. The interval observer from Theorem 9 is used to estimate the bounds on the internal states from only total current and voltage measurements. Two scenarios are considered. First, the state estimation of a single battery cell is tested, which accounts for uncertainties linked to state dependent parameters. Then, the same observer is used to estimate the state interval for a parallel arrangement of five cells, which involves uncertainty due to cell heterogeneity as well as SOC and temperature dependent parameters.

Interval Observer for Single Battery Cell

Let us first consider a single cell and design the interval observer according to Section 4.7. The initial value for SOC in the plant model is 30%, and the initial values on the interval observers (lower and upper bounds) are 20% and 40%. The observer gains are chosen to be $\underline{L} = [10 \quad -0.1]^\top$ and $\overline{L} = [10 \quad -0.1]^\top$, which ensure that $(A_0 - \underline{L}H)$ and $(A_0 - \overline{L}H)$ are Metzler and Hurwitz. The black signal in Fig. 4.5(a) shows the applied current. The solid black curve in Fig. 4.5(b) is the plant model simulated SOC, and the shaded green region represents feasible SOC values between the estimated intervals. From these plots, the interval observer recovers quickly (less than 20 s) from large initial errors and always enclose the true SOC of the battery. These results confirm the stability and inclusion properties of the designed interval observer stated in Theorem 9, given uncertain initial conditions and state-dependent parameters.

Interval Observer for Battery Cells in Parallel

Let us now consider a parallel arrangement of five cells, which differ in their initial SOCs and model parameters. The interval observer is designed according to 4.7. The initial SOCs are 20%, 30%, 34%, 37%, and 49%, and the initial bounds (interval observer) on SOCs are 15% and 54%. The applied total current is given by the orange signal in Fig. 4.5(a). In Fig. 4.5(c), the solid curves represent the true SOC of each cell, and the shaded green area highlights the feasible SOC values for all cells between the estimated intervals. These plots show that the interval observer is close to the minimum and maximum states during its temporal evolution. It also envelops the state distribution across the five cells. Hence, the results show that cell heterogeneity can be included as unknown but bounded uncertainties, which is exploited to develop an interval observer that provides reliable bound estimates for the states. Moreover, stability and inclusion of the observer are guaranteed by Theorem 9.

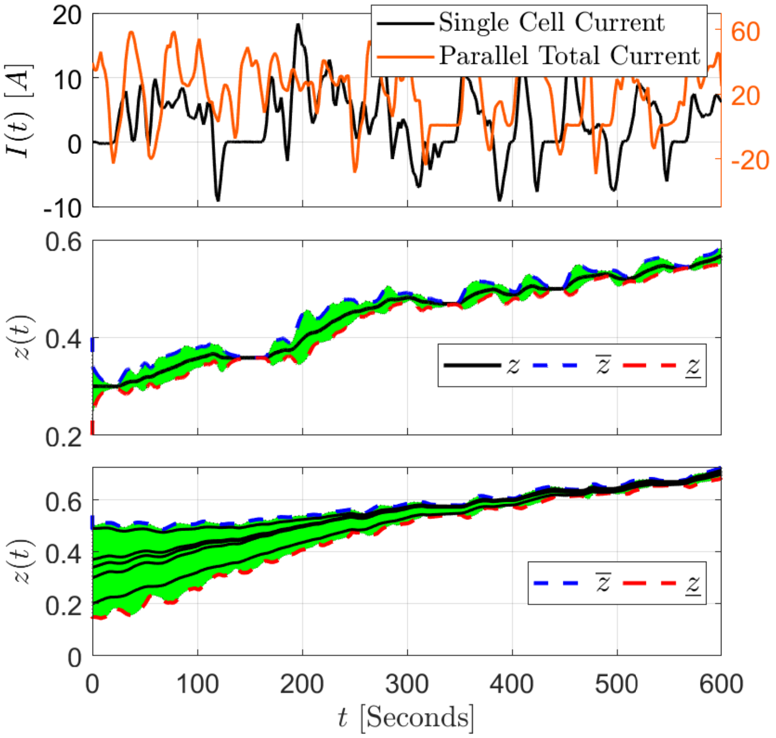

Figure 4.5: The interval observer bounds enclose the true states of charge for (b) a single cell and (c) five cells in parallel.

4.9 Conclusion

The state estimation problem for battery cells in parallel has been overlooked due to multiple unrealistic assumptions. We demonstrate heterogeneity between cells when connected in parallel. A nonlinear descriptor system has been proposed to model parallel arrangements of lithium-ion battery cells, and a state observer for such systems has been developed. This modeling framework fits naturally with battery applications, given the interconnections arising from Kirchhoff's laws. The design procedure used to build the state observer from this model avoids linearization or canonical transformations, and it only relies on the assumption of Lipschitz nonlinearities. The resulting state observer benefits from considering the cell currents as algebraic states to be simultaneously estimated with the differential states.

Secondly, an interval observer based on an equivalent circuit-thermal model for lithium-ion batteries has been presented in this paper. The SOC-temperature-dependent parameters are considered as unknown but bounded uncertainties. Then, a parallel arrangement of five cells is used for observer design, where cell heterogeneity is now accounted for through the uncertainty bounding functions. Given that the nominal battery model is locally observable, the original uncertain model can be transformed into a partial-linear form, which enables interval estimation based on monotone systems. By properly choosing the observer gains, the state matrix of the estimation error is Hurwitz and Metzler, which guarantees stability and inclusion of the state bound estimates. A major feature of the proposed estimation approach is its scalability, since the number of states of interval observers is independent of the number of cells in a pack. Simulation showcases the effectiveness of i) the descriptor system based cell state (differential and algebraic) estimator, and ii) the interval observer design. Future work includes developing a systematic methodology for computing the bounding functions associated with unknown local currents, and potential extended studies of control/stabilization problems utilizing the estimated state intervals [126, 127].

Chapter 5

Battery Temperature Estimation with an Uncertain Semilinear PDE Model

As batteries insert themselves more and more into our society, their operation is becoming increasingly safety critical, meaning that any battery failure can have an increasingly important impact upon systems of increasing size. One of the existing challenges that substantially impacts the battery safety and performance is its thermal behavior. In particular, many cases of thermal runaways leading to fire and explosion of Li-ion battery have been previously reported in [9]. As well as safety issues, thermal effects have also been shown to be key factors in the rate of battery degradation [10, 128]. Hence, in order to improve battery safety and longevity, it is crucial to develop thermal management strategies to alleviate the effects of temperature and prevent the drastic failure of the battery from happening. In light of the above concerns, this chapter proposes a model-based estimation algorithm for the battery temperature based on a high-fidelity nonlinear distributed parameter thermal model. As well as addressing this important application, the observer developed in this work is one of the first designed for a nonlinear parabolic partial differential equation (PDE) state estimation problem without performing linearization and spatial discretization prior to the observer design.

Modeling of battery thermal performance has been extensively studied in the literature [129]. Comprehensive high-dimensional thermal models, e.g., [130, 131, 132], provide an accurate and thorough understanding of the cell temperature behavior from an electrochemical point of view. Nevertheless, since these high-dimensional models are too complicated and demand a great amount of computational power, their application to real-time estimation and control in a battery management system (BMS) will not be feasible for applications outside of industrial/stationary storage [133]. To balance physical relevance and model structural simplicity, reduced-order PDE thermal models have been proposed [134, 135, 136]. A few other finite-dimensional approaches for battery thermal modeling stand out, and one such model is a two-state thermal model that predicts the surface and core temperature of a cylindrical battery cell [27]. A lumped thermal model has also been proposed by Smith et al. in [137]. Note that battery thermal behavior exhibits certain nonlinearity that are originated from ressistive heat generation, reversible entropic heat, and enthalpy of reactions, etc.

Catastrophic thermal failures stimulate significant work on the development of next-generation thermal estimation schemes. Previous studies on battery state estimation can be categorized into two main groups, i.e., the equivalent circuit model-based estimation [138, 139, 47, 18], and the electrochemical model-based estimation [45, 43, 140, 141, 68]. The existing BMS generally uses a thermal sensor attached to the surface of the cell and employ the online measured surface temperature for estimation. In [20], an adaptive observer for battery core temperature estimation was designed for a two-state thermal model with surface measurements. As well as estimation, studies on thermal fault diagnosis, e.g., the detection and isolation of the faults that influence the surface and core temperature in the two-state thermal model [133] and a PDE observer based fault detection [142], have also demonstrated benefits. A dual Kalman filter based temperature distribution estimation for cylindrical batteries under unknown cooling, based on a reduced radially distributed one-dimensional thermal modeling, was proposed in [143]. The work in [144] introduces an internal temperature distribution estimation in cylindrical cells by combining measured electrochemical impedance and surface temperature, relying on a combined thermal-impedance model. However, these methodologies suffer from one or more of the following drawbacks: (i) Early lumping approaches, where the thermal PDE models are discretized and approximated by systems of ordinary differential equations (ODE) a priori, are used to design the observers. This leads to the loss of PDE model accuracy and the state estimates from the discretized systems may not always converge to the true states. (ii) Only a small portion of these works provide theoretically certified convergence properties for the proposed estimation scheme. (iii) Finally, most of these works do not consider the inherent nonlinearity of battery thermal model. In this chapter, we attempt to address these drawbacks by proposing an estimation scheme that designs an observer directly on nonlinear battery PDE thermal model, i.e., using late lumping, and provide theoretical guarantee of estimation error convergence.

From a theoretical viewpoint, methods for control/estimation of linear parabolic PDEs based on the late-lumping approach have been well studied. The stabilization of unstable heat equations using boundary observation was addressed in [145] by means of an auxiliary functional observer. Smyshlyaev et al. applied the backstepping method to controller design based on a model with space-dependent diffusivity or time-dependent reactivity [146]. The authors in [66] presented an adaptive boundary observer for parabolic PDEs with domain and boundary parameter uncertainties, with the PDE being linear in the states and parameters. The techniques introduced in [65] provides a thorough analysis of the stability of adaptive control for linear parabolic PDEs with spatially varying coefficients. Nonetheless, extending these observer designs from linear to nonlinear PDE system require a more intricate analysis, with only a few designs having been developed so far. For instance, an extended Luenberger-type observer was proposed for a class of semilinear parabolic PDEs in [64]. The authors therein verified the exponential stability of the linearized observer error dynamics, in which the design extends the well-known backstepping method [147] to include the Volterra transformation with a time-varying kernel. A series of studies by Vazquez et al. discussed the control design for a 1-D parabolic PDE with Volterra nonlinearities [148, 149]. Boundary controller have also been designed towards Burgers' equation [150]. Additionally, designs based upon the plant models with modeling and parametric uncertainties, have also been explored. Cheng considers the stabilization of the heat equation with parameter variation and boundary uncertainties by designing a sliding mode controller [151]. Parabolic PDEs that are subject to in-domain and boundary parameter uncertainties are examined in [66]. However, none of the aforementioned works discuss observer design for nonlinear parabolic PDE systems simultaneously subjected to Lipschitz nonlinearity and model uncertainties.

In this context, we advance the aforementioned work by proposing a PDE-based observer for a one-dimensional distributed parameter thermal model subject to in-domain and output uncertainties, with the measurements from the cell surface. The thermal behavior for a Li-ion battery cell can be described by a semilinear parabolic PDE with Robin boundary condition, provided mild assumption on the nonlinear in-domain heat generation. The design is unique, since it exploits fundamental thermal dynamic properties. In addition, we rigorously prove the stability of the estimation error dynamics.

The remainder of the chapter is organized as follows. Chapter 5.1 formulates the one-dimensional semilinear thermal PDE model with nonlinear Lipschitz continuous heat generation. Chapter 5.2 presents the state estimation scheme based on the aforementioned model without the in-domain and output uncertainties, and the corresponding stability analysis of the estimation error dynamics. Chapter 5.3 proposes the strategies for observer gain selection. Chapter 5.4 develops a robust state estimation for the plant model with in-domain and output uncertainties. The performance of the observers is demonstrated via simulations in Chapter 5.5. The conclusions and future works are discussed in Chapter 5.6.

Notation. Throughout this chapter, $T(x,t)$ denotes the plant's state variable, which depends on nondimensionalized space x and time t. The x and t subscripts represent partial derivatives with respect to the notated variable: $u_t = \partial u/\partial t$, $u_x = \partial u/\partial x$, and $u_{xx} = \partial^2 u/\partial x^2$. The dot symbol denotes derivative with respect to time t, e.g. $\dot{\nu} = \mathrm{d}\nu/\mathrm{d}t$. The spatial L_2 norm is defined as

$$\|T(\cdot,t)\| = \sqrt{\int_0^1 T^2(x,t)\mathrm{d}x}.$$

5.1 Distributed Parameter Thermal Model

This section presents the development of a one-dimensional nonlinear PDE thermal model for batteries, oriented towards state estimation design.

One-dimensional Thermal Model

An unsteady non-homogeneous heat equation can be employed to describe the temperature distribution over the three-dimensional region for a prismatic battery cell shown in Fig. 5.1

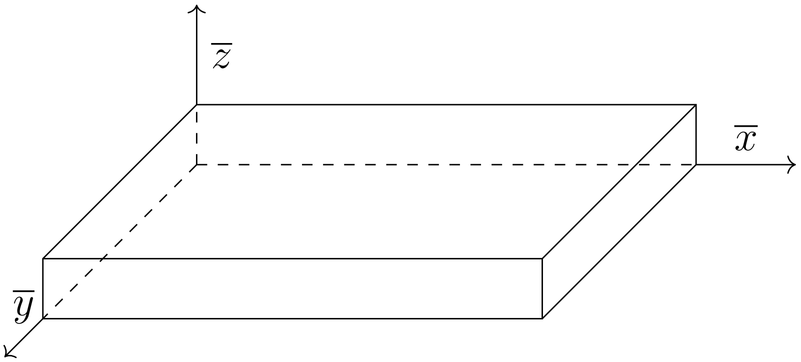

Figure 5.1: A schematic of a prismatic cell. The length in $\overline{z}$ dimension is typically much smaller than the dimensions in $\overline{x}$ and $\overline{y}$ dimensions.

[152]:

$$\rho c_p \frac{\partial \overline{T}}{\partial \overline{t}} = k_{\overline{x}} \frac{\partial^2 \overline{T}}{\partial \overline{x}^2} + k_{\overline{y}} \frac{\partial^2 \overline{T}}{\partial \overline{y}^2} + k_{\overline{z}} \frac{\partial^2 \overline{T}}{\partial \overline{z}^2} + \dot{q}, \tag{5.1}$$

where $\overline{T} = \overline{T}(\overline{x}, \overline{y}, \overline{z}, \overline{t})$ and $\dot{q} = \dot{q}(\overline{x}, \overline{y}, \overline{z}, \overline{t})$. Symbol $\overline{T}$ is the battery distributed temperature with respect to spatial position and time, and $\dot{q}$ denotes the volumetric heat generation rate. Moreover, k_i, $i \in \{\overline{x}, \overline{y}, \overline{z}\}$, is the thermal conductivity, ρ represents density, and c_p is the specific heat. The length $L_{\overline{z}}$ in the $\overline{z}$–dimension is typically much smaller than the dimensions in $\overline{x}$– and $\overline{y}$–dimensions, i.e. $L_{\overline{x}}$ and $L_{\overline{y}}$. Since prismatic Li-ion cells are composed by layers of anode, cathode, and separator materials, in the $\overline{x}$–$\overline{y}$ plane the thermal conductivity is dominated by the high conductivity of metals, whereas in the $\overline{z}$–dimension the conductivity is limited by the stacked layers and high thermal contact resistances. Thus, the thermal conductivity in the $\overline{x}$– and $\overline{y}$–dimensions are much larger than those in the $\overline{z}$–dimension, i.e. $k_{\overline{x}} \approx k_{\overline{y}} \gg k_{\overline{z}}$. Define τ_i to be the characteristic diffusion time in the i–dimension, where $i \in \{\overline{x}, \overline{y}, \overline{z}\}$:

$$\tau_i = \frac{L_i^2}{D_i} = \rho c_p \frac{L_i^2}{k_i}, \tag{5.2}$$

where D_i is the heat diffusion coefficient. As a numerical example, let $L_{\overline{x}} = 0.216$m, $L_{\overline{y}} = 0.129$m, $L_{\overline{z}} = 0.0072$m, $k_{\overline{x}} = k_{\overline{y}} = 28$W/(m·K), and $k_{\overline{z}} = 1.5$W/(m·K) [136, 153]. This leads to $\tau_{\overline{x}} \approx 48\tau_{\overline{z}}$ and $\tau_{\overline{y}} \approx 17\tau_{\overline{z}}$. The heat diffusion in the $\overline{z}$–dimension can thus be treated as instantaneous relative to those in $\overline{x}$- and $\overline{y}$–dimension.

Assumption 3. *The characteristic diffusion time in the $\overline{x}$–dimension is much larger than that in the $\overline{y}$–dimension, i.e. $\tau_{\overline{x}} \gg \tau_{\overline{y}}$.*

Although the above numerical example indicates that, with the specific cell geometry and cell material used, $\tau_{\overline{x}} \approx 3\tau_{\overline{y}}$, the Assumption 3 allows the original high-dimensional heat diffusion process (5.1) to be approximated by a reduced-order one-dimensional heat diffusion equation in the $\overline{x}$–dimension. An investigation of a two-dimensional (in $\overline{x}$–$\overline{y}$ plane) model is expected in future works. Therefore, a one-dimensional heat diffusion model has been elected in this study to describe the dynamics of the temperature distribution:

$$\frac{1}{\sigma}\frac{\partial \overline{T}}{\partial \overline{t}}\left(\overline{x},\overline{t}\right) = \frac{\partial^2 \overline{T}}{\partial \overline{x}^2}\left(\overline{x},\overline{t}\right) + \frac{\dot{q}\left(\overline{x},\overline{t}\right)}{k_{\overline{x}}}, \tag{5.3}$$

where $\sigma = \rho c_p / k_{\overline{x}}$, with Robin boundary conditions

$$\frac{\partial \overline{T}}{\partial \overline{x}}(0,\overline{t}) = \frac{h_{\overline{x}}}{k_{\overline{x}}}\left(\overline{T}_\infty - \overline{T}(0,\overline{t})\right), \tag{5.4}$$

$$\frac{\partial \overline{T}}{\partial \overline{x}}(L_{\overline{x}},\overline{t}) = \frac{h_{\overline{x}}}{k_{\overline{x}}}\left(\overline{T}_\infty - \overline{T}(L_{\overline{x}},\overline{t})\right), \tag{5.5}$$

where $\overline{x} \in [0, L_{\overline{x}}]$ is the spatial coordinate and $\overline{t} \in \mathbb{R}^+$ denotes time. $\overline{T}_\infty$ represents the constant ambient temperature. Symbol $h_{\overline{x}}$ is the convective heat transfer coefficient in $\overline{x}$–dimension. The temperatures at both boundaries can be measured by physical sensors, as follows

$$\overline{y}_m\left(\overline{t}\right) = \left[\overline{T}\left(0,\overline{t}\right), \overline{T}\left(L_{\overline{x}},\overline{t}\right)\right]. \tag{5.6}$$

Model Reduction and Analysis

Next we perform normalization and coordinate transformation to simplify the mathematical structure of the distributed parameter thermal model (5.3)-(5.6). Scale the position $\overline{x}$ and time $\overline{t}$ coordinates as follows,

$$x = \frac{\overline{x}}{L_{\overline{x}}}, \quad t = \frac{\alpha \overline{t}}{L_{\overline{x}}^2}, \quad k = \frac{k_{\overline{x}}}{L_{\overline{x}}^2}, \quad h = \frac{h_{\overline{x}}}{L_{\overline{x}}}, \quad T(x,t) = \overline{T}(\overline{x},\overline{t}), \quad \dot{Q}(x,t) = \dot{q}\left(\overline{x},\overline{t}\right), \tag{5.7}$$

where x and t are dimensionless. The above coordinate transformation yields

$$\frac{\partial T}{\partial t}(x,t) = \frac{\partial^2 T}{\partial x^2}(x,t) + \frac{\dot{Q}(x,t)}{k}, \tag{5.8}$$

with Robin boundary conditions

$$\frac{\partial T}{\partial x}(0,t) = \frac{h}{k}(T_\infty - T(0,t)), \tag{5.9}$$

$$\frac{\partial T}{\partial x}(1,t) = \frac{h}{k}(T_\infty - T(1,t)), \tag{5.10}$$

where $x \in [0,1]$ and $t \in \mathbb{R}^+$. The measurement signals in the transformed coordinate become

$$y_m(t) = \left[T(0,t), T(1,t)\right]. \tag{5.11}$$

The equation for computing heat generation proposed by Bernardi et al. [154] is employed frequently in its simplified form,

$$\dot{Q}(x,t) = I^2(t)\frac{R_s\big(T(x,t), SOC(t)\big)}{V} - I(t)T(x,t)\frac{\mathrm{d}V_{oc}}{\mathrm{d}T}, \tag{5.12}$$

where $I(t)$ is the applied current, V_{oc} denotes the open circuit voltage, and $V = L_{\overline{x}}L_{\overline{y}}L_{\overline{z}}$ represents the volume of the battery cell. Symbol R_s stands for the lumped resistance distributed over the spatial and time domain and is generally dependent on temperature and state of charge (SOC) of the battery cell [155]. The term $R_s\big(T(x,t), SOC(t)\big)$ can be characterized experimentally, e.g., see Fig. 6 in [155] for an illustrative example. For the heat generation expression in (5.12),

- The first term is the heat generation from resistive dissipation, which is always positive.
- The second term is the reversible entropic heat. The term $\frac{\mathrm{d}V_{oc}}{\mathrm{d}T}$ varies with SOC and can be determined by offline experimental studies, e.g., [28].

Remark 16. *As noted in [156, 157], with fixed SOC, the behavior of R_s due to the variation in temperature should nearly follow an Arrhenius type relationship:*

$$R_s(T) = R_s(T_0)\exp\left[-\frac{E_a}{R}\left(\frac{1}{T_0} - \frac{1}{T}\right)\right], \tag{5.13}$$

where T_0 is a given reference temperature, E_a is the activation energy, and R denotes the gas constant. Observe that

$$\frac{\mathrm{d}R_s}{\mathrm{d}T}(T) = -R_s(T_0)\frac{E_a}{RT^2}\exp\left[-\frac{E_a}{R}\left(\frac{1}{T_0} - \frac{1}{T}\right)\right] \tag{5.14}$$

is a monotonically increasing function with respect to T when $T > T_c = -E_a/2R$. Numerically, the admissible temperature range for a Li-ion battery cell is significantly larger than T_c.

In this work, for the purpose of model simplicity and observer design, the heat generation formulation (5.12) is reduced by (i) ignoring the entropic heat generation in the subsequent discussion as the entropic coefficient is significantly small for certain types of batteries, e.g., Lithium-ion Phosphate cell, and (ii) suppressing the dependence of R_s on SOC, and only taking into account the temperature dependence, e.g., $R_s = R_s(T(x,t))$. Consequently, the modeling error from the reduction is compensated by a distributed uncertainty $\delta(x,t)$, i.e.,

$$\dot{Q}(x,t) = I^2(t)\frac{R_s\big(T(x,t)\big)}{V} + \delta(x,t), \tag{5.15}$$

where $\delta(x,t)$ is upper and lower bounded, and these bounds can be numerically retrieved by experiments.

Hence, subbing this reduced heat generation (5.15) into (5.8) gives the final plant model under consideration in this study:

$$\frac{\partial T}{\partial t}(x,t) = \frac{\partial^2 T}{\partial x^2}(x,t) + f\left(T(x,t)\right) + \varepsilon(x,t), \tag{5.16}$$

where $\varepsilon(x,t) = \delta(x,t)/k$ and

$$f(T(x,t)) = \frac{1}{kV} I^2(t) R_s(T(x,t)), \tag{5.17}$$

with R_s given by (5.13), and Robin boundary conditions

$$\frac{\partial T}{\partial x}(0,t) = \frac{h}{k}(T_\infty - T(0,t)), \tag{5.18}$$

$$\frac{\partial T}{\partial x}(1,t) = \frac{h}{k}(T_\infty - T(1,t)). \tag{5.19}$$

The initial condition of the plant model is

$$T(x,0) = T_0(x). \tag{5.20}$$

The temperature signals at both boundaries are experimentally measured,

$$y_0(t) = T(0,t) + \mu(t), \quad y_1(t) = T(1,t) + \nu(t), \tag{5.21}$$

where we impose disturbances $\mu(t)$ and $\nu(t)$ in the output equations to account for uncertainties from the ambient environment or sensor inaccuracies. Let $\mathcal{U} = L_2(0,1)$ denote the state space of $T(x,t)$.

Assumption 4. *$f(T)$ is $\mathcal{C}^1$ in T, for all $x \in [0,1]$, $t \in [0,\infty)$, and $T \in \mathcal{U}$.*

Theorem 10 (Lipschitz Continuity)**.** *The nonlinearity $f(T(x,t))$ is globally Lipschitz continuous in $T(x,t)$, i.e., for every $T_1, T_2 \in \mathcal{U}$, there exists a positive constant γ such that*

$$\left\| f\left(T_1(\cdot,t)\right) - f\left(T_2(\cdot,t)\right) \right\| \leq \gamma \left\| T_1(\cdot,t) - T_2(\cdot,t) \right\|. \tag{5.22}$$

Proof. A Lipschitz constant with respect to T can be obtained by computing the infinity norm of $\mathrm{d}R_s/\mathrm{d}T$ per Remark 16,

$$\gamma = \frac{1}{kV}|I|^2_{\max} \left| \frac{\mathrm{d}R_s}{\mathrm{d}T}(T) \right|_{\max} = \frac{1}{kV}|I|^2_{\max} R_s(T_0) \frac{E_a}{RT^2_{\min}} \exp\left[-\frac{E_a}{R}\left(\frac{1}{T_0} - \frac{1}{T_{\min}} \right) \right]. \tag{5.23}$$

where $|I|_{\max}$ is the maximum absolute value of the applied current $I(t)$, and $T_{\min}$ is the minimum temperature allowed by the application. ■

Theorem 11. *According to [64, 158], Assumption 4 and Theorem 10 ensure the existence and uniqueness of a mild solution to the PDE system (5.16)-(5.20).*

Assumption 5. *The in-domain uncertainty $\varepsilon(x,t)$ is finite and bounded by $\varepsilon(x,t) \leq \overline{\varepsilon}$, $\forall(x,t) \in [0,1] \times [0,\infty)$, where $\overline{\varepsilon} \geq 0$.*

Assumption 6. *The uncertainties $\mu(t)$ and $\nu(t)$ in the output equations are finite and bounded by $\mu(t) \leq \overline{\mu}$, $\nu(t) \leq \overline{\nu}$, $\forall t \in [0,\infty)$, where $\overline{\mu}, \overline{\nu} \geq 0$. We further assume that $\mu(t)$ and $\nu(t)$ are continuously differentiable with respect to time t.*

Our objective is to estimate the spatially distributed temperature $T(x,t)$ in PDE (5.16) by utilizing only the boundary measurements $y_0(t)$ and $y_1(t)$. In Section 5.2, we present the observer design and observer convergence analysis based on the uncertainty-free plant model, i.e. $\varepsilon(x,t) = 0$, $\mu(t) = 0$, and $\nu(t) = 0$, $\forall x \in [0,1]$ and $t \in [0,\infty)$. Furthermore, in Section 5.4, we provide robust estimation scheme based on the plant model with uncertainties, i.e. $\varepsilon(x,t) \neq 0$, $\mu(t) \neq 0$, and $\nu(t) \neq 0$, in the sense of minimizing the estimation error via optimal observer gain selection.

Remark 17. *Although the considered problem setup is for prismatic cells, the method presented here can be easily generalized to cylindrical cells. Specifically, suppose the cell is thermally homogeneous, a distributed thermal dynamics for a cylindrical cell can be expressed as [134]*

$$\frac{1}{\alpha}\frac{\partial T}{\partial t}(r,t) = \frac{\partial^2 T}{\partial r^2}(r,t) + \frac{1}{r}\frac{\partial T}{\partial r}(r,t) + \frac{\dot{Q}(r,t)}{k}, \tag{5.24}$$

$$\frac{\partial T}{\partial r}(0,t) = 0, \tag{5.25}$$

$$\frac{\partial T}{\partial r}(R_p,t) = \frac{h}{k}\left(T_\infty - T(R_p,t)\right), \tag{5.26}$$

$$y_m(t) = T(R_p,t), \tag{5.27}$$

where R_p denotes the radius and $r \in [0,R_p]$ is the radial coordinate. Performing a normalization and transforming from spherical coordinate to Cartesian coordinate yields a similar structure to system (5.8)-(5.11).

5.2 State Estimation for Uncertainty-Free Plant Model

In this section, the following uncertainty-free plant model, namely $\varepsilon(x,t)=0$, $\mu(t)=0$, and $\nu(t)=0$, $\forall x\in[0,1]$ and $t\in[0,\infty)$, is considered:

$$T_t(x,t)=T_{xx}(x,t)+f(T(x,t)), \tag{5.28}$$

$$T_x(0,t)=\frac{h}{k}(T_\infty-T(0,t)), \tag{5.29}$$

$$T_x(1,t)=\frac{h}{k}(T_\infty-T(1,t)), \tag{5.30}$$

$$T(x,0)=T_0(x), \tag{5.31}$$

$$y_0(t)=T(0,t), \tag{5.32}$$

$$y_1(t)=T(1,t). \tag{5.33}$$

State Observer Structure

A distributed parameter state observer is designed by using a copy of the plant model with error injection, i.e.,

$$\widehat{T}_t(x,t)=\widehat{T}_{xx}(x,t)+f\left(\widehat{T}(x,t)\right)+p_1(x)\left(y_1(t)-\widehat{T}(1,t)\right), \tag{5.34}$$

$$\widehat{T}_x(0,t)=\frac{h}{k}(T_\infty-y_0(t)), \tag{5.35}$$

$$\widehat{T}_x(1,t)=\frac{h}{k}\left(T_\infty-\widehat{T}(1,t)\right)+p_{10}\left(y_1(t)-\widehat{T}(1,t)\right), \tag{5.36}$$

where $\widehat{T}(x,t)$ stands for the estimation of $T(x,t)$, and $\widehat{T}(1,t)$ is the boundary state estimate. Symbols $p_1(x)$ and p_{10} are spatially varying and constant observer gains to be designed to guarantee the stability of the observer error $\widetilde{T}(x,t)=T(x,t)-\widehat{T}(x,t)$. The initial condition for the observer is

$$\widehat{T}(x,0)=\widehat{T}_0(x). \tag{5.37}$$

Remark 18. *Despite the fact that the signals from both boundaries can be physically measured, only one of the boundary measurements are sufficient for the boundary observer design, which will be demonstrated subsequently in this section.*

Subtracting (5.34)-(5.37) from (5.28)-(5.31) yields the observer's error dynamics:

$$\widetilde{T}_t(x,t)=\widetilde{T}_{xx}(x,t)+\phi(x,t)-p_1(x)\widetilde{T}(1,t), \tag{5.38}$$

$$\widetilde{T}_x(0,t)=0, \tag{5.39}$$

$$\widetilde{T}_x(1,t)=-\left(\frac{h}{k}+p_{10}\right)\widetilde{T}(1,t), \tag{5.40}$$

$$\widetilde{T}(x,0)=T(x,0)-\widehat{T}(x,0), \tag{5.41}$$

where

$$\phi(x,t) = f\left(T(x,t)\right) - f\left(\widehat{T}(x,t)\right). \tag{5.42}$$

Remark 19. *Although the explicit dependence of $\phi(x,t)$ on $T(x,t)$ and $\widehat{T}(x,t)$ is suppressed in the notation above, this explicit dependence remains and is crucial in the subsequent stability analysis.*

Backstepping Transformation

To determine the appropriate observer gains, we adopt the backstepping approach [147]. We seek a linear backstepping transformation (*a.k.a.* a Volterra transformation) that transforms the state of the error system $\widetilde{T}(x,t)$ to a target state $\omega(x,t)$, by making use of the following expression with kernel function $j(x,y)$:

$$\widetilde{T}(x,t) = \omega(x,t) - \int_x^1 j(x,y)\omega(y,t)\mathrm{d}y, \tag{5.43}$$

which maps the error system (5.38)-(5.40) to the target system

$$\omega_t(x,t) = \omega_{xx}(x,t) + \psi(x,t) - c\omega(x,t), \tag{5.44}$$

$$\omega_x(0,t) = 0, \tag{5.45}$$

$$\omega_x(1,t) = -\left(c_1 + \frac{h}{k}\right)\omega(1,t), \tag{5.46}$$

where the constants $c > 0$ and c_1 are parameters to be designed. $\psi(x,t)$ is the transformed function from $\phi(x,t)$ by the same backstepping transformation, as follows,

$$\phi(x,t) = \psi(x,t) - \int_x^1 j(x,y)\psi(y,t)\mathrm{d}y. \tag{5.47}$$

To explicitly determine the kernel $j(x,y)$ we differentiate both sides of the transformation in (5.43) with respect to x and t and take into account target system (5.44)-(5.46). The computation reveals that the kernel $j(x,y)$ must satisfy the following Klein-Gordon PDE:

$$j_{xx}(x,y) - j_{yy}(x,y) = -cj(x,y), \tag{5.48}$$

$$j_x(0,y) = 0, \tag{5.49}$$

$$j(x,x) = -\frac{c}{2}x, \tag{5.50}$$

in which the boundary condition (5.49) emerges from evaluating (5.43) together with the boundary conditions (5.39)-(5.40). An unique and closed-form analytic solution exists for the PDE (5.48)-(5.50) [147, Chapter 4]:

$$j(x,y) = -cy\frac{I_1\left(\sqrt{c(y^2-x^2)}\right)}{\sqrt{c(y^2-x^2)}}, \tag{5.51}$$

where $I_1(\cdot)$ is the modified Bessel Function of the first kind. Moreover, the observer gains are computed as

$$p_1(x) = -j_y(x,1) - \left(c_1 + \frac{h}{k}\right) j(x,1), \tag{5.52}$$

$$p_{10} = c_1 - j(1,1) = c_1 + \frac{c}{2}. \tag{5.53}$$

Therefore, the observer gains (5.52)-(5.53) can be determined offline utilizing the kernel PDE solution (5.51).

Remark 20. *The fact that $\psi(x,t)$ is the transformed version of $\phi(x,t)$ under the same backstepping transformation makes the PDE system (5.48)-(5.50) for kernel function $j(x,y)$ to exhibit the same structure as the linear case, e.g., [147, Chapter 4]. The challenge lies in the stability verification of the target system.*

It is necessary to certify the existence and uniqueness of the inverse backstepping transformation, so that the stability of the target system implies the stability of the original error system. Consider the inverse backstepping transformation [147]:

$$\omega(x,t) = \widetilde{T}(x,t) + \int_x^1 \ell(x,y)\widetilde{T}(y,t)\mathrm{d}y, \tag{5.54}$$

with the kernel function $\ell(x,y)$. Similarly, differentiating both sides of the inverse backstepping transformation with respect to x and t yields the kernel PDE for $\ell(x,t)$:

$$\ell_{xx}(x,y) - \ell_{yy}(x,y) = c\ell(x,y), \tag{5.55}$$

$$\ell_x(0,y) = 0, \tag{5.56}$$

$$\ell(x,x) = -\frac{c}{2}x, \tag{5.57}$$

which has an analytic solution of

$$\ell(x,y) = -cy\frac{J_1\left(\sqrt{c(y^2-x^2)}\right)}{\sqrt{c(y^2-x^2)}}, \tag{5.58}$$

where $J_1(\cdot)$ is the Bessel Function of the first kind [147, Chapter 4].

Stability of the Target System

Based on the analysis in Section 5.2, the analytic solutions for the backstepping and inverse backstepping kernels $j(x,y)$ and $\ell(x,y)$ exist and are unique. Therefore, the stability properties of the target system (5.44)-(5.45) implies the stability of the original error system (5.38)-(5.40). In this section, we perform the Lyapunov analysis to establish the stability of the target system in the sense of spatial L_2 norm. We first present and prove the following lemma on Lipschitz continuity of the transformed nonlinearity ψ.

Lemma 12. *The nonlinear function $\psi(x,t)$ in the target system verifies the following inequality for all $t \in [0,\infty)$,*

$$\left\|\psi(\cdot,t)\right\| \leq \kappa(c;\gamma)\left\|\omega(\cdot,t)\right\|, \tag{5.59}$$

with $\kappa(c;\gamma) \coloneqq \gamma(1+\rho(c))(1+\eta(c))$, where

$$\rho(c) \coloneqq \sqrt{\int_0^1 \int_x^1 \ell^2(x,y;c)\mathrm{d}y\mathrm{d}x}, \tag{5.60}$$

$$\eta(c) \coloneqq \sqrt{\int_0^1 \int_x^1 j^2(x,y;c)\mathrm{d}y\mathrm{d}x}, \tag{5.61}$$

and c is the design variable of the target system in (5.44).

Proof. The inverse backstepping transformation from $\psi(x,t)$ to $\phi(x,t)$ specified by the kernel function $\ell(x,y)$ in (5.58) is written as

$$\psi(x,t) = \phi(x,t) + \int_x^1 \ell(x,y)\phi(y,t)\mathrm{d}y. \tag{5.62}$$

Applying the triangle inequality yields

$$\begin{aligned}
\|\psi(x,t)\| &\leq \|\phi(x,t)\| + \left\|\int_x^1 \ell(x,y)\phi(y,t)\mathrm{d}y\right\| \\
&= \|\phi(x,t)\| + \sqrt{\int_0^1 \left(\int_x^1 \ell(x,y)\phi(y,t)\mathrm{d}y\right)^2 \mathrm{d}x} \\
&\leq \|\phi(x,t)\| + \sqrt{\int_0^1 \left(\int_x^1 \ell^2(x,y)\mathrm{d}y\right)\left(\int_x^1 \phi^2(y,t)\mathrm{d}y\right)\mathrm{d}x} \\
&\leq \|\phi(x,t)\| + \sqrt{\int_0^1 \left(\int_x^1 \ell^2(x,y)\mathrm{d}y\right)\|\phi(y,t)\|^2\mathrm{d}x} \\
&= \left(1 + \sqrt{\int_0^1 \int_x^1 \ell^2(x,y)\mathrm{d}y\mathrm{d}x}\right)\|\phi(x,t)\| \\
&\leq \gamma\left(1 + \sqrt{\int_0^1 \int_x^1 \ell^2(x,y)\mathrm{d}y\mathrm{d}x}\right)\|\widetilde{T}(x,t)\|,
\end{aligned} \tag{5.63}$$

where the first inequality originates from the Cauchy-Schwarz Ineuqality, and the last inequality stems from the Lipschitz continuity of function $f(T(x,t))$ in Remark 10. A similar computation can be performed based on the forward backstepping transformation (5.43) to conclude

$$\|\widetilde{T}(x,t)\| \leq \left(1+\sqrt{\int_0^1\int_x^1 j^2(y,t)\mathrm{d}y\mathrm{d}x}\right)\|\omega(x,t)\|. \tag{5.64}$$

Therefore, in view of (5.63) and (5.64), function $\psi(x,t)$ verifies the inequality $\|\psi(\cdot,t)\| \leq \kappa(c;\gamma)\|\omega(\cdot,t)\|$. ■

Through Lemma 12, the stability analysis of the error system (5.38)-(5.42) defined in terms of the spatial L_2 norm can then be established via the target system.

Theorem 13 (Convergence of State Observer)**.** *Consider the observer error dynamics (5.38)-(5.40), and let the observer gains $p_1(x)$ and p_{10} be as in (5.52) and (5.53). Given Lipschitz constant γ, if the design parameters c and c_1 are chosen such that*

$$c > \kappa(c;\gamma) - \frac{1}{4}, \qquad c_1 \geq \frac{1}{2} - \frac{h}{k}, \tag{5.65}$$

then the origin of the error dynamics $\widetilde{T}(x,t)=0$ is exponentially stable in the sense of spatial L_2 norm, without the presence of the in-domain uncertainty and the output uncertainty, i.e., $\varepsilon(x,t)=0$, $\mu(t)=0$, and $\nu(t)=0$.

Proof. Consider the Lyapunov functional candidate for system (5.44)-(5.46):

$$W_1(t) = \frac{1}{2}\int_0^1 \omega^2(x,t)\mathrm{d}x = \frac{1}{2}\|\omega(x,t)\|^2. \tag{5.66}$$

The time derivative of the Lyapunov function $W_1(t)$ along the state trajectory can be computed as

$$\dot{W}_1 = \int_0^1 \omega(x,t)\omega_t(x,t)\mathrm{d}x = \int_0^1 \omega\omega_{xx}\mathrm{d}x + \int_0^1 \omega\psi\mathrm{d}x - c\int_0^1 \omega^2\mathrm{d}x. \tag{5.67}$$

Applying the integration by parts to the first term, and Cauchy-Schwarz Inequality to the second term at the right hand side of (5.67) result in

$$\dot{W}_1 \leq -\left(c_1+\frac{h}{k}\right)\omega^2(1) - \|\omega_x\|^2 + \|\psi\|\|\omega\| - c\|\omega\|^2. \tag{5.68}$$

Applying Poincaré Inequality, $-\|\omega_x\|^2 \leq \frac{1}{2}\omega^2(1) - \frac{1}{4}\|\omega\|^2$, to the second term at the right hand side of (5.68), and substituting the third term with (5.59), yields

$$\dot{W}_1 \leq -\left(c_1+\frac{h}{k}-\frac{1}{2}\right)\omega^2(1) - \left[c+\frac{1}{4}-\kappa(c;\gamma)\right]\|\omega\|^2. \tag{5.69}$$

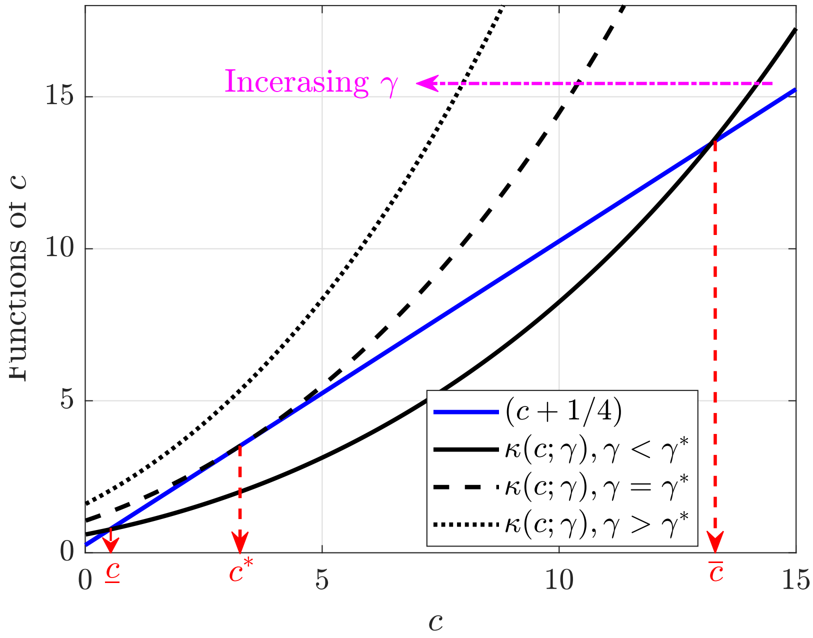

Figure 5.2: Illustration of design parameter selection. As γ increases, the function $\kappa(c;\gamma)$ shifts towards the upper-left dimension and the span between $\underline{c}$ and $\overline{c}$ shrinks accordingly. When $\gamma < \gamma^* \approx 1.053$, it is insured that there always exists a design parameter c such that the conditions in (5.65) hold.

If the design parameters are chosen such that $c_1 \geq \frac{1}{2} - \frac{h}{k}$ and $c > \kappa(c;\gamma) - \frac{1}{4}$, (5.69) is simplified to

$$\frac{\mathrm{d}}{\mathrm{d}t}\|\omega\| \leq -\left[c + \frac{1}{4} - \kappa(c;\gamma)\right]\|\omega\|, \tag{5.70}$$

which confirms the exponential stability of $\omega(x,t)$ as well as $\widetilde{T}(x,t)$ in the sense of spatial L_2 norm. ■

Remark 21. *The state observer design imposes a simple linear output error injection for a nonlinear plant model, without having to perform linearization and compute time-varying kernel functions [64]. However, its limitation is analogous to that of observer design for Lipschitz nonlinear ODE system [101], which will be discussed in the next section.*

5.3 Numerical Selection of Design Parameters

The design criteria (5.65) for the stability of the origin of the error system enforces c_1 to be greater than a fixed constant $(1/2 - h/k)$, and an affine function of c to be greater than a nonlinear function $\kappa(c;\gamma)$. It should be highlighted that for a Lipschitz constant γ, $\kappa(c;\gamma)$

increases near exponentially with respect to c since the backstepping kernel function $j(x, y)$ is dependent on the modified Bessel function $I_1(\cdot)$. The condition in (5.65) requires a linear function to dominate an exponential function, no matter that the argument of function $I_1(\cdot)$ in (5.51) is a square root of c. Satisfaction of the condition in (5.65) is then totally dependent upon the Lipschitz bound of the nonlinearity γ. A numerical study is now presented to explore the space of γ for which a feasible solution to the inequality of (5.65) exists.

Fig. 5.2 provides the visualization for the affine function $(c + 1/4)$ and the nonlinear function $\kappa(c; \gamma)$ with respect to c. As an illustrative example, when $\gamma < \gamma^*$, $\kappa(c; \gamma)$ (the black solid line) intersects with $(c+1/4)$ (the blue solid line) at two distinct points, namely $c = \bar{c}$ and $c = \underline{c}$. Hence, under this scenario, $c + 1/4 > \kappa(c; \gamma)$ if and only if $\underline{c} < c < \bar{c}$. With increasing γ, the plot of $\kappa(c; \gamma)$ shifts towards the up-left direction, and the span on the c-axis between $c = \bar{c}$ and $c = \underline{c}$ shrinks accordingly. At the critical point when $\gamma = \gamma^*$, the straight line $(c+1/4)$ is tangential to $\kappa(c; \gamma)$ (the black dotted line) and they intersect at a single point $c = c^*$. Furthermore, when $\gamma > \gamma^*$, $\kappa(c; \gamma)$ will never intersect with $(c + 1/4)$ for all possible c. Thus, when $\gamma < \gamma^*$, there always exists a c such that $c + 1/4 > \kappa(c; \gamma)$ stays true. Using a bisection method, the critical value of the Lipschitz constant for which a solution to (63) exists is $\gamma^* \approx 1.053$.

5.4 State Estimation for Uncertain Plant Model

In the previous section, a state observer as well as its convergence properties for an uncertainty-free plant model was analyzed. In this section, the plant model with in-domain and output uncertainties emerged from the heat generation reduction is under examination. We employ the same observer structure as in (5.34)-(5.37) for the uncertain plant model (5.16)-(5.20), and analyze the boundedness of the estimation error in the sense of spatial L_2 norm.

Subtracting (5.34)-(5.37) from (5.16)-(5.20) produces the observer's error dynamics:

$$\begin{aligned}\widetilde{T}_t(x,t) = {} & \widetilde{T}_{xx}(x,t) + \phi(x,t) - p_1(x)\widetilde{T}(1,t) \\ & - p_1(x)\nu(t) + \varepsilon(x,t), \qquad (5.71)\\ \widetilde{T}_x(0,t) = {} & -\frac{h}{k}\mu(t), \qquad (5.72)\\ \widetilde{T}_x(1,t) = {} & -\left(\frac{h}{k} + p_{10}\right)\widetilde{T}(1,t) - p_{10}\nu(t), \qquad (5.73)\end{aligned}$$

The analysis in this scenario is different from the traditional backstepping approach, where the boundary conditions and dynamics are uncertainty-free. The system of interest here, (5.71)-(5.73), imposes not only a nonlinearity, but also in-domain and output uncertainties.

Backstepping Transformation

The backstepping transformation (5.43) maps the error system (5.71)-(5.73) to the target system

$$\begin{aligned}\omega_t(x,t) = {}& \omega_{xx}(x,t) + \psi(x,t) - c\omega(x,t) + r(x)\nu(t) \\ & + \zeta(x,t), \qquad (5.74)\\ \omega_x(0,t) = {}& -\frac{h}{k}\mu(t), \qquad (5.75)\\ \omega_x(1,t) = {}& -\left(c_1 + \frac{h}{k}\right)\omega(1,t) + \big(j(1,1) - c_1\big)\,\nu(t). \qquad (5.76)\end{aligned}$$

The term $r(x)\nu(t)$ accounts for the term $p_1(x)\nu(t)$ in the original error dynamics, and $\zeta(x,t)$ is the transformed functions from $\varepsilon(x,t)$ by the backstepping transformation

$$\varepsilon(x,t) = \zeta(x,t) - \int_x^1 j(x,y)\zeta(y,t)\mathrm{d}y. \tag{5.77}$$

To explicitly determine $j(x,y)$ and $r(x)$ we differentiate both sides of the transformation in (5.43) with respect to x and t and take into account target system (5.74)-(5.76),

$$\begin{aligned}&\int_x^1 \omega(y,t)\left[j_{xx}(x,y) - j_{yy}(x,y) + cj(x,y)\right]\mathrm{d}t + \omega(1,t)\left[p_1(x) + j_y(x,1) + \left(c_1 + \frac{h}{k}\right)j(x,1)\right]\\ &+ \nu(t)\left[r(x) - \int_x^1 j(x,y)r(y)\mathrm{d}y + p_1(x) + p_{10}j(x,1)\right] - \omega(x,t)\left[2\frac{\partial}{\partial x}j(x,x) + c\right] = 0.\end{aligned} \tag{5.78}$$

Note that (5.78) has to hold for all $(x,t) \in [0,1]\times[0,\infty)$. Hence, we arrive at the same kernel PDE for $j(x,y)$ as the kernel PDE in (5.48)-(5.50) for the uncertainty-free case. Moreover, the observer gains also remain unchanged from those in (5.52) and (5.53). Finally, in view of (5.78), $r(x)$ has to verify $\Delta(x) = 0$ with

$$\Delta(x) \coloneqq r(x) - \int_x^1 j(x,y)r(y)dy + p_1(x) + p_{10}j(x,1). \tag{5.79}$$

The exact analytic expression of $r(x)$ will be derived in the subsequent section.

Inverse Backstepping Transformation

We employ the same inverse backstepping transformation (5.54) as that used for the uncertainty-free case. Differentiating both sides of (5.54) with respect to x and t produces

$$\begin{aligned}
&\int_x^1 \widetilde{T}(y,t)\left[-\ell_{xx}(x,y)+\ell_{yy}(x,y)+c\ell(x,y)\right]\mathrm{d}t\\
&-\widetilde{T}(1,t)\left[p_1(x)+\ell_y(x,1)+\left(\frac{h}{k}+p_{10}\right)\ell(x,1)+\int_x^1 \ell(x,y)p_1(y)\mathrm{d}y\right]\\
&-\nu(t)\left[r(x)+p_1(x)+p_{10}\ell(x,1)+\int_x^1 \ell(x,y)p_1(y)\mathrm{d}y\right]\\
&-\widetilde{T}(x,t)\left[2\frac{\partial}{\partial x}\ell(x,x)+c\right]=0. \qquad (5.80)
\end{aligned}$$

Again, (5.80) has to hold for all $(x,t)\in[0,1]\times[0,\infty)$. Interestingly, in this case, the inverse backstepping kernel $\ell(x,y)$ still satisfies the kernel PDE (5.55)-(5.57), so that the analytic solution for $\ell(x,y)$ is given by (5.58). Now, define the following:

$$(\star) := p_1(x)+\ell_y(x,1)+\left(\frac{h}{k}+p_{10}\right)\ell(x,1)+\int_x^1 \ell(x,y)p_1(y)\mathrm{d}y, \qquad (5.81)$$

$$(\star\star) := r(x)+p_1(x)+p_{10}\ell(x,1)+\int_x^1 \ell(x,y)p_1(y)\mathrm{d}y. \qquad (5.82)$$

Proposition 2. *Let* $(\star)$ *and* $(\star\star)$ *be as in (5.81) and (5.82). Then*

$$(\star)=0, \quad (\star\star)=0, \qquad (5.83)$$

for all $x\in[0,1]$, *if and only if*

$$r(x)=\ell_y(x,1)+\frac{h}{k}\ell(x,1). \qquad (5.84)$$

We verify Proposition 2 with the assistance of the following Lemma.

Lemma 14. *For* $j(x,y)$ *and* $\ell(x,y)$, *which are the kernels for the backstepping and the inverse backstepping transformations, it holds from [64] and [147] that*

$$\begin{aligned}
\ell(x,y)&=j(x,y)+\int_x^y j(x,\xi)\ell(\xi,y)\mathrm{d}\xi \qquad (5.85)\\
&=j(x,y)+\int_x^y \ell(x,\xi)j(\xi,y)\mathrm{d}\xi. \qquad (5.86)
\end{aligned}$$

We are now positioned to provide the proof for Proposition 2 utilizing Lemma 14.

Proof. Differentiate both sides of (5.86) with respect to y, and evaluate at $y = 1$:

$$\ell_y(x,1) = j_y(x,1) + \ell(x,1)j(1,1) + \int_x^1 \ell(x,\xi)j_y(\xi,1)\mathrm{d}\xi. \tag{5.87}$$

Then substitute $j_y(x,1)$ and $j(1,1)$ from (5.52)-(5.53) into (5.87):

$$\begin{aligned}\ell_y(x,1) = &- p_1(x) - \left(c_1 + \frac{h}{k}\right)j(x,1) + \ell(x,1)(c_1 - p_{10})\\ &+ \int_x^1 \ell(x,\xi)\left[- p_1(\xi) - \left(c_1 + \frac{h}{k}\right)j(\xi,1)\right]\mathrm{d}\xi.\end{aligned} \tag{5.88}$$

Re-arranging terms in (5.88) yields

$$(\star) = -\left(c_1 + \frac{h}{k}\right)\left[j(x,1) - \ell(x,1) + \int_x^1 \ell(x,\xi)j(\xi,1)\mathrm{d}\xi\right]. \tag{5.89}$$

In addition, note from (5.86) that

$$\ell(x,1) = j(x,1) + \int_x^1 \ell(x,\xi)j(\xi,1)\mathrm{d}\xi. \tag{5.90}$$

In view of (5.89) and (5.90), we have $(\star) = 0$. Moreover,

$$(\star) - (\star\star) = \ell_y(x,1) + \frac{h}{k}\ell(x,1) - r(x). \tag{5.91}$$

Hence, $(\star\star) = 0$ if and only if $r(x)$ verifies

$$r(x) = \ell_y(x,1) + \frac{h}{k}\ell(x,1). \tag{5.92}$$

Finally, we need to check if the proposed $r(x)$ in (5.92) satisfies $\Delta(x) = 0$. First, notice from (5.85) that

$$\ell_y(x,1) = j_y(x,1) + \ell(1,1)j(x,1) + \int_x^1 j(x,\xi)\ell_y(\xi,1)\mathrm{d}\xi. \tag{5.93}$$

Substitute $r(x)$ from (5.92), $p_1(x)$ in (5.52), and p_{10} from (5.53), altogether into (5.79), and we arrive at

$$\begin{aligned}\Delta(x) &= \ell_y(x,1) + \frac{h}{k}\ell(x,1) - j_y(x,1) - \left(c_1 + \frac{h}{k}\right)j(x,1) + \left(c_1 + \frac{c}{2}\right)j(x,1)\\ &\quad - \int_x^1 j(x,\xi)\left[\ell_y(\xi,1) + \frac{h}{k}\ell(\xi,1)\right]\mathrm{d}\xi\\ &= \frac{h}{k}\left[\ell(x,1) - j(x,1) - \int_x^1 j(x,\xi)\ell(\xi,1)\mathrm{d}\xi\right]\\ &\equiv 0,\end{aligned} \tag{5.94}$$

where the second equality stems from substituting $\ell_y(x,1)$ from (5.93), and the last equality is obtained from (5.85). ■

Stability of the Target System

Often the disturbances $\mu(t)$ and $\nu(t)$ that enter the system via the boundary conditions (5.75) and (5.76) become problematic when proving the stability of the target system, due to the terms that have multiplication between the uncertainties and state ω if L_2 spatial norm is used as the Lyapunov function. To tackle this issue, we utilize the following invertible transformation $\omega(x,t) \mapsto z(x,t)$ to transfer the boundary uncertainties into the in-domain dynamics:

$$\omega(x,t) = z(x,t) + \frac{h}{2k}\mu(t)(1-x)^2 - \frac{1}{2}p_{10}\nu(t)(x^2-1). \tag{5.95}$$

The second and third terms at the right hand side of (5.95) is utilized to cancel the uncertainty terms in the boundary conditions of the target system. It is also worth noting that $z(1,t) = \omega(1,t)$. Differentiating the above transformation with respect to x and t yields the dynamics for $z(x,t)$:

$$z_t(x,t) = z_{xx}(x,t) + \psi(x,t) - cz(x,t) + e_\mu(x,t) + e_\nu(x,t) + \zeta(x,t), \tag{5.96}$$

where $e_\mu(x,t)$ and $e_\nu(x,t)$ are terms that are associated with the uncertainties in the output equation:

$$e_\mu(x,t) = \frac{h}{k}\mu(t) - \frac{h}{2k}(1-x)^2(c\mu(t) + \mu_t(t)), \tag{5.97}$$

$$e_\nu(x,t) = (r(x) - p_{10})\nu(t) + \frac{1}{2}p_{10}(x^2-1)(c\nu(t) + \nu_t(t)). \tag{5.98}$$

The boundary conditions for $z(x,t)$ is given by

$$z_x(0,t) = \omega_x(0,t) + \frac{h}{k}\mu(t) = 0. \tag{5.99}$$

$$z_x(1,t) = \omega_x(1,t) + p_{10}\nu(t) = -\left(c_1 + \frac{h}{k}\right)z(1,t), \tag{5.100}$$

The uncertainties are no longer at the boundaries in the z-system. We provide the stability analysis in the sense of spatial L_2 norm for the original error system through the analysis of the transformed system (5.96)-(5.100).

Theorem 15 (Convergence of Robust Observer)**.** *Consider the observer error dynamics (5.71)-(5.73), and let the observer gains $p_1(x)$ and p_{10} be as in (5.52) and (5.53). Given Lipschitz constant γ, if the design parameters c and c_1 are selected such that (5.65) is satisfied, then in the presence of the in-domain uncertainty and the output uncertainty, i.e., $\varepsilon(x,t) \neq 0$, $\mu(t) \neq 0$, and $\nu(t) \neq 0$, the estimation error remains bounded in the sense of L_2 norm denoted by $\|\widetilde{T}(\cdot,t)\| \leq R_B(c,c_1)$ as $t \to \infty$, where*

$$R_B(c,c_1) := \eta(c)\left[\frac{\beta(c,c_1)}{\alpha(c)} + \lambda(c,c_1)\right]. \tag{5.101}$$

Specifically,

$$\alpha(c) \coloneqq c - \kappa(c;\gamma) + \frac{1}{4}, \tag{5.102}$$

$$\begin{aligned}\beta(c,c_1) \coloneqq{}& \kappa(c;\gamma)\lambda(c,c_1) + \frac{h}{k}\overline{\mu} + \frac{h}{2\sqrt{5}k}\overline{U} + \|r(x) - p_{10}\|\overline{\nu}\\ &+ \sqrt{\frac{2}{15}}|p_{10}|\,\overline{V} + (1+\rho(c))\overline{\varepsilon},\end{aligned} \tag{5.103}$$

$$\lambda(c,c_1) \coloneqq \sqrt{\frac{h^2}{20k^2}\overline{\mu} + \frac{2}{15}p_{10}^2\overline{\nu} + \frac{3h}{20k}|p_{10}|\,\overline{E}}, \tag{5.104}$$

where p_{10} is given by (5.53), and

$$\overline{U} = \max_t\{c\mu(t) + \dot{\nu}(t)\}, \tag{5.105}$$

$$\overline{V} = \max_t\{c\nu(t) + \dot{\nu}(t)\}, \tag{5.106}$$

$$\overline{E} = \max_t\{\mu(t)\nu(t)\}. \tag{5.107}$$

Proof. Consider again the Lyapunov functional candidate for system (5.96)-(5.100) using spatial L_2 norm,

$$W_2(t) = \frac{1}{2}\int_0^1 z^2(x,t)\mathrm{d}x = \frac{1}{2}\|z(x,t)\|^2. \tag{5.108}$$

The time derivative of the Lyapunov function $W(t)$ along the state trajectory can be computed as

$$\begin{aligned}\dot{W}_2(t) &= \int_0^1 z(x,t)z_t(x,t)\mathrm{d}x\\ &= \int_0^1 zz_{xx}\mathrm{d}x + \int_0^1 z\psi\mathrm{d}x - c\int_0^1 z^2\mathrm{d}x + \int_0^1 ze_\mu\mathrm{d}x + \int_0^1 ze_\nu\mathrm{d}x + \int_0^1 z\zeta\mathrm{d}x.\end{aligned} \tag{5.109}$$

Applying the integration by parts to the first term, and Cauchy-Schwarz Inequality to the second, fourth, fifth, and sixth term at the right hand side of (5.109) results in

$$\dot{W}_2(t) \le -\left(c_1 + \frac{h}{k}\right)z^2(1) - \|z_x\|^2 - c\|z\|^2 + \big(\|\psi\| + \|e_\mu\| + \|e_\nu\| + \|\zeta\|\big)\|z\|. \tag{5.110}$$

Now consider the transformation (5.95) and apply triangular inequality to conclude

$$\begin{aligned}\|\omega\| &\le \|z\| + \left\|\frac{h}{2k}\mu(t)(1-x)^2 - \frac{1}{2}p_{10}\nu(t)(x^2-1)\right\|\\ &\le \|z\| + \lambda(c,c_1),\end{aligned} \tag{5.111}$$

so that the upper bound for $\|\psi\|$ given by (5.59) is explicitly expressed in terms of state in z system:

$$\|\psi\| \leq \kappa(c;\gamma)\|z\| + \kappa(c;\gamma)\lambda(c,c_1). \tag{5.112}$$

Furthermore, from (5.97) and (5.98), the following upper bounds are imposed on e_μ and e_ν,

$$\|e_\mu\| \leq \frac{h}{k}\overline{\mu} + \frac{h}{2\sqrt{5}k}\overline{U}, \tag{5.113}$$

$$\|e_\nu\| \leq \|r(x) - p_{10}\|\overline{\nu} + \sqrt{\frac{2}{15}}|p_{10}|\,\overline{V}. \tag{5.114}$$

Finally, by recognizing the inverse backstepping transformation $\zeta(x,t) \mapsto \varepsilon(x,t)$,

$$\zeta(x,t) = \varepsilon(x,t) + \int_x^1 \varepsilon(y,t)\ell(x,y)\mathrm{d}y, \tag{5.115}$$

similar strategy as that in (5.63) can be employed to derive the upper bound on $\|\zeta(\cdot,t)\|$:

$$\|\zeta(\cdot,t)\| \leq (1+\rho(c))\overline{\varepsilon}. \tag{5.116}$$

Substituting (5.111)-(5.114) and (5.116) into the right hand side of (5.110), and applying the Poincaré Inequality, $-\|z_x\|^2 \leq \frac{1}{2}z^2(1) - \frac{1}{4}\|z\|^2$, to the second term in the right hand side of (5.110), yields

$$\dot{W}_2 \leq -\left(c_1 + \frac{h}{k} - \frac{1}{2}\right)z^2(1) - \alpha(c)\|z\|^2 + \beta(c,c_1)\|z\|. \tag{5.117}$$

If c_1 is chosen such that $c_1 \geq \frac{1}{2} - \frac{h}{k}$ and $\alpha(c) > 0$, or equivalently $c > \kappa(c;\gamma) - \frac{1}{4}$, the comparison principle applied to (5.117) gives

$$\|z(\cdot,t)\| \leq \frac{\beta(c,c_1)}{\alpha(c)} + \left[\|z(\cdot,0)\| - \frac{\beta(c,c_1)}{\alpha(c)}\right]e^{-\alpha(c)t}. \tag{5.118}$$

Since the inverse transformation $z(x,t) \mapsto \omega(x,t)$ is unique:

$$z(x,t) = \omega(x,t) - \frac{h}{2k}\mu(t)(1-x)^2 + \frac{1}{2}p_{10}\nu(t)(x^2-1), \tag{5.119}$$

and the backstepping transformation (5.43) is invertible, an upper bound of $\|\widetilde{T}(\cdot,t)\|$ is computed via the sequence of inequalities based on (5.64) and (5.111):

$$\|\widetilde{T}(\cdot,t)\| \leq \eta(c)\left[\|z(\cdot,t)\| + \lambda(c,c_1)\right]. \tag{5.120}$$

When $t \to \infty$, the exponential terms at the right hand side of (5.120) decays to zero. Under this scenario,

$$\|\widetilde{T}(\cdot,t)\| \leq \eta(c)\left[\frac{\beta(c,c_1)}{\alpha(c)} + \lambda(c,c_1)\right] \tag{5.121}$$

This completes the proof. ■

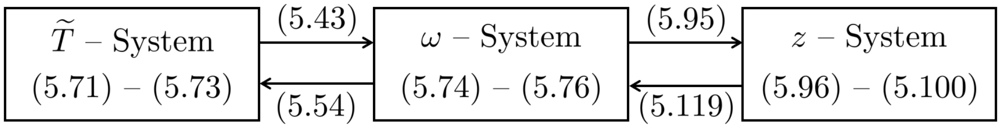

Figure 5.3: Summary of the coordinate transformations. The forward backstepping transformation (5.43) transforms the original error system $\widetilde{T}$ to the target system ω. Moreover, the transformation (5.95) transfers the boundary uncertainties in ω system into the in-domain dynamics of z system. It has been proven that all transformations are invertible and the inverse transformations are uniquely defined.

Symbols	Values	Units
T_0	298.15	K
$T_{\min}$	298.15	K
$R_s(T_0)$	4.7	mΩ
E_a	36.9	kJ/mol
$k_{\overline{x}}$	28	W/(m·K)
$h_{\overline{x}}$	13.4	W/(m^2· K)
R	8.314	J/(mol·K)
$L_{\overline{x}}$	0.216	m
$L_{\overline{y}}$	0.129	m
$L_{\overline{z}}$	0.0072	m
ρ	2118	kg/m^3
c_p	711	J/(kg·K)

Table 5.1: Model Parameters for a Prismatic Cell

For a given Lipschitz constant $\gamma < \gamma^*$, one can minimize the size of the error ball R_B to achieve robust estimation by formulating and solving the optimization problem

$$\begin{aligned} \underset{c,c_1}{\text{minimize}} \quad & R_B(c, c_1) \\ \text{subject to} \quad & \kappa(c;\gamma) - c - 1/4 < 0, \\ & -c_1 + 1/2 - h/k \leq 0, \\ & c > 0. \end{aligned}$$

A complete description of model transformations are depicted in Fig. 5.3.

5.5 Simulation Studies

In this section, we present simulation studies to demonstrate the performance of the proposed observers. In this study, the distributed one-dimensional thermal model (5.16)-(5.21) is used as the plant model. The model parameters and the geometric properties for a prismatic

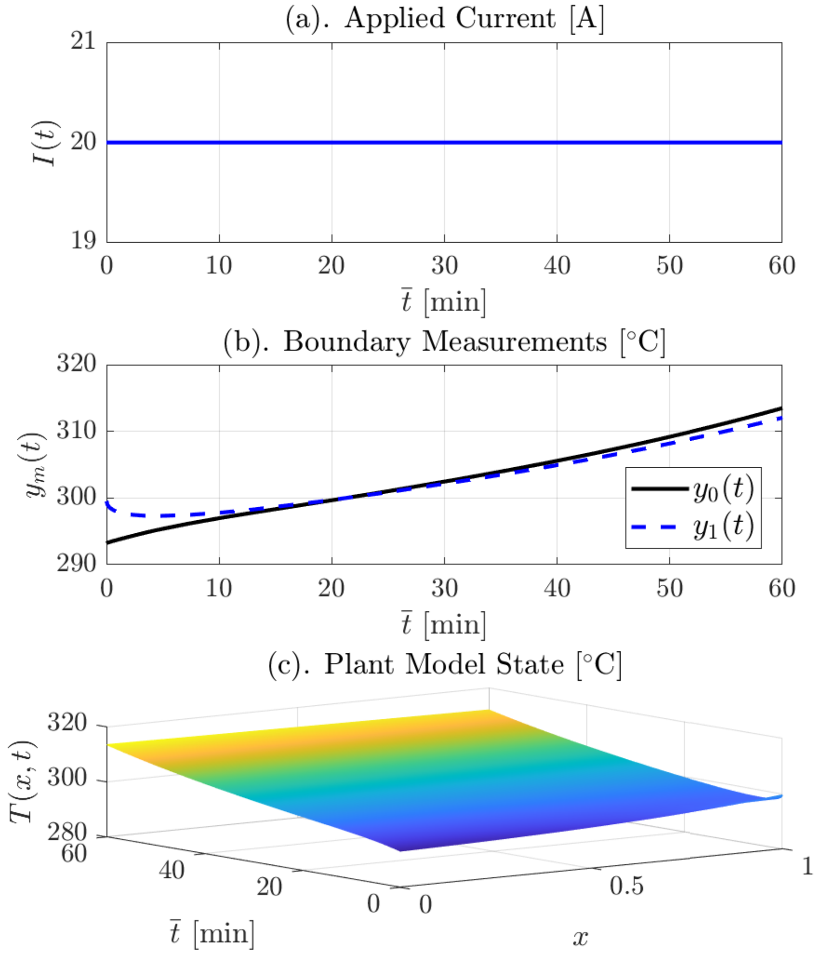

Figure 5.4: The plant model behavior under a constant charging profile. (a) Applied input current; (b) Boundary measurements; (c) spatially distributed state.

cell are adopted from [136, 156, 159], and are enumerated in Table 5.1. Let the premises in Assumption 1 hold, and then we evaluate the effectiveness of the proposed observer with and without the in-domain and output uncertainties. For all simulations, the state estimates are initialized with incorrect values. Specifically, $T(x,0) = 292.15 + \exp(2x)$ and $\widehat{T}(x,0) = 300 + 10\sin(8x)$.

No In-domain and Output Uncertainties

We first illustrate the performance of the proposed temperature estimation approach under no uncertainties, i.e. $\varepsilon(x,t) = 0$, $\mu(t) = 0$ and $\nu(t) = 0$, $\forall(x,t) \in [0,1] \times [0,\infty)$. A constant current, shown in Fig. 5.4(a), is applied to the battery thermal model. The simulation time is $\bar{t} \in [0, 60\text{min}]$, and the spatial domain is $\overline{x} \in [0, 0.216\text{m}]$, i.e., $x \in [0,1]$. The finite difference

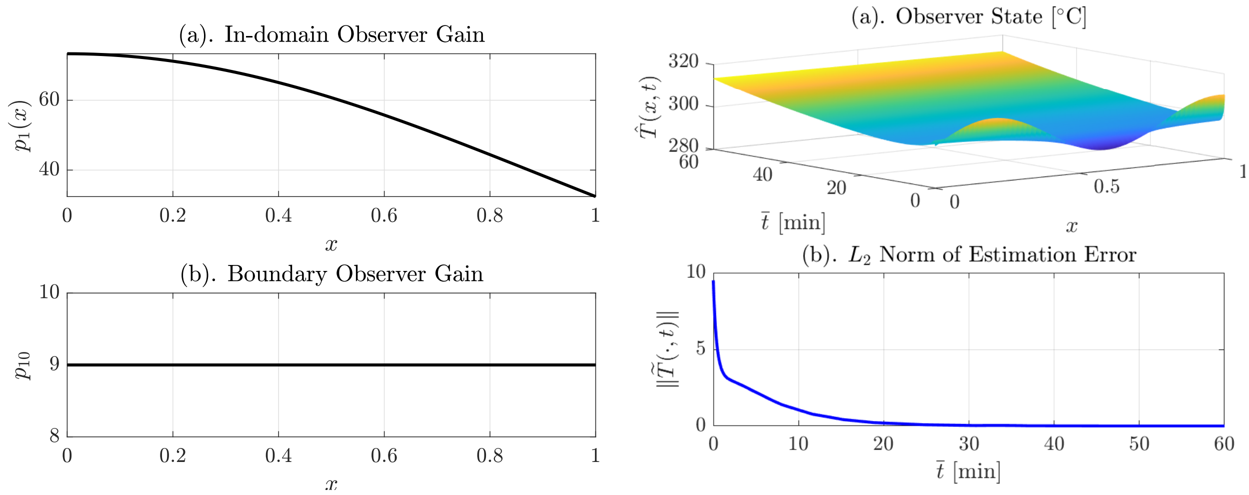

Figure 5.5: **Left:** The in-domain and boundary observer gains. The observer gains are analytically calculated using (5.52) and (5.53), based on the selection of parameter c and the analytic expression of backstepping kernel (5.51). **Right:** Observer results for a constant charging profile. True initial condition: $T(x,0) = 292.15 + \exp(2x)$. Observer initial condition: $\widehat{T}(x,0) = 300 + 10\sin(8x)$. The estimation error converges to zero exponentially in the sense of L_2 spatial norm, thus confirming the conclusion from Theorem 13. (a) Observer state; (b) Estimation error.

method is employed to numerically discretize the plant model. The plant model is discretized spatially with 50 grid points. The PDE boundary conditions are handled by the method of imaginary point. The simulation is performed in MATLAB. The measured boundary signals and the spatially distributed temperature are sketched in Fig. 5.4 (b) and (c), respectively. The maximum absolute current in this specific case is $|I|_{\max} = 20$A. The expression in (5.23) provides the numerical value of the Lipschitz constant for the nonlinearity $f(T(x,t))$ with respect to $T(x,t)$ in the plant model, i.e. $\gamma = 0.62 < \gamma^*$. This guarantees that there always exists a design parameter c such that the observer convergence conditions presented in Theorem 13 are fulfilled. In fact, the feasible ranges for the design parameters in this case are $0.55 < c < 12.74$ and $c_1 \geq 0.4$. With the choice of $c = 8$ and $c_1 = 5$, the in-domain observer gain $p_1(x)$ and the boundary observer gain p_{10} can be computed with the assistance of backstepping kernels (5.48) and (5.55), and their spatial evolution is plotted in the left of Fig. 5.5. Finally, the right of Fig. 5.5 presents the observer state and the exponential convergence of the L_2 norm of temperature estimation error to zero, even with the incorrect initialization. The numerical simulation results confirm our conclusion in Theorem 13.

(a). Applied Current [A]

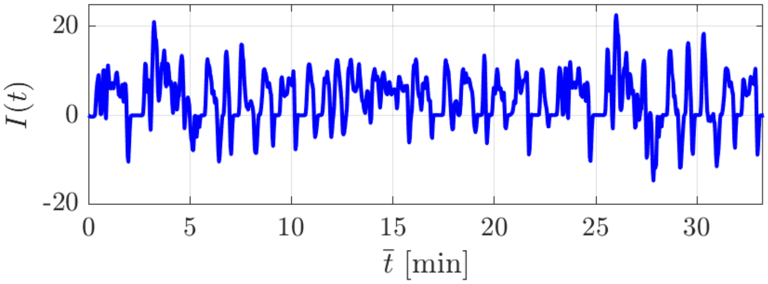

(b). Boundary Measurements [°C]

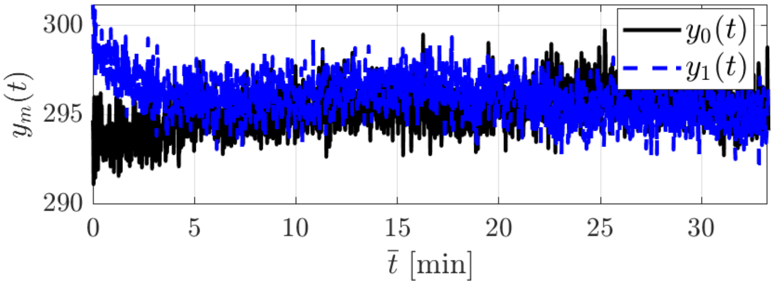

(c). Plant Model State [°C]

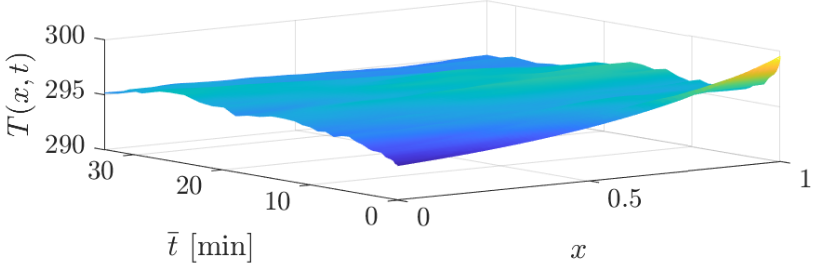

Figure 5.6: The plant model behavior for a vehicle-like charging and discharging cycle, extracted from an UDDS cycle. Gaussian noise with 1 °C variance and zero mean, i.e., $\mu(t) \sim \mathcal{N}(0,1)$ and $\nu(t) \sim \mathcal{N}(0,1)$, are injected to the boundary measurement signals $y_0(t)$ and $y_1(t)$. Uniformly distributed random noise $\varepsilon(x,t)$ is injected into the dynamical equation (5.16). (a) Noise-corrupted boundary measurements; (c) Spatially distributed state.

With In-domain and Output Uncertainties

In this section, Gaussian noises with 1°C variance and zero mean, i.e. $\mu(t) \sim \mathcal{N}(0,1)$ and $\nu(t) \sim \mathcal{N}(0,1)$, are manually injected to the boundary measurement signals $y_0(t)$ and $y_1(t)$. Further, an uniformly distributed random noise $\varepsilon(x,t)$ is included in the dynamical equation (5.16). The profile of the applied current, which is extracted from the Urban Dynamometer Driving Schedule (UDDS) driving cycle, is shown in Fig. 5.6(a). The noise-corrupted boundary measurements and spatially distributed temperature state are plotted in Fig. 5.6(b) and (c), respectively. Once again, the observer state is initialized to incorrect spatially distributed values, and the norm of estimation error converges quickly to a ball of (a). Observer State [°C]

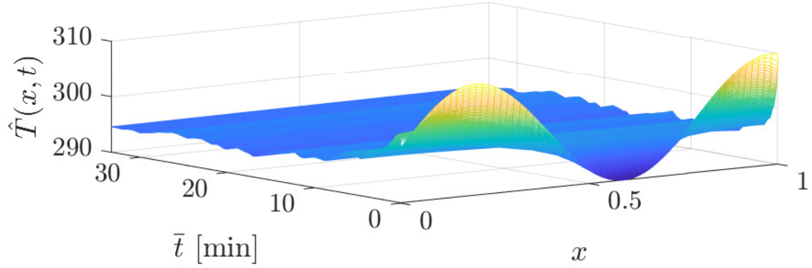

(b). L_2 Norm of Estimation Error

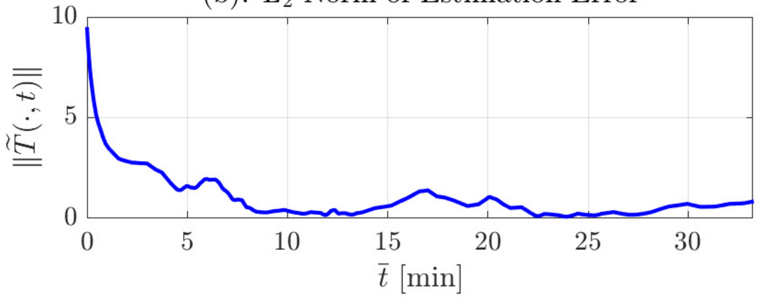

Figure 5.7: Observer results for a vehicle-like charging and discharging cycle extracted from UDDS cycle, subject to in-domain and output uncertainties. True initial condition: $T(x,0) = 293.15 + 3\exp(3x)$. Observer initial condition: $\widehat{T}(x,0) = 300 + 10\sin(8x)$. The estimation error converges to a ball of radius R_B around the equilibrium point $\widetilde{T} = 0$ in the sense of L_2 spatial norm, thus justifying the conclusion from Theorem 15. (a) Observer state; (b) Estimation error.

radius R_B around the equilibrium point $\widetilde{T} = 0$, as can be seen in Fig. 5.7. Notice that the same observer gains $p_1(x)$ and p_{10} as that from the uncertainty-free case are utilized (in the left of Fig. 5.5). The simulation results support the conclusion in Theorem 15.

Estimation with Constant Resistance

In this section, we demonstrate the benefit of using a nonlinear resistance with respect to temperature in the observer dynamics (5.34), against adopting simply a constant resistance. Specifically, we examine the following state observer

$$\Gamma_t(x,t) = \Gamma_{xx}(x,t) + I^2(t)R_0 + p_1(x)\left(y_1(t) - \Gamma(1,t)\right), \tag{5.122}$$

$$\Gamma_x(0,t) = \frac{h}{k}\left(T_\infty - y_0(t)\right), \tag{5.123}$$

$$\Gamma_x(1,t) = \frac{h}{k}\left(T_\infty - \Gamma(1,t)\right) + p_{10}\left(y_1(t) - \Gamma(1,t)\right), \tag{5.124}$$

where $\Gamma(x,t)$ is the temperature estimation produced by the observer system (5.122)-(5.124). Symbol R_0 represents a constant resistance, and the value of R_0 is the resistance at the

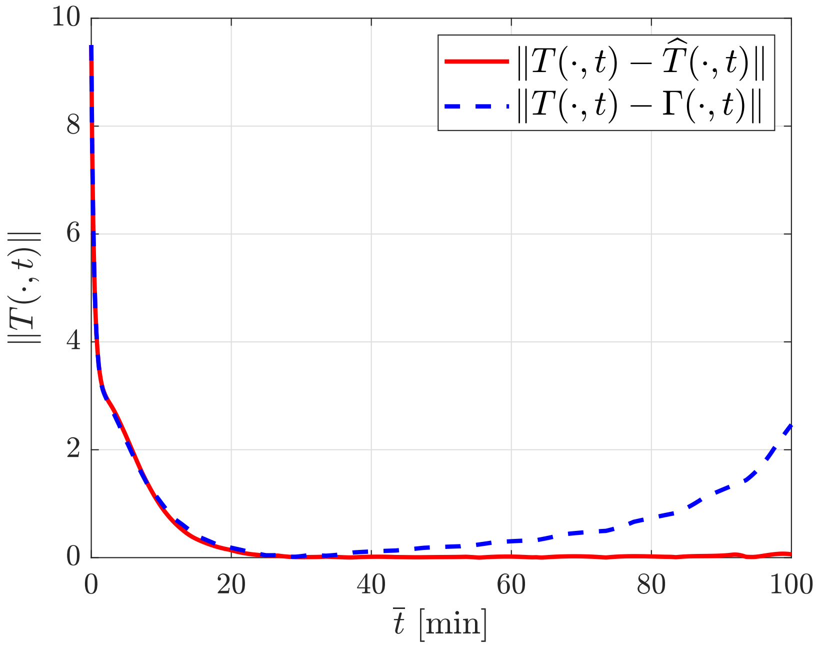

Figure 5.8: Spatial L_2 norm of the estimation errors produced by (i) the observer with a nonlinear resistance with respect to temperature, and (ii) the observer using a constant resistance.

reference temperature, i.e. $R_0 = R_s(T_0)$. The measurements $y_0(t)$ and $y_1(t)$ are generated from the uncertainty-free nonlinear plant model (5.28)-(5.33). Fig. 5.8 demonstrates the spatial L_2 norm of the estimation errors under a constant current (given by Fig. 5.4(a)) produced by (i) the observer with nonlinear resistance with respect to temperature, namely the observer system (5.34)-(5.36), and (ii) the observer using a constant resistance, namely the observer system (5.122)-(5.124), utilizing the same set of observer gains $p_1(x)$ and p_{10} as those in (5.52)-(5.53). It is noted that the estimation error from case (i) converges to zero exponentially in the sense of spatial L_2 norm, whereas the error generated by case (ii) initially decays toward zero with a similar decaying rate in case (i), but starts to deviate from zero when the real resistance evolves with changing temperature.

5.6 Conclusion and Future Works

The knowledge of real-time battery temperature enables safe operation in battery management systems. In this study, a boundary observer is proposed for a one-dimensional Li-ion battery distributed parameter thermal model subject to in-domain and output uncertainties. The thermal model is formulated such that the nonlinear heat generation term is Lipschitz continuous with respect to state, thus the considered plant model fits the structure of a parabolic semilinear PDE. The observer is designed based on the backstepping technique, by converting the error system to a prescribed stable target system. Without the presence of the uncertainties, it is shown that the observer error dynamics is exponentially stable, thanks to the Lipschitz continuous nonlinearity. In the presence of uncertainties, we transfer the uncertainties in the boundary conditions of the target system into the in-domain dynamics. If the uncertainties are unknown but with appropriate known bounds, the state estimation error converges to an error ball around the equilibrium point, which is explicitly characterized in terms of uncertainty bounds, observer parameters, and model parameters. The sufficient condition on the Lipschitz constant such that the proposed estimation scheme guarantees exponential convergence is derived. The numerical study illustrates the effectiveness and robustness of the observer algorithm with respect to Lipschitz nonlinearities, and in-domain and output uncertainties. Moreover, the observer design here is one of the first for a semilinear parabolic PDE state estimation problem without performing linearization.

Future works include extending the proposed estimation algorithm to higher-dimensional thermal model, e.g., three-dimensional models, and exploring the necessary and sufficient conditions to ensure observer's exponential convergence.

Chapter 6

State and Disturbance Estimator for Unstable Reaction-Advection-Diffusion PDE with Boundary Disturbance

6.1 Introduction

This chapter investigates a general reaction-advection-diffusion partial differential equation (PDE) with unknown boundary disturbances, which can be utilized to describe a variety of systems such as electrochemistry (Li-ion batteries) [38], thermal/fluid flows [160], and structural acoustics [161], with uncertain flux at one end. As we have discussed in Chapter 1, the working principle of an electrochemical Li-ion battery cell is based on the intercalation and de-intercalation of lithium ions in the electrode active materials and the transport of the lithium ions between two electrodes. These mechanisms are often modeled by the diffusion/transport processes. The objective of this chapter is to estimate the disturbance at the boundary of a reaction-advection-diffusion partial PDE, in order to attenuate the effect of disturbance in the feedback controller design. With the disturbance estimation signal, a state estimator is also proposed.

In the past few decades, the boundary control and estimation of PDE systems has gained significant research attention, due to their high-fidelity model accuracy in describing many processes. When uncertainties enter the PDE system through the boundaries or in-domain dynamics, there generally have been three types of methods developed to tackle such issue: adaptive control [66], sliding mode control [162, 163], and active disturbance control [164, 165]. See [162] for an excellent review.

The active disturbance rejection control (ADRC) method was initially introduced by Han [166], which has been proven to be effective in dealing with disturbances in PDE systems. A crucial step in ADRC is to estimate the time-varying disturbance using available boundary measurements. The convergence problem of ADRC was solved in [167], and this approach has been widely applied to disturbance attenuation in feedback controller design in PDE systems. For instance, a boundary output feedback stabilization for a one-dimensional anti-stable wave equation with control matched disturbance is examined in [165]. A disturbance estimator for a wave PDE on a time-varying domain is studied in [168], and an output feedback controller is further designed utilizing the disturbance estimates [164]. The output feedback stabilization for an unstable wave equation with general boundary measurement disturbance is introduced in [169]. The application of ADRC on the unstable heat equation with boundary uncertainties is presented in [162], as well as the sliding mode controller design. In [170], stabilization of an unstable 1-D heat equation with boundary uncertainty and external disturbance is achieved by designing an unknown input type state observer.

In this chapter, we design a combined disturbance and state estimator for an unstable reaction-advection-diffusion PDE with boundary disturbance, by adopting a similar methodology from [168, 170]. The contribution of this paper lies in

- *Designing a disturbance estimator for boundary disturbance in an unstable reaction-advection-diffusion PDE system, and derive a sufficient condition on the reaction coefficient, for which the disturbance estimator achieves asymptotic convergence.*
- *Proposing an asymptotically convergent state estimator for the unstable reaction-advection-diffusion PDE using the estimated disturbance signal, adopting the backstepping technique.*

The reminder of this chapter is organized as follows. Chapter 6.2 discusses the problem set-up, well-posedness of the plant model. The disturbance estimator and the corresponding convergence analysis are presented in Chapter 6.3. Chapter 6.4 presents the state estimator design using the estimated disturbance signal, by employing the backstepping method. Chapter 6.5 provides a numerical simulation to visualize the performance of the proposed estimators. Chapter 6.6 summarizes and concludes the paper.

Notation. Throughout this chapter, $u(x,t)$ denotes the state variable with the dependence on space variable x and time variable t. The x and t subscripts represent partial derivatives with respect to the notated variable: $u_t = \partial u/\partial t$, $u_x = \partial u/\partial x$, and $u_{xx} = \partial^2 u/\partial x^2$. The dot symbol denotes derivative with respect to time t, e.g. $\dot{T} = \mathrm{d}T/\mathrm{d}t$, and the prime symbol represents derivative with respect to space x, e.g. $X' = \mathrm{d}X/\mathrm{d}x$. The $L^2(0,1)$ spatial norm is defined as

$$\|u(\cdot,t)\| = \sqrt{\int_0^1 u^2(x,t)\mathrm{d}x}.$$

6.2 Problem Specification.

We consider the following reaction-advection-diffusion PDE with boundary disturbance, where the disturbance is anti-collocated with the applied control input:

$$\begin{aligned} z_t(x,t) &= z_{xx}(x,t) + b z_x(x,t) + \lambda_0 z(x,t), && (6.1)\\ z_x(0,t) &= q_0 z(0,t) + d_0(t), && (6.2)\\ z_x(1,t) &= Q(t), && (6.3)\\ z(x,0) &= z_0(x), && (6.4)\\ y(t) &= \left[z(0,t), z(1,t)\right], && (6.5) \end{aligned}$$

where b, λ_0, and q_0 are constants, $d_0(t)$ represents the boundary disturbance, and $Q(t)$ denotes the control input. The signals at both boundaries are measured. The following change of variables (gauge transformation) [81]:

$$u(x,t) = z(x,t)e^{\frac{b}{2}x}, \tag{6.6}$$

transforms the system (6.1)-(6.5) to (6.7)-(6.11), with coefficients, disturbance, and control input mapped accordingly, as follows,

$$\begin{aligned} u_t(x,t) &= u_{xx}(x,t) + \lambda u(x,t), && (6.7)\\ u_x(0,t) &= q u(0,t) + d(t), && (6.8)\\ u_x(1,t) &= U(t), && (6.9)\\ u(x,0) &= u_0(x). && (6.10)\\ y_m(t) &= \left[u(0,t), u(1,t)\right]. && (6.11) \end{aligned}$$

Symbol $d(t)$ represents the disturbance on the heat flux at one boundary, $U(t)$ denotes the known control input, and λ and q are constants.

Assumption 7. *The disturbance $d(t) \in \mathbb{R}$ is upper and lower bounded:*

$$\left|d(t)\right| \leq \overline{d}, \quad \forall t \in [0,\infty), \tag{6.12}$$

where $\overline{d}$ is an unknown positive number.

The analysis in this paper is based on the system (6.7)-(6.11). Our objective is to estimate the disturbance $d(t)$ as well as the state $u(x,t)$ by utilizing the boundary measurements $y_m(t)$.

Theorem 16. *The linear boundary value problem (BVP) (6.7)-(6.10) is well-posed with initial data $u_0(\cdot) \in L^2(0,1)$, provided that the disturbance $d(t)$ and control input $U(t)$ are bounded.*

We utilize Lemma 21 [171] (in Appendix) to prove Theorem 16.

Proof. Define the operator

$$(\mathcal{L}u)(x,t) = -u_{xx}(x,t) - \lambda u(x,t), \quad (x,t) \in (0,1) \times [0,\infty). \tag{6.13}$$

Similarly, define the boundary condition operator

$$(\mathcal{B}u)(x,t) = \begin{cases} u_x(0,t) - qu(0,t) & x = 0, t \in [0,\infty) \\ u_x(1,t) & x = 1, t \in [0,\infty) \end{cases} \tag{6.14}$$

which allows the boundary condition to be expressed as

$$(\mathcal{B}u)(x,t) = h(x,t), \tag{6.15}$$

where $h(0,t) = d(t)$ and $h(1,t) = U(t)$. Then, by defining

$$(\mathcal{H}u) = \begin{cases} u_t(x,t) + (\mathcal{L}u)(x,t) & (x,t) \in (0,1) \times [0,\infty) \\ (\mathcal{B}u)(x,t) & (x,t) \in \{0,1\} \times [0,\infty) \\ u(x,0) & x \in [0,1], t = 0 \end{cases} \tag{6.16}$$

and

$$\mathcal{F}(x,t) = \begin{cases} 0 & (x,t) \in (0,1) \times [0,\infty) \\ h(x,t) & (x,t) \in \{0,1\} \times [0,\infty) \\ u_0(x) & x \in [0,1], t = 0 \end{cases} \tag{6.17}$$

the BVP (6.7)-(6.10) can be written in the compact form:

$$(\mathcal{H}u)(x,t) = \mathcal{F}(x,t). \tag{6.18}$$

The operator $\mathcal{H}$ is linear. The inverse monotonicity of $\mathcal{H}$ can be confirmed by contradiction. Moreover, a non-negative comparison function $\phi(x)$, $x \in [0,1]$, can be computed by constructing a low-degree polynomial, for example, $\phi(x) = Ax^2 + Bx + C$, and choose constants A, B, C to verify $\mathcal{H}\phi(x) \geq 1$ for $x \in [0,1]$. Then the well-posedness follows immediately from Lemma 21, by choosing $\|\psi\|_u = \|\psi\|_\infty = \max_{(x,t)\in[0,1]\times[0,\infty)} \psi$, for $\psi \in L^2(0,1)$. Furthermore, from (A.4) we have that

$$\max_{x\in[0,1]} \left|u(x,t)\right| \leq \left[\max_{x\in[0,1]} \phi(x)\right] \cdot \max\left\{\|h(x,t)\|_\infty, \|u_0(x)\|_\infty\right\}, \tag{6.19}$$

which dictates that a bound on the magnitude of the solution has been determined. ∎

Remark 22. *The plant model dynamics (6.7)-(6.10) is unstable for sufficiently large λ and q. This motivates future ADRC design where the disturbance estimation is required to attenuate the actual disturbance.*

6.3 Disturbance Estimator Design

In this section, we detail the disturbance estimator design for the system (6.7)-(6.10) using the boundary measurement $y_m(t)$. We introduce the following auxiliary system:

$$\eta_t(x,t) = \eta_{xx}(x,t) + \lambda\eta(x,t), \tag{6.20}$$

$$\eta(0,t) = u(0,t) - \zeta(0,t), \tag{6.21}$$

$$\eta_x(1,t) = -\alpha\eta(1,t), \tag{6.22}$$

where $\zeta(x,t)$ satisfies the following system:

$$\zeta_t(x,t) = \zeta_{xx}(x,t) + \lambda\zeta(x,t), \tag{6.23}$$

$$\zeta_x(0,t) = qu(0,t), \tag{6.24}$$

$$\zeta_x(1,t) = U(t) + \alpha(u(1,t) - \zeta(1,t)). \tag{6.25}$$

Specifically, ζ system consists of a copy of the plant model (6.7)-(6.10) with the output error injection using the measurement of $u(1,t)$. The η system is completely determined by the measured signal $u(0,t)$ and the boundary value from the ζ system. We further define the estimate for the disturbance $\hat{d}(t)$ to be

$$\hat{d}(t) = \eta_x(0,t). \tag{6.26}$$

The system (6.20)-(6.22), (6.23)-(6.25), together with (6.26), is the *disturbance estimator*. The constant $\alpha > 0$ is to be determined such that the disturbance estimate $\hat{d}(t)$ reconstructs the actual disturbance $d(t)$ asymptotically.

Convergence of Disturbance Estimator

Define the variable $y(x,t) = u(x,t) - \zeta(x,t)$, which satisfies the system:

$$y_t(x,t) = y_{xx}(x,t) + \lambda y(x,t), \tag{6.27}$$

$$y_x(0,t) = d(t), \tag{6.28}$$

$$y_x(1,t) = -\alpha y(1,t), \tag{6.29}$$

and we also define $\tilde{w} = y - \eta$, which verifies

$$\tilde{w}_t(x,t) = \tilde{w}_{xx}(x,t) + \lambda\tilde{w}(x,t), \tag{6.30}$$

$$\tilde{w}(0,t) = 0, \tag{6.31}$$

$$\tilde{w}_x(1,t) = -\alpha\tilde{w}(1,t). \tag{6.32}$$

The purpose of $\tilde{w}$ system is that the disturbance estimation error $\tilde{d}(t) = d(t) - \hat{d}(t)$ can be expressed by the boundary signal of $\tilde{w}$, as follows,

$$\tilde{d} = d - \hat{d} = y_x(0,t) - \eta_x(0,t) = \tilde{w}_x(0,t). \tag{6.33}$$

Thus, the convergence analysis of disturbance estimation error $\tilde{d}(t)$ is equivalent to the convergence of $\tilde{w}_x(0,t)$.

Remark 23. *The systems (6.27)-(6.29) and (6.30)-(6.32) are well-posed. The structure of the proof is analogous to Theorem 16 using Lemma 21.*

From now on, we aim to determine the values of parameter λ such that there always exists a tuning parameter $\alpha > 0$ for which $\tilde{w}(x,t)$ and $\tilde{w}_x(x,t)$ converge to zero as $t \to \infty$ in the sense of L^2 norm. Prior to presenting the main theorem, we require a few lemmas. The next lemma is the extension of the well-known Poincaré Inequality [81, 172]. For the reader's convenience, we provide a sketch of the proof.

Lemma 17. *For any function $\tilde{w}(x,t)$ with $x \in [0,1]$ and $t \in [0,\infty)$, that is twice continuously differentiable on $x \in [0,1]$,*

$$\|\tilde{w}_x(x,t)\|^2 \le 2\tilde{w}_x^2(1,t) + 4\|\tilde{w}_{xx}(x,t)\|^2. \tag{6.34}$$

Proof.

$$\int_0^1 \tilde{w}_x^2 \mathrm{d}x = x\tilde{w}_x^2\Big|_0^1 - 2\int_0^1 x\tilde{w}_x\tilde{w}_{xx}\mathrm{d}x \le \tilde{w}_x^2(1) + \frac{1}{2}\int_0^1 \tilde{w}_x^2\mathrm{d}x + 2\int_0^1 x^2\tilde{w}_{xx}^2\mathrm{d}x, \tag{6.35}$$

where Young's Inequality has been used. Therefore,

$$\int_0^1 \tilde{w}_x^2\mathrm{d}x \le 2\tilde{w}_x^2(1) + 4\int_0^1 \tilde{w}_{xx}^2\mathrm{d}x. \tag{6.36}$$

■

Lemma 18. *System (6.30)-(6.32) admits an unique solution $\tilde{w}(x,t)$ which satisfies*

$$\|\tilde{w}_{xx}(\cdot,t)\| \le \|\tilde{w}_{xx}(\cdot,0)\|Le^{-\Omega t}, t \ge 0, \tag{6.37}$$

where L and Ω are positive constants, given that $\lambda < x_0^2$, where x_0 is the smallest positive solution to

$$\tan(x) = -\frac{x}{\alpha}. \tag{6.38}$$

The proof of Lemma 18 is omitted here. The readers may refer to Lemma 3.1 in [170] for details.

Now we present the following lemma describing the stability results for the system (6.30)-(6.32).

Lemma 19. *For any initial data $\tilde{w}_0(\cdot) \in L^2(0,1)$, and $\lambda < 3 - 2\sqrt{2}$, there exists a constant $\alpha > 0$ such that $\tilde{w}(x,t)$ in the system (6.30)-(6.32) is asymptotically stable for all $x \in [0,1]$. Moreover, $\tilde{w}_x(0,t)$ converges to zero as $t \to \infty$.*

Proof. Consider the Lyapunov functional

$$V(t) = \frac{\alpha}{2}\tilde{w}^2(1,t) + \frac{1}{2}\left\|\tilde{w}\right\|^2 + \frac{1}{2}\left\|\tilde{w}_x\right\|^2. \tag{6.39}$$

The time derivative of the Lyapunov functional $V(t)$ along the trajectory of $\tilde{w}(x,t)$ is

$$\begin{aligned}
\dot{V}(t) &= \alpha\tilde{w}(1)\tilde{w}_t(1) + \int_0^1 \tilde{w}\tilde{w}_t \mathrm{d}x + \int_0^1 \tilde{w}_x\tilde{w}_{xt}\mathrm{d}x \\
&= \alpha\tilde{w}(1)\tilde{w}_t(1) + \tilde{w}(x)\tilde{w}_x(x)\Big|_0^1 - \int_0^1 \tilde{w}_x^2\mathrm{d}x + \lambda\int_0^1 \tilde{w}^2\mathrm{d}x + \tilde{w}_t(x)\tilde{w}_x(x)\Big|_0^1 - \int_0^1 \tilde{w}_t\tilde{w}_{xx}\mathrm{d}x \\
&= -\alpha\tilde{w}^2(1) - \|\tilde{w}_x\|^2 + \lambda\|\tilde{w}\|^2 - \|\tilde{w}_{xx}\|^2 - \lambda\int_0^1 \tilde{w}\tilde{w}_{xx}\mathrm{d}x \\
&= -\alpha\tilde{w}^2(1) - \|\tilde{w}_x\|^2 + \lambda\|\tilde{w}\|^2 - \|\tilde{w}_{xx}\|^2 + \lambda\alpha\tilde{w}^2(1) + \lambda\|\tilde{w}_x\|^2 \\
&= -\alpha(1-\lambda)\tilde{w}^2(1) + \lambda\|\tilde{w}\|^2 - (1-\lambda)\|\tilde{w}_x\|^2 - \|\tilde{w}_{xx}\|^2 \\
&\le -\alpha(1-\lambda)\tilde{w}^2(1) + \lambda\|\tilde{w}\|^2 - (1-\lambda)\|\tilde{w}_x\|^2 + \frac{1}{2}\tilde{w}_x^2(1) - \frac{1}{4}\|\tilde{w}_x\|^2 \\
&= -\left[\alpha(1-\lambda) - \frac{\alpha^2}{2}\right]\tilde{w}^2(1) + \lambda\|\tilde{w}\|^2 - \left(\frac{5}{4} - \lambda\right)\|\tilde{w}_x\|^2,
\end{aligned} \tag{6.40}$$

where integration by parts has been utilized multiple times, and Lemma 17 is applied in the last inequality. Observing the last line of (6.40), λ clearly has a significant impact on the sign of $\dot{V}(t)$. A sufficient condition posed on λ for which there always exists a $\alpha > 0$ such that $V(t)$ is asymptotically stable is to be determined.

We first require $\lambda < 5/4$ in view of the last term involving $\|\tilde{w}_x\|$ in (6.40), and introduce two positive constants p_1 and p_2 as follows,

$$p_1 + p_2 = \frac{5}{4} - \lambda, \text{ and } p_1, p_2 > 0, \tag{6.41}$$

so that (6.40) becomes

$$\begin{aligned}
\dot{V}(t) =& -\left[\alpha(1-\lambda) - \frac{\alpha^2}{2}\right]\tilde{w}^2(1) + \lambda\|\tilde{w}\|^2 - p_1\|\tilde{w}_x\|^2 - p_2\|\tilde{w}_x\|^2 \\
\le& -\left[(1-\lambda) - \frac{\alpha}{2} - \frac{p_1}{2\alpha}\right]\alpha\tilde{w}^2(1) - \left(\frac{p_1}{4} - \lambda\right)\|\tilde{w}\|^2 - p_2\|\tilde{w}_x\|^2.
\end{aligned} \tag{6.42}$$

where the Poincaré Inequality is used. According to (6.42), if there exists a p_1 such that there always exists a $\alpha > 0$ so that the following conditions hold:

$$(1-\lambda) - \frac{\alpha}{2} - \frac{p_1}{2\alpha} > 0, \quad \frac{p_1}{4} - \lambda > 0, \quad \frac{5}{4} - \lambda - p_1 > 0, \quad \text{and } p_1 > 0, \tag{6.43}$$

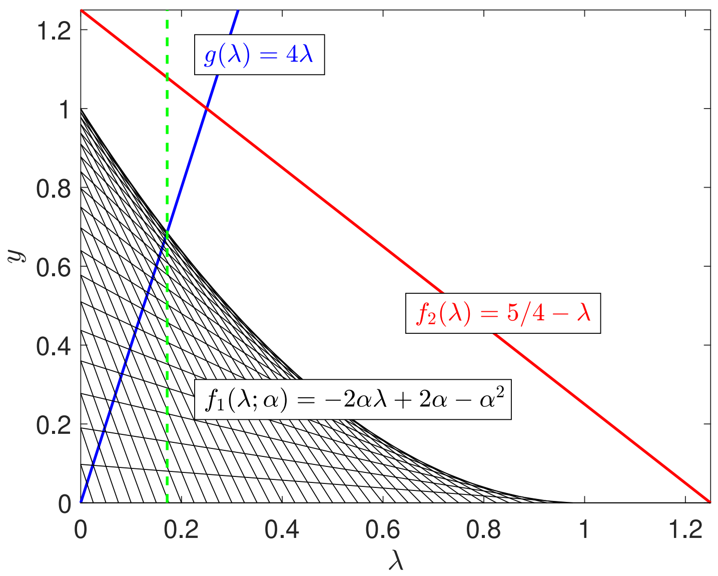

Figure 6.1: Visualization of analysis of sufficient condition for reaction coefficient λ.

then the Lyapunov functional $V(t)$ decays exponentially with decaying rate β:

$$\dot{V} \leq -\beta V. \tag{6.44}$$

where $\beta > 0$ is defined by

$$\beta = \min\left\{(1-\lambda) - \frac{\alpha}{2} - \frac{p_1}{2\alpha}, \frac{p_1}{4} - \lambda, \frac{5}{4} - \lambda - p_1\right\}. \tag{6.45}$$

In order for p_1 to be well-defined by (6.43) for some α, we must enforce

$$\max\{0, 4\lambda\} < p_1 < \min\left\{2\alpha(1-\lambda) - \alpha^2, \frac{5}{4} - \lambda\right\}. \tag{6.46}$$

We solve for the values of λ such that there always exists a $\alpha > 0$ so that (6.46) holds. We consider two cases: $\lambda \leq 0$ and $\lambda > 0$.

Case 1: $\lambda \leq 0$. In this case, the left hand side (LHS) of (6.46) is LHS $= \max\{0, 4\lambda\} = 0$. On the right hand side (RHS) of (6.46), we have $5/4 - \lambda > 0$. Let $f(\alpha) = 2\alpha(1-\lambda) - \alpha^2$, and $f(\alpha)$ takes its peak value $f_{\max} = (1-\lambda)^2 > 0$ at $\alpha = (1-\lambda) > 0$, which means that there always exists a $\alpha > 0$ such that RHS > 0. Thus, there always exists a $p_1 > 0$ that satisfies (6.46) if $\lambda \leq 0$.

Case 2: $\lambda > 0$. In this scenario, LHS $= 4\lambda$. Let $g(\lambda) = 4\lambda$, $f_1(\lambda;\alpha) = 2\alpha(1-\lambda) - \alpha^2$, and $f_2(\lambda) = 5/4 - \lambda$. Note that function f_1 is parameterized by α. Our objective is to search for the values of $\lambda > 0$ such that there exists a α so that the minimum of f_1 and f_2 is larger than g. Observe that f_1 intersects the y-axis at $(0, 2\alpha-\alpha^2)$, which is below the point $(0, 5/4)$ where f_2 intersects the y-axis, because $2\alpha-\alpha^2 \le 1\ \forall\alpha > 0$. On the other hand, f_1 intersects the x-axis at $((2-\alpha)/2, 0)$, which is to the left of $(5/4, 0)$ where f_2 intersects the x-axis, because $(2-\alpha)/2 < 1\ \forall\alpha > 0$. Therefore, we can conclude that RHS $= \min\{f_1, f_2\} = f_1$ due to these two facts, and the fact that f_1 is linear in λ. These arguments are geometrically illustrated in Fig. 6.1, where the family of f_1 parameterized by $\alpha > 0$ (in black) is always less than f_2 (in red). Hence, the maximum value of λ such that there exists α such that $g \le f_1$ can be obtained by finding the value of λ where f_1 and g intersect. Equating f_1 and g yields

$$\lambda = \frac{2\alpha-\alpha^2}{4+2\alpha}, \text{ and } \lambda_{\max} = 3-2\sqrt{2}. \tag{6.47}$$

Consequently, there always exists a $\alpha > 0$ such that (6.46) is satisfied when $0 < \lambda < 3-2\sqrt{2}$.

Combining Case 1 and 2, we conclude that there always exists a $\alpha > 0$ such that (6.46) is satisfied provided that $\lambda < 3-2\sqrt{2}$. Under this condition, (6.44) gives us

$$V(t) \le V_0 e^{-\beta t}, \tag{6.48}$$

where V_0 is the initial condition of $V(t)$. With this, we can also conclude from (6.39) that

$$\|\tilde{w}\|, \|\tilde{w}_x\| \to 0, \text{ as } t \to \infty. \tag{6.49}$$

Applying Agmon's ([81], Lemma 2.4) and Young's Inequality yields

$$\max_{x\in[0,1]} |\tilde{w}|^2 \le \tilde{w}^2(0) + 2\|\tilde{w}\|\|\tilde{w}_x\| \le \|\tilde{w}\|^2 + \|\tilde{w}_x\|^2, \tag{6.50}$$

where (6.31) is used, and we have thus proved that

$$\tilde{w}(x,t) \to 0 \quad \forall\ x \in [0,1], \qquad \text{as } t \to \infty. \tag{6.51}$$

According to the Fundamental Theorem of Calculus, triangle inequality, and Cauchy-Schwarz Inequality:

$$\begin{aligned} \tilde{w}_x(0,t) &= \tilde{w}_x(1,t) - \int_0^1 \tilde{w}_{xx} \mathrm{d}x \\ &\le \alpha\big|\tilde{w}(1,t)\big| + \left(\int_0^1 \tilde{w}_{xx}^2 \mathrm{d}x\right)^{\frac{1}{2}} \\ &\le \alpha\big|\tilde{w}(1,t)\big| + \|\tilde{w}_{xx}(\cdot,0)\| L e^{-\omega t}, \end{aligned} \tag{6.52}$$

where Lemma 18 has been imposed in the last inequality. As $t \to \infty$, $\tilde{w}(1,t) \to 0$ according to (6.51), and it can be concluded that $\tilde{w}_x(0,t) \to 0$ as $t \to \infty$. This concludes the proof for Lemma 19. ∎

With Lemma 19, we are now positioned to present and prove the main result of the disturbance estimator.

Theorem 20. *For any initial data $\tilde{d}_0$ which is finite, and $\lambda < 3 - 2\sqrt{2}$, there exists a constant $\alpha > 0$ such that the error for the disturbance estimation $\tilde{d}(t)$ converges to zero asymptotically,.*

Proof. According to (6.33),

$$\tilde{d} = d - \hat{d} = \tilde{u}_x(0,t) - \eta_x(0,t) = \tilde{w}_x(0,t), \tag{6.53}$$

which according to Lemma 19, is asymptotically stable. ■

Remark 24. *The state in the system (6.20)-(6.22) is bounded in the sense of L^2 norm, as follows,*

$$\lim_{t\to\infty} \|\eta(\cdot,t)\| < \infty. \tag{6.54}$$

This can be verified by using the Lyapunov functional $W = \frac{1}{2}\|\eta(\cdot,t)\|^2$. Since η is bounded and $\tilde{w}$ is asymptotically stable in the sense of L^2 norm, y is bounded in the sense of L^2 norm. In addition, as u is bounded according to (6.19), ζ is also bounded in the sense of L^2 norm. We have thus proved that all the states in disturbance estimator stay bounded in the sense of L^2 norm.

Remark 25. *The sufficient condition on λ for the asymptotic convergence of the disturbance estimator is conservative, since the majorization of $\dot{V}(t)$ in (6.42) using Poincaré Inequality is not tight.*

6.4 State Estimator Design

This section presents a state estimator utilizing the asymptotically convergent disturbance estimation signal. The state estimator is designed by using a copy of the plant model (6.7)-(6.10) with an error injection, i.e.

$$\hat{u}(x,t) = \hat{u}_{xx}(x,t) + \lambda\hat{u}(x,t) + k(x)\tilde{u}(1,t), \tag{6.55}$$

$$\hat{u}_x(0,t) = qu(0,t) + \hat{d}(t), \tag{6.56}$$

$$\hat{u}_x(1,t) = U(t) + k_1\tilde{u}(1,t), \tag{6.57}$$

$$\hat{u}(x,0) = \hat{u}_0(x), \tag{6.58}$$

where $\hat{u}(x,t)$ represents the estimation of $u(x,t)$, and $k(x)$ and k_1 are, respectively, spatially-distributed and constant observer gains to be determined to achieve stability of state estimation error $\tilde{u}(x,t) = u(x,t) - \hat{u}(x,t)$. Note that the disturbance estimation $\hat{d}(t)$ is injected into the boundary of the state estimator. The disturbance estimator is autonomous and upstream from the state estimator, so they are convergent independently.

Subtracting (6.55)-(6.58) from (6.7)-(6.10) yields the state estimation error dynamics:

$$\tilde{u}_t(x,t) = \tilde{u}_{xx}(x,t) + \lambda\tilde{u}(x,t) - k(x)\tilde{u}(1,t), \tag{6.59}$$

$$\tilde{u}_x(0,t) = \tilde{d}(t), \tag{6.60}$$

$$\tilde{u}_x(1,t) = -k_1\tilde{u}(1,t), \tag{6.61}$$

$$\tilde{u}(x,0) = u_0(x) - \hat{u}_0(x). \tag{6.62}$$

As $t \to \infty$, the disturbance estimation error $\tilde{d}(t)$ at $x = 0$ boundary vanishes when $\lambda < 3-2\sqrt{2}$, according to Theorem 20. Hence, when $\hat{d}(t)$ converges to $d(t)$, we recover a boundary condition with left end insulated, i.e.

$$\tilde{u}_x(0,t) = 0. \tag{6.63}$$

To determine the observer gains, we adopt the backstepping approach [81]. We seek a linear Volterra transformation that transforms the state of the error system $\tilde{u}(x,t)$ to the target state $\tilde{v}(x,t)$, by making use of the following expression:

$$\tilde{u}(x,t) = \tilde{v}(x,t) - \int_x^1 \ell(x,y)\tilde{v}(y,t)\mathrm{d}y, \tag{6.64}$$

which maps the error system (6.59), (6.61)-(6.63) to the exponentially stable heat equation (target system):

$$\tilde{v}(x,t) = \tilde{v}_{xx}(x,t), \tag{6.65}$$

$$\tilde{v}_x(0,t) = 0, \tag{6.66}$$

$$\tilde{v}_x(1,t) = 0, \tag{6.67}$$

where $\ell(x,y)$ is the gain kernel. To explicitly determine $\ell(x,y)$, we differentiate the transformation (6.64) with respect to x and t, and conclude that $\ell(x,y)$ must satisfy the following Klein-Gordon PDE:

$$\ell_{xx}(x,y) - \ell_{yy}(x,y) = -\lambda\ell(x,y), \tag{6.68}$$

$$\ell_x(0,y) = 0, \tag{6.69}$$

$$\ell(x,x) = -\frac{\lambda}{2}x, \tag{6.70}$$

in which the boundary condition (6.69)-(6.70) emerges from evaluating (6.64) together with the boundary conditions (6.63) and (6.61). An unique and closed-form analytic solution exists for the kernel $p(x,y)$ [81]:

$$\ell(x,y) = -\lambda y\frac{I_1\Big(\sqrt{\lambda(y^2-x^2)}\Big)}{\sqrt{\lambda(y^2-x^2)}}, \tag{6.71}$$

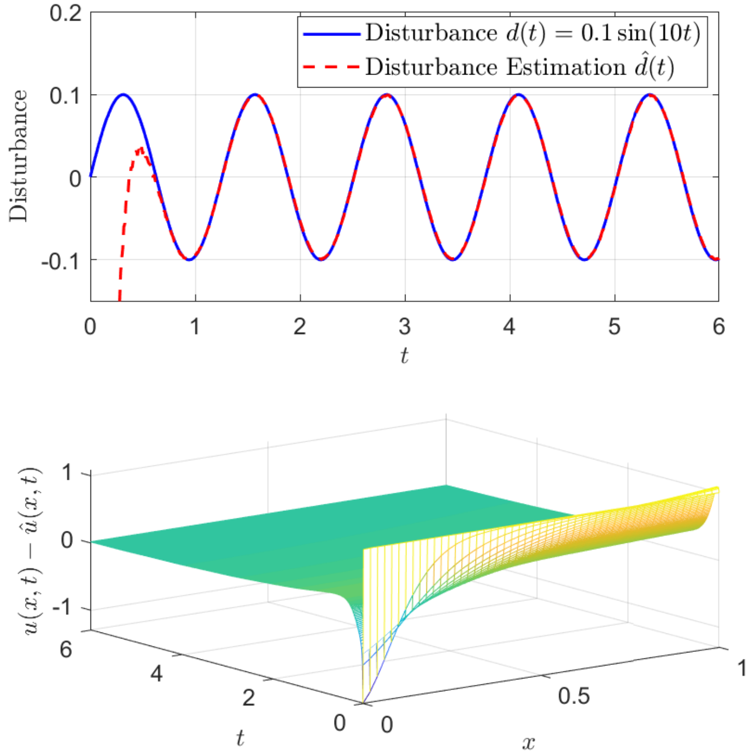

Figure 6.2: The convergence of disturbance estimator and backstepping state estimator.

where $I_1(\cdot)$ is the Modified Bessel Function of the first kind. Moreover, the observer gains are computed as

$$k(x) = -\ell_y(x,1), \quad k_1 = -\ell(1,1). \tag{6.72}$$

Therefore, the observer gains can be determined offline using the kernel PDE solution (6.71). It can also be proven that the linear Volterra transformation (6.64) is invertible [81]. Thus, the exponential stability of the target system (6.65)-(6.67) implies the stability of the original error system (6.59), (6.61)-(6.63).

6.5 Numerical Simulation and Discussion

In this section, we demonstrate the effectiveness of the proposed estimators. The plant model (6.7)-(6.10), disturbance estimator (6.20)-(6.26), and the backstepping state estimator (6.55)-(6.58) are implemented in MATLAB. The finite difference method is employed in spatial discretization. 51 points has been utilized to discretize in space, and the spatial discretization step is $dx = 1/50$. The simulation end time is chosen as $T = 6$s. We use reaction coefficient $\lambda = -1$, constant $q = 0.5$, the disturbance $d(t) = 0.1\sin(5t)$, and input $U(t) = 0$ for an illustrative example. As demonstrated in Figure 6.2, with an appropriate selection of design variable $\alpha > 0$, the disturbance estimation $\hat{d}(t)$ converges to its true value $d(t)$ asymptotically, and the backstepping observer reconstructs the actual state asymptotically.

6.6 Conclusion

In this paper, we propose and rigorously analyze a combined disturbance and state estimator for a class of unstable reaction-advection-diffusion PDEs, subject to unknown boundary disturbance. A sufficient condition on the reaction coefficient is derived, for which the disturbance estimation error is asymptotically stable. The disturbance estimate is combined with a backstepping state observer to also yield asymptotically convergent state estimates. The convergence of the estimators are analyzed by Lyapunov stability analysis. The results of this paper can be applied to ADRC where the disturbance estimate is required to attenuate the actual disturbance in a feedback controller design, as the plant model becomes unstable for certain combination of λ and q. Future work will also examine the necessary condition on reaction coefficient λ for the disturbance estimator to be asymptotically convergent.

Chapter 7

Conclusion

7.1 Dissertation Summary

This dissertation presents frameworks for online model-based state and parameter estimation techniques for Li-ion batteries utilizing nonlinear reduced-order electrochemical, equivalent circuit, and thermal models. In particular, we apply real-time estimation and control techniques for battery state of charge, state of health, and temperature estimation with mathematically provable stability and convergence. As a consequence, the proposed algorithms may improve the remaining life of battery cells/packs by closely monitoring the charge and health status. This is significantly crucial for large-scale battery energy storage systems, ranging from EVs to stationary grid-scale storage, where model-based state feedback control is required for maintaining optimal operation within safe limits.

In Chapter 2, a battery electrical model was coupled with a two-state thermal dynamics to study the battery charge capacity estimation. We proposed a hierarchical estimation scheme. Stage 1 estimates the core temperature, heat generation, and thermal resistance based on a two-state thermal model, and the second stage receives these estimation signals to estimate SOC and capacity (SOH) utilizing a sliding mode observer. We have showed that the algorithm presented can be considered as a novel methodology for combined SOC/SOH estimation, with provable convergence properties, under suitable conditions. This chapter also qualitatively demonstrated the advantages of thermal model-based capacity estimation relative to the traditional current-voltage based methodologies.

Chapter 3 investigates an adaptive observer framework for a reduced-order single particle model couple with diffusion-induced mechanical stress in the electrode solid-phase material. We motivated the importance of monitoring the mechanical response of electrode materials since particle fracture due to stress generation is a major source of battery capacity fade. First, the nonlinear PDE system for the SPM-Stress model is approximated by ODEs using the finite difference method. Next we designed a nonlinear observer based on the sliding mode observer for estimating the anode lithium surface concentration from current and voltage measurements signals. Finally the estimated surface concentration is utilized as a pseudo-measurement signal for combined state and parameter estimation in the adaptive observer, through which the diffusion coefficient and the stress profile are obtained. This chapter extends the understanding of battery degradation associated with diffusion-induced stress, thus protects the battery against particle fracture and consequently extends battery life.

Chapter 4 introduces a novel modeling structure for a battery pack with heterogeneous cells connected in parallel using a differential-algebraic system. Specifically, this chapter analyzed the local observability of a parallel structure from the reduced current and voltage measurements. The designed state observer from this model avoids linearization or canonical transformations, and it only relies on the assumption of Lipschitz nonlinearities. The resulting state observer benefits from considering the cell currents as algebraic states to be simultaneously estimated with the differential states. The results provided a guideline for parallel cell estimation problem which has been overlooked due to multiple unrealistic assumptions. Further, an interval observer was designed and implemented for estimating feasible bounds of cell SOCs in a pack when cell uncertainties are accounted for. A major feature of the proposed interval estimation approach is its scalability, since the number of states of interval observers is independent of the number of cells in a pack.

Chapter 5 captures the thermal dynamics of a Li-ion battery cell using a reduced-order high-fidelity semilinear PDE model. The thermal model was formulated such that the nonlinear heat generation is Lipschitz continuous with respect to the system state. The observer was designed based on the backstepping technique, by converting the error system to a prescribed stable target system. Without the presence of the uncertainties, it was shown that the observer error dynamics is exponentially stable. In the presence of uncertainties, we transformed the uncertainties in the boundary conditions of the target system into the in-domain dynamics. If the uncertainties are unknown but with appropriate known bounds, the state estimation error converges to an error ball around the equilibrium point, which is explicitly characterized in terms of uncertainty bounds, observer parameters, and model parameters. Ultimately, the knowledge of real-time battery temperature enables safe operation in battery management systems. From a theoretical point of view, this chapter also made an invaluable attempt to address the state estimation for a nonlinear parabolic PDE subject to uncertainties without taking linearization.

Chapter 6 exclusively investigates a class of reaction-advection-diffusion PDE system subject to boundary disturbance. The mathematical modeling for electrochemical phenomena inside a battery cell generally adopts a diffusion/transport process. Theoretically, we designed a disturbance estimator for the boundary disturbance in an unstable reaction-advection-diffusion PDE system, and derived a sufficient condition on the reaction coefficient, for which the disturbance estimator achieves asymptotic convergence. Subsequently, we proposed an asymptotically convergent state estimator using the estimated disturbance signal, adopting the backstepping technique. The results of this paper is crucial for the active disturbance rejection control where the disturbance estimate is required to attenuate the actual disturbance in a feedback controller.

In summary, the research reported in this dissertation advances knowledge on the online model-based adaptive estimation that is crucial in the on-board management for Li-ion energy storage systems. This dissertation has demonstrated that this task is crucial for enhancing battery safety, remaining useful lifetime, and subsequent control actions. Importantly, these theoretical developments take steps towards increasing the adoption of Li-ion batteries in the large-scale energy storage systems.

7.2 Perspectives on Future Extensions

The proposed modeling framework and resulting algorithms made notable progress towards intelligently monitoring and managing of battery systems in real time. However, there exist several opportunities to advance the work presented here.

Electrochemical Modeling

The coupled SPM and Stress model utilized in Chapter 3, which is adopted from [54], is derived from physical principles relying on an analogy to thermal stress, and provides a quantitative aggregated stress prediction, which is useful to understand battery SOH associated with intercalation-induced stress. Opportunities exist for estimator designs based on improved electrochemical stress models that account for temperature and high current. Furthermore, the stress-enhanced models need to be validated against experimental stress data. Towards this goal, there exists a burgeoning body of research on sensors for electrode stresses, e.g. [12].

Modeling for battery packs naturally inherits a DAE nature as illustrated in Chapter 4. An states estimator based on such descriptor system was possible thanks to the fact that the input current appears linearly the in the equivalent circuit models. Electrochemical model-based modeling for packs creates opportunities for estimation and control design for nonlinear DAEs and partial differential algebraic equations (PDAEs) [173].

Model Observability

It is noted in many previous studies that the battery electrochemical models, e.g. SPM, is not locally observable from the current and voltage measurements in the linear sense [22, 40, 141, 174]. Many attempts have been proposed to mitigate issue, including representing dynamics of one electrode as a function of another using conservation of lithium and designing an open-loop observer for one electrode and a closed-loop estimator for another. However, the locally unobservable conclusion for the electrochemical models are mostly derived based on the fact that the observability matrix constructed from the linearized system matrices loses rank. Local unobservability based linearization does not provide a comprehensive indication for the observability of the original nonlinear electrochemical models. Potential extensions on the observability studies could be significant by (i) exploring nonlinear observability, and

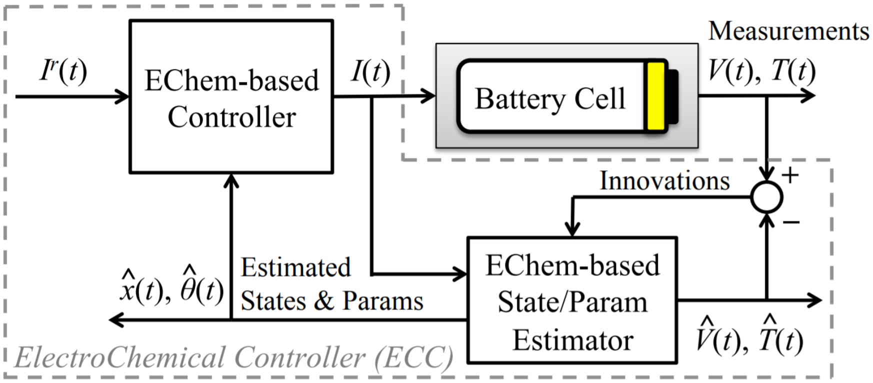

Figure 7.1: A block diagram for electrochemical model-based closed-loop control system [7].

(2) examining the local observability using the linearized system in a more comprehensive manner.

Battery Pack Modeling and Estimation

It was highlighted in Chapter 4 that battery pack system modeling can be divided into three categories. The first approach treats the entire pack as one lumped single cell [87]. However, in practice, some cells are more prone to violate safety-critical constraints than others, which cannot be resolved from the lumped single cell approach. The second modeling approach also relies on a single cell model, but it focuses on a set of specific in-pack cells – the weakest and the strongest ones [85, 88]. The last modeling approach is based on the interconnection of single cell models [89, 90, 91], which benefit from high fidelity cell-by-cell resolution, but it might suffer from high real-time computational burden. Similar to Chapter 4, recent works have been recognizing that parallel-connected cells are as crucial as cells in series, which involves a more challenging mathematical system [175, 176]. Detailed physical-based cell models for pack modeling will generate intractable computational burden, whereas empirical models lose track of the actual electrochemistry. Modeling and estimation tasks for packs still require careful designs to seek appropriate balances.

Feedback Control

The ultimate objective of a model-based control system in a battery management system is to close the loop, i.e. optimally control the applied current for some defined objective [177]. One of the examples of such an electrochemical model-based control topology is shown in Fig. 7.1 [7]. The EChem-based Controller in Fig. 7.1 uses the estimated states and parameters, which is the focus of this dissertation, to determine an optimal current trajectory. To advance this research, the closed-loop stability must be established for the electrochemical models [146, 164, 165]

Bibliography

[1] Runsen Zhang and Shinichiro Fujimori. "The role of transport electrification in global climate change mitigation scenarios". In: *Environmental Research Letters* 15.3 (2020), p. 034019.

[2] Stephanie Heitel et al. "Global electric car market deployment considering endogenous battery price development". In: *Technological Learning in the Transition to a Low-Carbon Energy System.* Elsevier, 2020, pp. 281–305.

[3] Nalin A Chaturvedi et al. "Algorithms for advanced battery-management systems". In: *IEEE Control systems magazine* 30.3 (2010), pp. 49–68.

[4] Leigh Anna Marie Steele et al. *Understanding Lithium Ion Battery Fires.* Tech. rep. Sandia National Lab.(SNL-NM), Albuquerque, NM (United States), 2014.

[5] Joseph M Kolly, Joseph Panagiotou, and BA Czech. "The Investigation of a Lithium-Ion Battery Fire Onboard a Boeing 787 by the US National Transportation Safety Board". In: *Safety Research Corporation of America: Dothan, AL, USA* (2013), pp. 1–18.

[6] Gregory L Plett. *Battery management systems, Volume I: Battery modeling.* Vol. 1. Artech House, 2015.

[7] Scott J Moura. "Estimation and control of battery electrochemistry models: A tutorial". In: *2015 54th IEEE Conference on Decision and Control (CDC).* IEEE. 2015, pp. 3906–3912.

[8] Hector Eduardo Perez. "Model Based Optimal Control, Estimation, and Validation of Lithium-Ion Batteries". PhD thesis. UC Berkeley, 2016.

[9] Qingsong Wang et al. "Thermal runaway caused fire and explosion of lithium ion battery". In: *Journal of Power Sources* 208 (2012), pp. 210–224.

[10] John Wang et al. "Cycle-life model for graphite-LiFePO$_4$ cells". In: *Journal of Power Sources* 196.8 (2011), pp. 3942–3948.

[11] Xinfan Lin et al. "A lumped-parameter electro-thermal model for cylindrical batteries". In: *Journal of Power Sources* 257 (2014), pp. 1–11.

[12] Vijay A Sethuraman et al. "In situ measurements of stress evolution in silicon thin films during electrochemical lithiation and delithiation". In: *Journal of Power Sources* 195.15 (2010), pp. 5062–5066.

[13] Anthony Barré et al. "A review on lithium-ion battery ageing mechanisms and estimations for automotive applications". In: *Journal of Power Sources* 241 (2013), pp. 680–689.

[14] Caihao Weng, Jing Sun, and Huei Peng. "A unified open-circuit-voltage model of lithium-ion batteries for state-of-charge estimation and state-of-health monitoring". In: *Journal of power Sources* 258 (2014), pp. 228–237.

[15] Sung Park, Andreas Savvides, and Mani Srivastava. "Battery capacity measurement and analysis using lithium coin cell battery". In: *Proceedings of the 2001 international symposium on Low power electronics and design*. ACM. 2001, pp. 382–387.

[16] Thomas F Fuller, Marc Doyle, and John Newman. "Simulation and optimization of the dual lithium ion insertion cell". In: *Journal of the Electrochemical Society* 141.1 (1994), pp. 1–10.

[17] Gregory L Plett. "Sigma-point Kalman filtering for battery management systems of LiPB-based HEV battery packs: Part 2: Simultaneous state and parameter estimation". In: *Journal of power sources* 161.2 (2006), pp. 1369–1384.

[18] Gregory L Plett. "Extended Kalman filtering for battery management systems of LiPB-based HEV battery packs: Part 3. State and parameter estimation". In: *Journal of Power sources* 134.2 (2004), pp. 277–292.

[19] IL-Song Kim. "A technique for estimating the state of health of lithium batteries through a dual-sliding-mode observer". In: *IEEE Transactions on Power Electronics* 25.4 (2010), pp. 1013–1022.

[20] Xinfan Lin et al. "Online parameterization of lumped thermal dynamics in cylindrical lithium ion batteries for core temperature estimation and health monitoring". In: *IEEE Transactions on Control Systems Technology* 21.5 (2013), pp. 1745–1755.

[21] Alexander Bartlett et al. "Electrochemical model-based state of charge and capacity estimation for a composite electrode lithium-ion battery". In: *IEEE Transactions on Control Systems Technology* 24.2 (2016), pp. 384–399.

[22] Scott J Moura, Nalin A Chaturvedi, and Miroslav Krstić. "Adaptive partial differential equation observer for battery state-of-charge/state-of-health estimation via an electrochemical model". In: *Journal of Dynamic Systems, Measurement, and Control* 136.1 (2014), p. 011015.

[23] Yinjiao Xing et al. "An ensemble model for predicting the remaining useful performance of lithium-ion batteries". In: *Microelectronics Reliability* 53.6 (2013), pp. 811–820.

[24] M Orchard et al. "Risk-sensitive particle-filtering-based prognosis framework for estimation of remaining useful life in energy storage devices". In: *Studies in Informatics and Control* 19.3 (2010), pp. 209–218.

[25] Verena Klass, Mårten Behm, and Göran Lindbergh. "Evaluating real-life performance of lithium-ion battery packs in electric vehicles". In: *Journal of The Electrochemical Society* 159.11 (2012), A1856–A1860.

[26] Bhaskar Saha et al. "Prognostics methods for battery health monitoring using a Bayesian framework". In: *IEEE Transactions on Instrumentation and Measurement* 58.2 (2009), pp. 291–296.

[27] Chanwoo Park and Arun K Jaura. *Dynamic thermal model of Li-ion battery for predictive behavior in hybrid and fuel cell vehicles*. Tech. rep. SAE Technical Paper, 2003.

[28] Christophe Forgez et al. "Thermal modeling of a cylindrical $LiFePO_4$/graphite lithium-ion battery". In: *Journal of Power Sources* 195.9 (2010), pp. 2961–2968.

[29] Berit Floor Lund and Bjarne A Foss. "Parameter ranking by orthogonalization - Applied to nonlinear mechanistic models". In: *Automatica* 44.1 (2008), pp. 278–281.

[30] Petros A Ioannou and Jing Sun. *Robust adaptive control*. Courier Corporation, 2012.

[31] Alberto Isidori. *Nonlinear control systems*. Springer Science & Business Media, 2013.

[32] Hassan K Khalil. "Noninear systems". In: *Prentice-Hall, New Jersey* 2.5 (1996), pp. 5–1.

[33] Bahram Shafai and Mehrdad Saif. "Proportional-Integral observer in robust control, fault detection, and decentralized control of dynamic systems". In: *Control and Systems Engineering*. Springer, 2015, pp. 13–43.

[34] M Safari and C Delacourt. "Modeling of a commercial graphite/$LiFePO_4$ cell". In: *Journal of The Electrochemical Society* 158.5 (2011), A562–A571.

[35] HE Perez et al. "Optimal Charging of Li-Ion Batteries via a Single Particle Model with Electrolyte and Thermal Dynamics". In: *Journal of The Electrochemical Society* 164.7 (2017), A1–A9.

[36] Xiaosong Hu, Shengbo Li, and Huei Peng. "A comparative study of equivalent circuit models for Li-ion batteries". In: *Journal of Power Sources* 198 (2012), pp. 359–367.

[37] Shriram Santhanagopalan et al. "Review of models for predicting the cycling performance of lithium ion batteries". In: *Journal of Power Sources* 156.2 (2006), pp. 620–628.

[38] Marc Doyle, Thomas F Fuller, and John Newman. "Modeling of galvanostatic charge and discharge of the lithium/polymer/insertion cell". In: *Journal of the Electrochemical society* 140.6 (1993), p. 1526.

[39] Shriram Santhanagopalan and Ralph E White. “Online estimation of the state of charge of a lithium ion cell”. In: *Journal of power sources* 161.2 (2006), pp. 1346–1355.

[40] Domenico Di Domenico, Anna Stefanopoulou, and Giovanni Fiengo. “Lithium-ion battery state of charge and critical surface charge estimation using an electrochemical model-based extended Kalman filter”. In: *Journal of dynamic systems, measurement, and control* 132.6 (2010), p. 061302.

[41] N Lotfi et al. “Electrochemical model-based adaptive estimation of Li-ion battery state of charge”. In: *ASME Dyn. Syst. Control Conf.* 2015.

[42] Saeed Khaleghi Rahimian, Sean Rayman, and Ralph E White. “Extension of physics-based single particle model for higher charge–discharge rates”. In: *Journal of Power Sources* 224 (2013), pp. 180–194.

[43] Scott J Moura et al. “Battery state estimation for a single particle model with electrolyte dynamics”. In: *IEEE Transactions on Control Systems Technology* 25.2 (2017), pp. 453–468.

[44] Tanvir R Tanim, Christopher D Rahn, and Chao-Yang Wang. “State of charge estimation of a lithium ion cell based on a temperature dependent and electrolyte enhanced single particle model”. In: *Energy* 80 (2015), pp. 731–739.

[45] Reinhardt Klein et al. “Electrochemical model based observer design for a lithium-ion battery”. In: *IEEE Transactions on Control Systems Technology* 21.2 (2013), pp. 289–301.

[46] Dong Zhang et al. “Remaining useful life estimation of Lithium-ion batteries based on thermal dynamics”. In: *American Control Conference (ACC), 2017*. IEEE. 2017, pp. 4042–4047.

[47] Dong Zhang et al. “Real-Time Capacity Estimation of Lithium-Ion Batteries Utilizing Thermal Dynamics”. In: *IEEE Transactions on Control Systems Technology* (2019).

[48] Scott J Moura, N Chaturvedi, and M Krstic. “Adaptive PDE observer for battery SOC/SOH estimation”. In: *2012 ASME Dynamic Systems and Control Conference*. 2012.

[49] Satadru Dey, Beshah Ayalew, and Pierluigi Pisu. “Adaptive observer design for a Li-ion cell based on coupled electrochemical-thermal model”. In: *ASME Paper No. DSCC2014-5986* (2014).

[50] S Kalnaus, K Rhodes, and C Daniel. “A study of lithium ion intercalation induced fracture of silicon particles used as anode material in Li-ion battery”. In: *Journal of Power Sources* 196.19 (2011), pp. 8116–8124.

[51] KE Aifantis and JP Dempsey. “Stable crack growth in nanostructured Li-batteries”. In: *Journal of power sources* 143.1 (2005), pp. 203–211.

[52] Rutooj Deshpande, Yue Qi, and Yang-Tse Cheng. "Effects of concentration-dependent elastic modulus on diffusion-induced stresses for battery applications". In: *Journal of the Electrochemical Society* 157.8 (2010), A967–A971.

[53] John Christensen and John Newman. "Stress generation and fracture in lithium insertion materials". In: *Journal of Solid State Electrochemistry* 10.5 (2006), pp. 293–319.

[54] Xiangchun Zhang, Wei Shyy, and Ann Marie Sastry. "Numerical simulation of intercalation-induced stress in Li-ion battery electrode particles". In: *Journal of the Electrochemical Society* 154.10 (2007), A910–A916.

[55] J Li et al. "A Single Particle Model for Lithium-Ion Batteries with Electrolyte and Stress-Enhanced Diffusion Physics". In: *Journal of The Electrochemical Society* 164.4 (2017), A874–A883.

[56] Bharatkumar Suthar et al. "Optimal charging profiles for mechanically constrained lithium-ion batteries". In: *Physical Chemistry Chemical Physics* 16.1 (2014), pp. 277–287.

[57] Mehdi M Forouzan, Brian A Mazzeo, and Dean R Wheeler. "Modeling the effects of electrode microstructural heterogeneities on Li-ion battery performance and lifetime". In: *Journal of The Electrochemical Society* 165.10 (2018), A2127–A2144.

[58] Dong Zhang, Satadru Dey, and Scott J Moura. "Lithium-Ion Battery State Estimation for a Single Particle Model with Intercalation-Induced Stress". In: *2018 Annual American Control Conference (ACC)*. IEEE. 2018, pp. 2294–2299.

[59] John Christensen and John Newman. "A mathematical model of stress generation and fracture in lithium manganese oxide". In: *Journal of The Electrochemical Society* 153.6 (2006), A1019–A1030.

[60] J Vetter et al. "Ageing mechanisms in lithium-ion batteries". In: *Journal of power sources* 147.1 (2005), pp. 269–281.

[61] M Broussely et al. "Main aging mechanisms in Li ion batteries". In: *Journal of power sources* 146.1 (2005), pp. 90–96.

[62] Cheng Lin et al. "Analysis for Mechanical Failure of DISs with Graphite Anode in Lithium ion Batteries for Electric Vehicles". In: *Nanomaterials and Nanotechnology* 6 (2016), p. 1847980416680806.

[63] Pallab Barai et al. "Reduced order modeling of mechanical degradation induced performance decay in lithium-ion battery porous electrodes". In: *Journal of The Electrochemical Society* 162.9 (2015), A1751–A1771.

[64] Thomas Meurer. "On the extended Luenberger-type observer for semilinear distributed-parameter systems". In: *IEEE Transactions on Automatic Control* 58.7 (2013), pp. 1732–1743.

[65] Andrey Smyshlyaev and Miroslav Krstic. *Adaptive control of parabolic PDEs*. Princeton University Press, 2010.

[66] Tarek Ahmed-Ali et al. "Adaptive boundary observer for parabolic PDEs subject to domain and boundary parameter uncertainties". In: *Automatica* 72 (2016), pp. 115–122.

[67] Pedro Ascencio. "Adaptive observer design for parabolic partial differential equations". In: *Imperial College London* (2017).

[68] Satadru Dey, Beshah Ayalew, and Pierluigi Pisu. "Nonlinear adaptive observer for a lithium-ion battery cell based on coupled electrochemical–thermal model". In: *Journal of Dynamic Systems, Measurement, and Control* 137.11 (2015), p. 111005.

[69] Xinfan Lin et al. "State of Charge Imbalance Estimation for Battery Strings Under Reduced Voltage Sensing." In: *IEEE Trans. Contr. Sys. Techn.* 23.3 (2015), pp. 1052–1062.

[70] Shi Zhao, Stephen R Duncan, and David A Howey. "Observability analysis and state estimation of lithium-ion batteries in the presence of sensor biases". In: *IEEE Transactions on Control Systems Technology* 25.1 (2017), pp. 326–333.

[71] Mathukumalli Vidyasagar. *Nonlinear systems analysis*. Vol. 42. Siam, 2002.

[72] Rutooj Deshpande et al. "Battery cycle life prediction with coupled chemical degradation and fatigue mechanics". In: *Journal of the Electrochemical Society* 159.10 (2012), A1730–A1738.

[73] M Safari et al. "Life-prediction methods for lithium-ion batteries derived from a fatigue approach I. Introduction: capacity-loss prediction based on damage accumulation". In: *Journal of The Electrochemical Society* 157.6 (2010), A713–A720.

[74] Liqiang Zhang et al. "Non-destructive analysis of degradation mechanisms in cycle-aged graphite/$LiCoO_2$ batteries". In: *Energies* 7.10 (2014), pp. 6282–6305.

[75] Young Man Cho and Rajesh Rajamani. "A systematic approach to adaptive observer synthesis for nonlinear systems". In: *IEEE transactions on Automatic Control* 42.4 (1997), pp. 534–537.

[76] Riccardo Marino. "Adaptive observers for single output nonlinear systems". In: *IEEE Transactions on Automatic Control* 35.9 (1990), pp. 1054–1058.

[77] Yuri Shtessel et al. "Introduction: intuitive theory of sliding mode control". In: *Sliding Mode Control and Observation*. Springer, 2014, pp. 1–42.

[78] Kumpati S Narendra and Anuradha M Annaswamy. *Stable adaptive systems*. Courier Corporation, 2012.

[79] JS Newman. "Fortran programs for simulation of electrochemical systems, dualfoil. f program for lithium battery simulation". In: *Available on: www. cchem. berkeley. edu/jsngrp/fortran. html* (2004).

[80] Soren Ebbesen, Pascal Kiwitz, and Lino Guzzella. “A generic particle swarm optimization Matlab function”. In: *American Control Conference (ACC), 2012*. IEEE. 2012, pp. 1519–1524.

[81] Miroslav Krstic and Andrey Smyshlyaev. *Boundary control of PDEs: A course on backstepping designs*. Vol. 16. Siam, 2008.

[82] Scott J Moura and Hosam K Fathy. “Optimal boundary control & estimation of diffusion-reaction PDEs”. In: *American Control Conference (ACC), 2011*. IEEE. 2011, pp. 921–928.

[83] Xinfan Lin and Anna G Stefanopoulou. “Analytic bound on accuracy of battery state and parameter estimation”. In: *Journal of The Electrochemical Society* 162.9 (2015), A1879–A1891.

[84] Jake Christensen. “Modeling diffusion-induced stress in Li-ion cells with porous electrodes”. In: *Journal of the Electrochemical Society* 157.3 (2010), A366–A380.

[85] Liang Zhong et al. “A method for the estimation of the battery pack state of charge based on in-pack cells uniformity analysis”. In: *Applied Energy* 113 (2014), pp. 558–564.

[86] X. Lin et al. “State of Charge Imbalance Estimation for Battery Strings Under Reduced Voltage Sensing”. In: *IEEE Transactions on Control Systems Technology* 23.3 (2015), pp. 1052–1062.

[87] S. Castano et al. “Dynamical modeling procedure of a Li-ion battery pack suitable for real-time applications”. In: *Energy Conversion and Management* 92 (2015), pp. 396–405.

[88] Yin Hua et al. “A multi time-scale state-of-charge and state-of-health estimation framework using nonlinear predictive filter for lithium-ion battery pack with passive balance control”. In: *Journal of Power Sources* 280 (2015), pp. 293–312.

[89] Yuejiu Zheng et al. “Cell state-of-charge inconsistency estimation for $LiFePO_4$ battery pack in hybrid electric vehicles using mean-difference model”. In: *Applied Energy* 111 (2013), pp. 571–580.

[90] Xu Zhang et al. “An on-line estimation of battery pack parameters and state-of-charge using dual filters based on pack model”. In: *Energy* 115 (2016), pp. 219–229.

[91] Ting Zhao et al. “Robust Online State of Charge Estimation of Lithium-Ion Battery Pack Based on Error Sensitivity Analysis”. In: *Mathematical Problems in Engineering* 2015 (2015), p. 11.

[92] Xiaosong Hu, Fengchun Sun, and Yuan Zou. “Estimation of state of charge of a lithium-ion battery pack for electric vehicles using an adaptive Luenberger observer”. In: *Energies* 3.9 (2010), pp. 1586–1603.

[93] Thomas Bruen and James Marco. “Modelling and experimental evaluation of parallel connected lithium ion cells for an electric vehicle battery system”. In: *Journal of Power Sources* 310 (2016), pp. 91–101.

[94] Guang-Ren Duan. *Analysis and design of descriptor linear systems*. Vol. 23. Springer Science & Business Media, 2010.

[95] R. Nikoukhah, A. S. Willsky, and B. C. Levy. “Kalman filtering and Riccati equations for descriptor systems”. In: *IEEE Transactions on Automatic Control* 37.9 (1992), pp. 1325–1342.

[96] L. Chisci and G. Zappa. “Square-root Kalman filtering of descriptor systems”. In: *Systems & Control Letters* 19.4 (1992), pp. 325–334.

[97] M. Darouach and M. Boutayeb. “Design of observers for descriptor systems”. In: *IEEE Transactions on Automatic Control* 40.7 (1995), pp. 1323–1327.

[98] M. Boutayeb and M. Darouach. “Observers design for nonlinear descriptor systems”. In: *34th IEEE Conference on Decision and Control*. Vol. 3. 1995, 2369–2374 vol.3.

[99] Gerta Zimmer and Jürgen Meier. “On observing nonlinear descriptor systems”. In: *Systems & Control Letters* 32.1 (1997), pp. 43–48.

[100] Jan Åslund and Erik Frisk. “An observer for non-linear differential-algebraic systems”. In: *Automatica* 42.6 (2006), pp. 959–965.

[101] Rajesh Rajamani. “Observers for Lipschitz nonlinear systems”. In: *IEEE transactions on Automatic Control* 43.3 (1998), pp. 397–401.

[102] S Kaprielian and J Turi. “An observer for a nonlinear descriptor system”. In: *31st IEEE Conference on Decision and Control*. 1992, pp. 975–976.

[103] Lu Guoping and D. W. C. Ho. “Full-order and reduced-order observers for Lipschitz descriptor systems: the unified LMI approach”. In: *IEEE Transactions on Circuits and Systems II: Express Briefs* 53.7 (2006), pp. 563–567.

[104] M. Darouach and L. Boutat-Baddas. “Observers for a Class of Nonlinear Singular Systems”. In: *IEEE Transactions on Automatic Control* 53.11 (2008), pp. 2627–2633.

[105] D. N. Shields. “Observer design and detection for nonlinear descriptor systems”. In: *International Journal of Control* 67.2 (1997), pp. 153–168.

[106] João S. Albuquerque and Lorenz T. Biegler. “Decomposition algorithms for on-line estimation with nonlinear DAE models”. In: *Computers & chemical engineering* 21.3 (1997), pp. 283–299.

[107] V. M. Becerra, P. D. Roberts, and G. W. Griffiths. “Applying the extended Kalman filter to systems described by nonlinear differential-algebraic equations”. In: *Control Engineering Practice* 9.3 (2001), pp. 267–281.

[108] R.K. Mandela et al. “Recursive state estimation techniques for nonlinear differential algebraic systems”. In: *Chemical Engineering Science* 65.16 (2010), pp. 4548–4556.

[109] Yash Puranik et al. “An Ensemble Kalman Filter for Systems Governed by Differential Algebraic Equations (DAEs)”. In: *IFAC Proceedings Volumes* 45.15 (2012), pp. 531–536.

[110] Tarun Huria et al. “High fidelity electrical model with thermal dependence for characterization and simulation of high power lithium battery cells”. In: *IEEE International Electric Vehicle Conference (IEVC)* (2012).

[111] Xinfan Lin et al. “Online parameterization of lumped thermal dynamics in cylindrical lithium ion batteries for core temperature estimation and health monitoring”. In: *IEEE Transactions on Control Systems Technology* 21.5 (2012), pp. 1745–1755.

[112] Xinfan Lin et al. “Parameterization and Observability Analysis of Scalable Battery Clusters for Onboard Thermal Management”. In: *Oil & Gas Science and Technology* 68.1 (2013), pp. 165–178.

[113] Xiaosong Hu, Fengchun Sun, and Yuan Zou. “Estimation of state of charge of a lithium-ion battery pack for electric vehicles using an adaptive Luenberger observer”. In: *Energies* 3.9 (2010), pp. 1586–1603.

[114] Gregory Plett. “Extended Kalman filtering for battery management systems of LiPB-based HEV battery packs: Part 1. Background”. In: *Journal of Power Sources* 134 (2004), pp. 252–261.

[115] Luis D Couto and Michel Kinnaert. “Partition-based unscented Kalman filter for reconfigurable battery pack state estimation using an electrochemical model”. In: *American Control Conference (ACC)*. 2018, pp. 3122–3128.

[116] Taesic Kim, Wei Qiao, and Liayn Qu. “Online SOC and SOH estimation for multicell lithium-ion batteries based on an adaptive hybrid battery model and sliding-mode observer”. In: *IEEE Energy Conversion Congress and Exposition*. 2013, pp. 292–298.

[117] Tarek Raissi, Denis Efimov, and Ali Zolghadri. “Interval state estimation for a class of nonlinear systems”. In: *IEEE Transactions on Automatic Control* 57.1 (2011), pp. 260–265.

[118] Stanislav Chebotarev et al. “Interval observers for continuous-time LPV systems with L1/L2 performance”. In: *Automatica* 58 (2015), pp. 82–89.

[119] Gang Zheng, Denis Efimov, and Wilfrid Perruquetti. “Design of interval observer for a class of uncertain unobservable nonlinear systems”. In: *Automatica* 63 (2016), pp. 167–174.

[120] Hector E Perez and Scott J Moura. “Sensitivity-based interval PDE observer for battery SOC estimation”. In: *American Control Conference (ACC)*. 2015, pp. 323–328.

[121] M. Vidyasagar. *Nonlinear Systems Analysis*. Vol. 42. Philadelphia, PA, USA: SIAM, 2002.

[122] M. Rausch et al. "Nonlinear observability and identifiability of single cells in battery packs". In: *2013 IEEE International Conference on Control Applications*. 2013, pp. 401–406.

[123] S. Zhao, S. R. Duncan, and D. A. Howey. "Observability Analysis and State Estimation of Lithium-Ion Batteries in the Presence of Sensor Biases". In: *IEEE Transactions on Control Systems Technology* 25.1 (2017), pp. 326–333.

[124] Xinfan Lin et al. *Estimating core temperatures of battery cells in a battery pack*. US Patent 10,230,137. 2019.

[125] Shi Zhao, Stephen R Duncan, and David A Howey. "Observability analysis and state estimation of lithium-ion batteries in the presence of sensor biases". In: *IEEE Transactions on Control Systems Technology* 25.1 (2016), pp. 326–333.

[126] Denis Efimov, Tarek Raissi, and Ali Zolghadri. "Control of nonlinear and LPV systems: interval observer-based framework". In: *IEEE Transactions on Automatic Control* 58.3 (2013), pp. 773–778.

[127] Denis Efimov, Andrey Polyakov, and Jean-Pierre Richard. "Interval observer design for estimation and control of time-delay descriptor systems". In: *European Journal of Control* 23 (2015), pp. 26–35.

[128] Michel Broussely et al. "Main aging mechanisms in Li ion batteries". In: *Journal of Power Sources* 146.1-2 (2005), pp. 90–96.

[129] Daniel H Doughty et al. "Lithium battery thermal models". In: *Journal of Power Sources* 110.2 (2002), pp. 357–363.

[130] Gi-Heon Kim, Ahmad Pesaran, and Robert Spotnitz. "A three-dimensional thermal abuse model for lithium-ion cells". In: *Journal of Power Sources* 170.2 (2007), pp. 476–489.

[131] Li Song and James W Evans. "Electrochemical-thermal model of lithium polymer batteries". In: *Journal of the Electrochemical Society* 147.6 (2000), pp. 2086–2095.

[132] SC Chen, CC Wan, and YY Wang. "Thermal analysis of lithium-ion batteries". In: *Journal of Power Sources* 140.1 (2005), pp. 111–124.

[133] Satadru Dey et al. "Model-based real-time thermal fault diagnosis of Lithium-ion batteries". In: *Control Engineering Practice* 56 (2016), pp. 37–48.

[134] Said Al Hallaj et al. "Thermal modeling and design considerations of lithium-ion batteries". In: *Journal of Power Sources* 83.1-2 (1999), pp. 1–8.

[135] WB Gu and Chao-Yang Wang. "Thermal and electrochemical coupled modeling of a lithium-ion cell". In: *Proceedings of the ECS*. Vol. 99. 2000, pp. 748–762.

[136] Matteo Muratori, Marcello Canova, and Yann Guezennec. "A spatially–reduced dynamic model for the thermal characterisation of Li–ion battery cells". In: *International Journal of Vehicle Design* 58.2 (2012), p. 134.

[137] Kandler Smith and Chao-Yang Wang. “Power and thermal characterization of a lithium-ion battery pack for hybrid-electric vehicles”. In: *Journal of Power Sources* 160.1 (2006), pp. 662–673.

[138] Dong Zhang et al. “Remaining useful life estimation of lithium-ion batteries based on thermal dynamics”. In: *American Control Conference (ACC)*. 2017, pp. 4042–4047.

[139] Y Hu and S Yurkovich. “Battery cell state-of-charge estimation using linear parameter varying system techniques”. In: *Journal of Power Sources* 198 (2012), pp. 338–350.

[140] Shu-Xia Tang et al. “State-of-Charge estimation from a thermal–electrochemical model of lithium-ion batteries”. In: *Automatica* 83 (2017), pp. 206–219.

[141] Dong Zhang et al. “Battery Adaptive Observer for a Single-Particle Model With Intercalation-Induced Stress”. In: *IEEE transactions on control systems technology* (2019).

[142] Satadru Dey, Hector E Perez, and Scott J Moura. “Model-based battery thermal fault diagnostics: Algorithms, analysis, and experiments”. In: *IEEE Transactions on Control Systems Technology* 27.2 (2017), pp. 576–587.

[143] Youngki Kim et al. “The estimation of temperature distribution in cylindrical battery cells under unknown cooling conditions”. In: *IEEE Transactions on Control Systems Technology* 22.6 (2014), pp. 2277–2286.

[144] Robert R Richardson, Peter T Ireland, and David A Howey. “Battery internal temperature estimation by combined impedance and surface temperature measurement”. In: *Journal of Power Sources* 265 (2014), pp. 254–261.

[145] Takao Nambu. “On the stabilization of diffusion equations: boundary observation and feedback”. In: *Journal of Differential Equations* 52.2 (1984), pp. 204–233.

[146] Andrey Smyshlyaev and Miroslav Krstic. “On control design for PDEs with space-dependent diffusivity or time-dependent reactivity”. In: *Automatica* 41.9 (2005), pp. 1601–1608.

[147] Miroslav Krstic and Andrey Smyshlyaev. *Boundary control of PDEs: A course on backstepping designs*. Vol. 16. Siam, 2008.

[148] Rafael Vazquez and Miroslav Krstic. “Control of 1-D parabolic PDEs with Volterra nonlinearities, part I: design”. In: *Automatica* 44.11 (2008), pp. 2778–2790.

[149] Rafael Vazquez and Miroslav Krstic. “Control of 1D parabolic PDEs with Volterra nonlinearities, part II: analysis”. In: *Automatica* 44.11 (2008), pp. 2791–2803.

[150] Miroslav Krstic. “On global stabilization of Burgers’ equation by boundary control”. In: *Systems & Control Letters* 37.3 (1999), pp. 123–141.

[151] Meng-Bi Cheng, Verica Radisavljevic, and Wu-Chung Su. “Sliding mode boundary control of a parabolic PDE system with parameter variations and boundary uncertainties”. In: *Automatica* 47.2 (2011), pp. 381–387.

[152] Yunus Cengel. *Heat and mass transfer: fundamentals and applications*. McGraw-Hill Higher Education, 2014.

[153] Sun Ung Kim et al. “Thermoelectrochemical simulations of performance and abuse in 50-Ah automotive cells”. In: *Journal of Power Sources* 268 (2014), pp. 625–633.

[154] D Bernardi, E Pawlikowski, and John Newman. “A general energy balance for battery systems”. In: *Journal of the Electrochemical Society* 132.1 (1985), pp. 5–12.

[155] Nassim A Samad, Jason B Siegel, and Anna G Stefanopoulou. “Parameterization and validation of a distributed coupled electro-thermal model for prismatic cells”. In: *ASME 2014 Dynamic Systems and Control Conference*. American Society of Mechanical Engineers. 2014, V002T23A006–V002T23A006.

[156] Stefan Käbitz et al. “Cycle and calendar life study of a graphite | $\mathrm{LiNi_{1/3}Mn_{1/3}Co_{1/3}O_2}$ Li-ion high energy system. Part A: Full cell characterization”. In: *Journal of Power Sources* 239 (2013), pp. 572–583.

[157] Bor Yann Liaw et al. “Correlation of Arrhenius behaviors in power and capacity fades with cell impedance and heat generation in cylindrical lithium-ion cells”. In: *Journal of Power Sources* 119 (2003), pp. 874–886.

[158] Amnon Pazy. *Semigroups of linear operators and applications to partial differential equations*. Vol. 44. Springer Science & Business Media, 2012.

[159] Hossein Maleki et al. “Thermal properties of lithium-ion battery and components”. In: *Journal of the Electrochemical Society* 146.3 (1999), pp. 947–954.

[160] Rafael Vazquez and Miroslav Krstic. “Explicit output feedback stabilization of a thermal convection loop by continuous backstepping and singular perturbations”. In: *2007 American Control Conference*. IEEE. 2007, pp. 2177–2182.

[161] George Avalos. “The exponential stability of a coupled hyperbolic/parabolic system arising in structural acoustics”. In: *Abstract and Applied Analysis*. Vol. 1. 2. Hindawi. 1996, pp. 203–217.

[162] Jun-Jun Liu and Jun-Min Wang. “Active disturbance rejection control and sliding mode control of one-dimensional unstable heat equation with boundary uncertainties”. In: *IMA Journal of Mathematical Control and Information* 32.1 (2015), pp. 97–117.

[163] Alessandro Pisano and Yury Orlov. “Boundary second-order sliding-mode control of an uncertain heat process with unbounded matched perturbation”. In: *Automatica* 48.8 (2012), pp. 1768–1775.

[164] Ji Wang et al. “Exponential regulation of the anti-collocatedly disturbed cage in a wave PDE-modeled ascending cable elevator”. In: *Automatica* 95 (2018), pp. 122–136.

[165] Bao-Zhu Guo and Feng-Fei Jin. “Output feedback stabilization for one-dimensional wave equation subject to boundary disturbance”. In: *IEEE Transactions on Automatic control* 60.3 (2014), pp. 824–830.

[166] Jingqing Han. “From PID to active disturbance rejection control”. In: *IEEE transactions on Industrial Electronics* 56.3 (2009), pp. 900–906.

[167] Bao-Zhu Guo and Zhi-liang Zhao. “On the convergence of an extended state observer for nonlinear systems with uncertainty”. In: *Systems & Control Letters* 60.6 (2011), pp. 420–430.

[168] Ji Wang et al. “Disturbance Estimation of a Wave PDE on a Time-varying Domain”. In: *2017 Proceedings of the conference on control and its applications*. SIAM. 2017, pp. 107–111.

[169] Hongyinping Feng and Bao-Zhu Guo. “Output feedback stabilization of an unstable wave equation with general corrupted boundary observation”. In: *Automatica* 50.12 (2014), pp. 3164–3172.

[170] Hongyinping Feng and Bao-Zhu Guo. “New unknown input observer and output feedback stabilization for uncertain heat equation”. In: *Automatica* 86 (2017), pp. 1–10.

[171] David F Griffiths, John W Dold, and David J Silvester. *Essential partial differential equations*. Springer, 2015.

[172] Shuxia Tang and Chengkang Xie. “State and output feedback boundary control for a coupled PDE–ODE system”. In: *Systems & Control Letters* 60.8 (2011), pp. 540–545.

[173] Wade S Martinson and Paul I Barton. “A differentiation index for partial differential-algebraic equations”. In: *SIAM Journal on Scientific Computing* 21.6 (2000), pp. 2295–2315.

[174] Satadru Dey, Beshah Ayalew, and Pierluigi Pisu. “Nonlinear robust observers for state-of-charge estimation of lithium-ion cells based on a reduced electrochemical model”. In: *IEEE Transactions on Control Systems Technology* 23.5 (2015), pp. 1935–1942.

[175] Markus H Hofmann et al. “Dynamics of current distribution within battery cells connected in parallel”. In: *Journal of Energy Storage* 20 (2018), pp. 120–133.

[176] Xinyuan Fan et al. “Simplified Battery Pack Modeling Considering Inconsistency and Evolution of Current Distribution”. In: *IEEE Transactions on Intelligent Transportation Systems* (2020).

[177] Hector Perez et al. “Optimal Charging of Li-Ion Batteries with Coupled Electro-Thermal-Aging Dynamics”. In: *IEEE Transactions on Vehicular Technology* (2017).

Appendix A

Well-Posedness for Linear BVP

The following lemma is well-established to deal with the well-posedness of a linear BVP [171].

Lemma 21. *Suppose the BVP under consideration is written in the form*

$$(\mathcal{H}u)(x,t) = \mathcal{F}(x,t), \tag{A.1}$$

where $\mathcal{H}$ contains both the differential and boundary operators, and $\mathcal{F}$ the data terms comprising the right hand side of the differential equation and the boundary conditions. Moreover, suppose

1. *$\mathcal{H}$ is linear.*
2. *$\mathcal{H}$ is inverse monotone: $\mathcal{H}v \geq 0$ implies $v \geq 0$.*
3. *A bounded and non-negative comparison function $\phi(x)$ exists, such that $\mathcal{H}\phi(x) \geq 1$ for all $x \in [0,1]$.*

If an appropriate norm $\|\cdot\|_u$ is defined such that

$$-\|\mathcal{F}\|_u \leq \mathcal{F} \leq \|\mathcal{F}\|_u, \tag{A.2}$$

then the problem $(\mathcal{H}u) = \mathcal{F}$ is well-posed:

$$-\|\mathcal{F}\|_u\phi \leq u \leq \|\mathcal{F}\|_u\phi \tag{A.3}$$

at all points $x \in [0,1]$, which means that

$$\max_{x\in[0,1]} |u| \leq \gamma\|\mathcal{F}\|_u, \tag{A.4}$$

where $\gamma = \max_{x\in[0,1]} \phi$.

The proof of Lemma 21 is omitted here. The detailed steps of the proof can be retrieved in Section 5.2 of [171].